Titre: Title:	Ball-in-Track Nonlinear Energy sinks for Galloping Mitigation
Auteur: Author:	Michael Makram Mousa Selwanis
Date:	2021
Type:	Mémoire ou thèse / Dissertation or Thesis
Référence: Citation:	Selwanis, M. M. M. (2021). Ball-in-Track Nonlinear Energy sinks for Galloping Mitigation [Thèse de doctorat, Polytechnique Montréal]. PolyPublie. https://publications.polymtl.ca/9747/

URL de PolyPublie: PolyPublie URL:	https://publications.polymtl.ca/9747/
Directeurs de recherche: Advisors:	Frederick Gosselin, & Cédric Béguin
Programme: Program:	Génie mécanique

POLYTECHNIQUE MONTRÉAL
affiliée à l'Université de Montréal

Ball-in-Track Nonlinear Energy Sinks for Galloping Mitigation

MICHAEL MAKRAM MOUSA SELWANIS
Département de génie mécanique

Thèse présentée en vue de l'obtention du diplôme de *Philosophiæ Doctor*
Génie mécanique

Décembre 2021

POLYTECHNIQUE MONTRÉAL
affiliée à l'Université de Montréal

Cette thèse intitulée :

Ball-in-Track Nonlinear Energy Sinks for Galloping Mitigation

présentée par **Michael Makram Mousa SELWANIS**
en vue de l'obtention du diplôme de *Philosophiæ Doctor*
a été dûment acceptée par le jury d'examen constitué de :

Njuki MUREITHI, président
Frédérick GOSSELIN, membre et directeur de recherche
Cédric BÉGUIN, membre et codirecteur de recherche
Alain BATAILLY, membre
Guilhem MICHON, membre externe

DEDICATION

To my beloved family,
specially my wonderful wife,
for her everlasting support...

ACKNOWLEDGEMENTS

I would like to express my sincere gratitude to everyone who supported me in my Ph.D. research during the last three years.

First of all, I want to thank my supervisor, Prof. Frédérick Gosselin, for his insightful guidance through all the research stages and his lasting support. I also want to express my gratitude to Prof. Cédric Béguin, my co-supervisor, for his assistance and valuable suggestions that helped me during the project. Without their supervision, the thesis would not have progressed to its presented state. I thank Prof. Guilherme Franzini for his insightful comments that improved the publications brought out from this research, as well Hongyan Miao for reviewing the thesis draft.

I want to thank all the participated interns in the project: Alexandre Medeiros and Constant Roussel, for their efforts in developing the experimental setup, as well as Sima Rishmawi, for her assistance in the image processing. I am also grateful for the assistance offered by Raed Bouslama and the help of Souheil Serroud during the free rotation tests.

I would like to thank the people at the mechanical engineering department of Polytechnique Montréal: Mr. Benedict Bésner and Mr. Aimène, for developing the Labview programs and the measuring system ; and my outstanding group, the laboratory for multiscale mechanics (LM2), for the informative technical presentations given at its regular meetings. I express my gratitude to Shibo Zou and Gaétan Raynaud, my brilliant colleagues, for their assistance in making short videos of the experiments and using the light-board. I also thank Loay Alyaldin and Mohamed Abda for the worthy discussions and for sharing the evening study times, which were also filled with fun and laughter.

I am so grateful to the Egyptian Ministry of Defense for the financial support, as well as the Natural Sciences and Engineering Research Council of Canada (NSERC) for sponsoring the current project. Special thanks to prof. Ahmed Farid Nemnem for the follow-up during my research. I want to express my sincere appreciation to Ahmed Sami Bahgat, my real friend, for his support in the hard situations during my Ph.D. journey.

Finally, I'd like to express my heartfelt thanks and respect to my wonderful wife, Nancy Samaan, for her unfailing love and everlasting support. I also want to thank my lovely kids, Martin and Robin, for their passion despite my wandering during my Ph.D. Special thanks to my big family, father, mother and brother, for their encouragement and support during this period and throughout my whole life.

RÉSUMÉ

Les vibrations induites par un écoulement doivent être considérées pour la conception des structures d'ingénierie. Le galop est un type de vibration induite par un écoulement qui se produit sur les lignes de transmission d'énergie, les faisceaux de câbles et les structures en hauteur. Ce mémoire propose une revue de la littérature qui explique brièvement le mécanisme de galop d'un prisme carré, puis aborde une revue historique sur les absorbeurs de vibrations passifs et leurs applications dans la suppression des vibrations de divers systèmes. Les suppresseurs passifs sont preferables pour leur construction simple qui ne comprend pas de capteurs ou d'actionneurs lourds. Parmi ces dispositifs, les absorbeurs d'énergie non linéaire (*Nonlinear Energy sink.* NES) n'affectent pas les caractéristiques du système primaire. Dans la présente recherche, nous introduisons un absorbeur purement non linéaire (NES) composé d'une bille se déplaçant librement sur une piste circulaire afin d'atténuer le galop d'un prisme carré. La bille est couplée à la vibration du prisme par une interaction dynamique non linéaire. Les essais en soufflerie évaluent l'impact de ce NES sur l'atténuation du galop en comparant les réponses du prisme avec et sans celui-ci. Ce NES réussit à retarder l'apparition du galop, en présentant différents modes de réponse : oscillatoire, intermittent et rotationnel. Nous définissons le comportement de la bille dans chaque régime et discutons de son effet sur la réponse du prisme. Aux faibles vitesses d'écoulement, le mode de réponse oscillatoire apparaît, dans lequel la bille et le prisme oscillent avec une faible amplitude. Pour des vitesses plus élevées, le régime intermittent apparaît dans une petite plage de vitesse comme mode de transition. À une vitesse d'écoulement encore plus élevée, la bille effectue des révolutions avec des vitesses angulaires relativement élevées dans le régime rotationnel, ce qui entraîne une forte réponse modulée du prisme. La conception simple du NES permet de modifier les dimensions de la piste en échangeant des pièces pour utiliser des billes de différentes masses et tailles. Nous illustrons donc l'effet des principaux paramètres du NES : la masse de la bille, le rayon de la piste du NES, le frottement de la bille et le jeu entre les parois de la piste du NES et la bille en rotation, sur l'amplitude du prisme et la dynamique de la bille. Un modèle proposé, utilisant les mesures du coefficient de force induites par le galop et celle de l'amortissement de la bille, simule la dynamique du prisme carré couplé avec ce NES et prévoit le comportement du système à des vitesses d'écoulement élevées au-delà des limites des expériences. Les expériences statiques en soufflerie ont permis de mesurer le coefficient de force de galop C_y en fonction de l'angle d'attaque du prisme, tandis que les essais de rotation libre ont permis de mesurer le coefficient d'amortissement de la bille c_θ. Les expériences démontrent qu'au-delà d'une certaine vitesse angulaire l'amortissement de la

balle augmente fortement. La variation de cet amortissement est un avantage du NES ; un amortissement moindre à de faibles vitesses angulaires permet à la bille de démarrer sa rotation, tandis qu'un amortissement relativement important dissipe plus d'énergie de vitesses élevées. Les simulations présentent les trois modes de réponse observés lors des expériences. En outre, elles prédisent un quatrième mode, le régime inefficace, à des vitesses d'écoulement élevées hors de la plage d'efficacité du NES. Dans ce régime, la bille tourne, de façon aleatoire dans les deux directions sans effet d'amortissement sur les amplitudes du prisme. De plus, des estimations analytiques définissent la limite du régime oscillatoire et de la plage effective du NES. La modélisation de la masse primaire comme une excitation paramétrique pour le NES fournit des amplitudes de prisme qui coïncident avec les oscillations stables de la bille, représentant la limite de transition entre les régimes oscillatoire et intermittent. Une analyse développée de la puissance transmise à travers le système intégré prisme-NES explique le comportement du NES et prédit la limite de son efficacité. Nos simulations sont en accord avec les attentes analytiques et les résultats expérimentaux. Enfin, nous utilisons plusieurs billes au lieu d'une seule grande bille de masse totale équivalente pour améliorer l'efficacité du NES. Les collisions entre les billes permettent d'absorber de l'énergie tout en changeant également la dynamique des billes du NES. L'augmentation du nombre de billes déplace le centre de masse effectif de l'ensemble des billes et encombre la piste du NES. L'essai de diverses configurations de NES à plusieurs billes de masse équivalente fournit une valeur optimale pour le taux d'encombrement de la piste. Les expériences confirment également l'efficacité accrue des NES à plusieurs billes par rapport aux NES à une seule bille. Alors qu'un NES à une bille dont la masse est de 8% de celle du prisme peut retarder la vitesse critique réduite de 68%, un NES à 2 ou 3 billes de masse équivalente retarde cette vitesse de 87%.

ABSTRACT

Flow-induced vibration (FIV) leads to critical design considerations for engineering structures. Galloping is a type of such vibration arising on power transmission lines, cables bundles and high-rising structures. The literature briefly explains the galloping mechanism of a square prism, then addresses a historical review on passive vibration absorbers and their applications in suppressing the vibration of various systems. Among these devices, nonlinear energy sinks (NESs) do not affect the characteristics of the primary system.

In the current research, we introduce a purely nonlinear energy sink (NES) composed of a ball moving freely in a circular track to mitigate the galloping of a square prism. The ball is coupled to the prism vibration through a nonlinear dynamic interaction. Wind tunnel tests assess the NES impact on mitigating the galloping by comparing the prism responses with and without the NES. The ball-in-track NES (BIT-NES) successfully delayed the galloping occurrence, exhibiting different response modes: oscillatory, intermittent, and rotational. At low flow speeds, the oscillatory responseămode arises, in which both the ball and the prism oscillate with small amplitude. The intermittent regime then appears at higher flow speeds within a small range as a transition mode. At high flow speed, the ball oscillates with relatively high angular velocities in the rotational regime, resulting in a strong modulated response of the prism. The NES simple design allows changing the track dimensions by swapping parts to use a ball of various masses and sizes. Hence, we illustrate the effect of the main NES parameters: the ball mass, NES track radius, ball friction, and radial clearance between NES track walls and the rotating ball, on the prism amplitude and the ball dynamics.

A proposed model, employing the measurements of the galloping force coefficient and the ball damping as inputs, simulates the dynamics of the square prism coupled with the BIT-NES and expects the system behaviour at high flow speeds beyond the limits of the experiments. Wind tunnel static experiments describe the galloping force coefficient C_y as a function of the prism angle of attack, while proposed free rotation tests define the ball damping coefficient c_θ. The experiments provide a certain angular speed beyond which the ball damping highly rises. The damping variation is an advantage of the BIT-NES; less damping at low angular velocities helps the ball start rotation, while relatively large damping dissipates more energy at high speeds. The simulations exhibit the three response modes observed in the experiments. Besides, it predicts a fourth mode, the random regime, at high flow speeds out of the NES effective range. In this regime, the ball rotates, alternating in both directions with no

damping effect on the prism amplitudes.

Moreover, analytical estimations define the limit boundary of the oscillatory regime and the NES effective range. Modelling the primary mass as a parametric excitation for the NES provides prism amplitudes that coincide with the ball's stable oscillations, representing the transition boundary between oscillatory and intermittent regimes. A developed power flow analysis across the integrated prism-NES system explains the NES behaviour in the rotational regime and predicts the limit of its effective range. Our simulations agree with the analytical estimations and the experimental findings.

Finally, we use multiple balls instead of a large one of equivalent mass to improve the suppression efficiency of the NES. Besides the effect of the collision between balls in absorbing energy, it interrupts the ball dynamics. Increasing the ball's number shifts the mass center and crowds the NES track. Testing various configurations of multi-ball NES of equivalent mass provides optimal value for the track crowdedness ratio. The experiments also approve the enhanced suppression efficiency of multi-ball NES compared to the single ball NES. Whereas a single ball NES with a mass 8% that of the prism can delay the critical reduced velocity by 68%, a 2 or 3-ball NES of equivalent mass delays this speed by 87%.

TABLE OF CONTENTS

LIST OF TABLES

LIST OF FIGURES

LIST OF SYMBOLS AND ACRONYMS

Symbols

A	Vibration amplitude.
$\hat{A}$	Non-dimensional vibration amplitude of the prism, $= A/D$.
A_1, A_3, A_5	Constants of the polynomial fitting of the galloping force coefficient.
α	Square prism angle of attack, $= \dot{y}/U$.
C_d	Drag coefficient.
C_l	Lift coefficient.
c	Structural damping coefficient of the prism.
c_θ	Ball damping coefficient.
c_y	System damping coefficient in y-direction.
θ	Ball angular coordinates relative to the prism.
$\dot{\theta}_c$	Ball critical speed.
D	Side length of the square prism cross section.
d_b	NES ball diameter.
δ	Logarithmic decrement, $= 2\pi\zeta_y$ for lightly damped systems.
F_D	Drag force [N].
F_d	Damping force affecting the rotating ball.
F_L	Lift force [N].
f_n	Natural frequency, $= 2\pi\omega$.
F_y	Aerodynamic force in the direction of force balance y-axis [N].
f_{vs}	Vortex shedding frequency.
φ	the arc angle
γ_t	NES track crowdedness ratio.
k	Spring stiffness.
l	Height of the square prism.
l_1	The length between the force balance and the upper end of the prism.
l_2	The length between the hinge and the lower end of the prism.
Λ	Onset velocity ratio, $= U_g/U_{vs}$.
M	Total oscillating mass.
M_x	Moment measured by force balance in x-axis direction [N.m].
m_b	NES ball mass.
$\hat{m}$	NES mass ratio, $= m_b/M+m_b$.

m^*	Mass ratio with reference to air-flow, $= {}^{M+m_b}/_{\rho L D^2}$.
μ	NES radial clearance, $= w - d_b$.
$\hat{\mu}$	Relative NES clearance, $= {}^{\mu}/_{r_b}$.
μ	Dynamic viscosity of the fluid.
ω	Natural angular frequency, $= \sqrt{{}^{k}/_{m}}$.
r	NES track mean radius.
$\hat{r}$	NES radius ratio, $= {}^{r}/_{D}$.
r_b	NES ball radius.
ρ	Airflow density $[kg/m^3]$.
ρ_c	The radius of the NES mass centre.
Re	Reynolds number, $= {}^{\rho U D}/_{\mu}$
R_1,R_2	Reaction force on the upper and the lower ends of the stationary prism in y-direction.
S_t	Strouhal number.
t	time [s].
τ	Non-dimensional time, $= \omega t$.
U	Flow velocity.
U_c	Galloping onset speed.
U_{crit}	Critical speed at which the prism amplitude reach the limit of the experimental setup.
U_g	Quasi-steady galloping reduced Velocity, $= {}^{4\,m^*\,\zeta}/_{A_1}$
U_r	Reduced flow velocity, $= {}^{U}/_{\omega D}$.
U_rel	Flow speed relative to a vibrating prism.
U_{vs}	Kármán-resonance reduced velocity, $= {}^{1}/_{S_t}$
w	NES track width
y	Displacement normal to the fow direction
Y, $\hat{Y}$	Non-dimensional vibration displacement, $= {}^{y}/_{D}$.
ζ_y	Structural damping ratio, $= {}^{c}/_{2\,(M+m_b)\,\omega}$.
ζ_θ	Ball damping ratio, $= {}^{c_\theta}/_{2 m_b r^2\,\omega}$.

Acronyms

TMD	Tuned Mass Damper.
TVA	Tuned Vibration Absorber.
FIV	Flow-Induced Vibration.
VIV	Vortex-Induced Vibration.
NES	Non-linear Energy Sink.

TET	Targeted Energy Transfer.
VI-NES	Vibro impact Non Linear Energy Sink.
BIT-NES	Ball-in-track Non Linear Energy Sink.

LIST OF APPENDICES

CHAPTER 1 INTRODUCTION

1.1 Motivation

Vibration is a typically undesired response generated by various structural and mechanical systems due to a certain excitation. This critical problem generally increases the dynamic stresses and may damage the system. Accordingly, it is a common subject in civil, mechanical, automotive, aeronautical, and many other fields of engineering. Many types of vibration arise from the fluid-structure interaction and usually lead to self-excited oscillations. Among these flow-induced vibrations (FIV), vortex-induced vibrations (VIV), flutter and galloping represent important phenomena. The textbooks written by Blevins [2] and Païdoussis et al. [3] are examples of reliable surveys on FIV. We can observe the FIV on the trembling of tree branches and the vibrations of highway mounted signages and long slender structures. Galloping amplitudes particularly increase after a certain speed in a dramatic way with the flow speed resulting in great danger on structures. Galloping was the main reason for the mass failure of the windows of the Hancock skyscraper in Boston during the construction [4]. The mounting of the huge windows was very stiff and did not consider such a critical phenomenon. As a result, the panels cracked and plummeted to the sidewalk below. This well-known catastrophe has attracted worldwide concern showing the great danger of FIV for high towers.

1.2 Development of vibration absorbers

The reduction of vibration is a great challenge for engineers to enhance system resistance against different excitations. Since Frahm [5] invented the first tuned vibration absorber (TVA), it has been widely extended to many systems for its simplicity. This device can efficiently absorb the vibration for a small range of frequencies. But, it changes the system properties by adding new frequencies. Housner et al. [6] provided an extensive review of the work done later to overcome the TMD drawbacks. A system of multiple TVAs increases the absorber damping range compared to a single one [7]. Semi-active TVAs can adapt their properties with time according to the main system frequency improving damper behaviours [8, 9]. The tunable Stiffness Absorber (TSA) is another type that adapts its stiffness for a higher working range [10, 11]. Advanced TVAs are more effective than the typical TVA. Nevertheless, they lose the advantage of being a simple and low-cost vibration absorber. Moreover, the collision of a free mass attached to a vibrating primary structure promotes energy dissipation through a complex nonlinear dynamical interaction. Depending

on this concept, the impact damper was developed by Masri [12] representing another kind of vibration suppressor applicable for broadband vibrations.

Under the class of nonlinear stiffness absorbers (NSA), nonlinear energy sinks (NES) have appeared as a more robust kind of passive suppressors. The NES consists of an auxiliary mass coupled to the primary structure by a spring element of non-linearizable stiffness and a damper. It is different from the TMD by its nonlinear stiffness that enables the device to interact with the dynamics of the primary system reducing its vibration over a higher range of frequencies [13]. The attention to the nonlinear energy absorption phenomenon has resulted in the introduction of many types of NESs. The first one is the typical translative NES that only makes a translational motion and has many configurations; the grounded NES [14], the ungrounded NES [15], the NES with limited amplitude [16], the bistable NES [17], and the multi-DOF NES [18]. The second type is the rotative NES, where a rigid arm attaches a tip mass able to rotate only [19] or makes both rotational and translational motion [20]. The Vibro-impact NES [21], the third type, appeared as an advanced NES depending on the impact of the attached mass with the primary structure walls to dissipate more energy [22]. Another type with no spring elements known as the track NES [23] utilizes a given racetrack to restrict the motion of the attached mass for the indirect coupling with the primary structure. The track shape defines a smoother non-contact restoring force of such NESs. More explanations for the behaviour of each of the NES mentioned types are to be illustrated in the literature.

Vibration absorbers exhibit different techniques for nonlinear energy absorption. Developing an efficient absorber requires the combination of more than one technique. The vibro-impact NES, as an example, combines the advantages of both an impact damper and a typical NES. It absorbs energy from a vibrating structure in two forms, kinetic energy in the motion of the NES mass and momentum transfer due to the impact of the secondary mass with a rigid wall. Thus, the vibro-impact NES is more efficient than the typical translative NES in mitigating the vibration of structures. Recently, a vibro-impact track NES [24] has appeared as a modified version of a track NES with a rigid wall on one side to limit the motion of the NES mass, using the impact between them to improve its energy absorption ability. In the same way, the bistable track NES [25] combines the advantages of both the bistable NES and the track NES showing an efficient and practical NES of two stable equilibrium points. The suppressor using more than one technique for energy absorption improves its suppression capability and increases its effective range.

1.3 NES applications

The NES firstly appeared as a suppressor for structures under impulsive load [26]. Hence, it has been implemented as a vibration absorber in several engineering applications, including civil engineering structures, mechanical systems, aeronautics and energy harvesting. In the civil engineering field, the NES controls the structural response due to seismic excitation [27, 28], and mitigates the vibrations of buildings during earthquakes [29]. The NES also absorbs the vibration of structural elements such as beams [30], and plates [31]. Many studies applied the NES as a suppressor in mechanical systems; flywheel [32], rotary systems [33], and self-excited systems [34]. The NES as well damps the vibrations of the helicopter blades [35]. In addition to the NES damping effect, integrating such oscillators in a magneto-electric [36], or a piezoelectric [37] systems is a technique to harvest the energy of an oscillating system.

Regarding the mitigation of FIV, the NES could delay the flutter instability of wings [38, 39], mitigate the oscillations of pipes conveying fluid [40]. NES designs as well have been coupled with cylindrical structures to reduce the danger of wind-induced vibrations. A numerical study [41] addressed the effect of a translative NES on the vortex-induced vibration (VIV) of a cylinder. The NES could reduce the vortex shedding amplitudes to 75 % of its original value. Mehmood et al. [42] discussed the great effect of the initial conditions on the suppression efficiency of the NES. Further, Dai et al. [43] adopted the wake-oscillator models to estimate the fluid forces due to VIV and demonstrated how the energy transfer with the translative NES strongly modulated the cylinder dynamics. In a comparable study, Blanchard et al. [44] conversely estimated the fluid loads using computational fluid dynamics (CFD) and illustrated that a rotative NES likewise modulates the cylinder response. NES parameters, particularly the mass, have a great effect on its suppression efficiency [45]. Only a few researchers have advanced the NES as a passive absorber for transverse galloping. A numerical study [46] examined the impact of a translative NES in delaying the occurrence of square prism galloping, illustrating the effect of NES parameters variation on its behaviour. In a comparable problem, Teixeira et al. [47] reported a 50 % reduction in the prism galloping amplitudes by using a rotative NES.

Despite the number of theoretical investigations addressing the feasibility of such vibration absorbers in various applications, experimental works were much less and most of them introduced the NES as a vibration absorber for buildings [18, 48]. Regarding the mitigation of FIV, Dongyang et al. [49], Dai et al. [43] only validated the VIV model of the cylinder without the suppression effect of the NES. No considerable contributions, at least to our knowledge, exist in terms of the experimental mitigation of galloping by NES.

1.4 Ball-in-track configuration

Referring to an interesting phenomenon, a free ball in a circular track can efficiently reduce rotor vibration generated from system imbalance at high rotating speeds [50]. The Automatic Ball Balancer (ABB) represents a passive balancer found in washing machines and optical disks. I experimentally validated the effect of ABB in reducing rotors vibration during my master's research. Contrary to the NES, the ball in this balancer moves to find the desired position counteracting the system imbalance. This concept is different from the NES theory that depends on the ball rotation to absorb energy from the vibrating system. However, the simple structure of ABB is inspiring for the design of a purely rotative NES with no direct coupling to the primary structure.

1.5 Originality and Impact

The originality of this work is to provide a purely rotative nonlinear energy sink (NES) depending on the ball-in-track NES configuration. Although the structure of the proposed NES resembles that of the ABB, their concepts are different. The ABB is a balancer in which the balls tend to reach positions counteracting the system imbalance then stops relative to the rotor. This balancer works properly at high angular speeds beyond the critical speed of the rotor, as the balls tend to move away from the imbalance mass. Differently, the ball of the NES rotates due to a dynamic coupling with the primary structure to absorb and dissipate its vibrational energy. The idea of using a multi-ball NES to benefit from the collisions between them as an additional mechanism for energy absorption has not been considered before.

The current research dives from the realm of conceptual and theoretical studies into the real physical world with a working prototype for the ball-in-track NES. The simple structure and the low fabrication cost of the proposed NES may extend its applicability to many systems. It can mitigate wind-induced vibrations of power lines and sign support structures. With further investigations, considering a large scale for the ball-in-track NES, it can play the same role as the tuned mass damper in absorbing the vibration of skyscrapers and other civil engineering structures.

1.6 Research question

This research discusses the advantages of passive vibration absorbers and aims to contribute a simple, economical suppressor applicable for practical implementation in many systems.

We introduce a free ball rotating in a circular track race as a purely rotative NES. Hence, the current study answers the following questions :

- Can the ball-in-track rotative NES mitigate the galloping of a square prism?
- What is the key parameter of the proposed NES and how does it affect its behaviour?
- Is the ball friction with the NES track enough for the dissipation of vibrational energy?
- How does the energy transfer across the integrated prism-NES system?
- What is the maximum power capacity of the NES?
- How does the usage of multiple balls influence the NES suppression efficiency?
- Are the collisions between balls beneficial in a multi-ball NES?

1.7 Thesis structure

The current thesis includes seven chapters, each one starts with a brief introduction exposing the goals of the related content and ends with a summary of the main findings. Following the introduction chapter, we structured the thesis as follows.

- **Chapter 2 - Literature Review -** briefly explains the galloping mechanism of a square prism and introduces different types of vibration absorbers, including tuned mass damper, quasi-zero stiffness isolator, impact damper, and nonlinear energy sink. Moreover, it addresses the NES various designs and how it was adopted as a suppressor for FIV.

- **Chapter 3 - Problem Statement -** identifies the problem and the objectives of our research.

- **Chapter 4 - Wind Tunnel Demonstration of Galloping Mitigation with a Purely Nonlinear Energy Sink -** presents the design of a purely rotative NES and the experimental setup of the wind tunnel tests that demonstrated the effect of the proposed NES on mitigating the galloping of a square prism. The experiments showed variable dynamics experienced by the NES at different flow speeds and the influence of main NES parameters on its behaviour.

- **Chapter 5 - How a ball free to orbit in a circular track mitigates the galloping of a square prism -** explains the methodology used in simulating the dynamics of the prism-NES system employing the experimental data measured for the galloping force and the ball damping coefficients as inputs for a numerical model. The proposed free rotation tests provide an efficient way for measuring the damping of rotating particles. Moreover, this chapter addresses analytical estimations for the transition boundary between NES

regimes. A proposed power analysis came up with an analytical expression for the NES maximum power analysis, thus expects a limit for its effective range.

- **Chapter 6 - Multi balls rotating in a circular track experimentally mitigate the galloping of a square prism -** illustrates the advantage of using multiple balls, instead of a large one of equivalent mass, in improving the suppression efficiency of the NES through wind tunnel experiments. Furthermore, it highlights the NES crowdedness ratio and the maximum radius of the NES mass center as key parameters affecting the behaviour of a multi-ball NES.

- **Chapter 7 - General Discussion -** explains the findings of the whole study and compares the simulation results with the analytical estimations and the experimental results.

- **Chapter 8 - Conclusions and future work -** brings the main contributions of the research, pointing out the limitations and the expected future work. Finally, it addresses the publications that came out of this project.

CHAPTER 2 LITERATURE REVIEW

The literature starts with a brief description of the galloping phenomenon of a square prism describing the leading parameters of this instability. That is followed by a review of the different kinds of passive vibration absorbers. We start with the linear TMD and present other nonlinear absorbers that appeared to overcome the limitation of the TMD effective range as the quasi-zero stiffness isolators and impact dampers. Moreover, a wide class of nonlinear energy sinks (NESs) have received exceptional interest and been developed in many configurations. The literature outlines the various designs and applications of NESs, coming up with a new design idea of a simple-structured rotative NES.

2.1 Galloping Phenomenon

Galloping instability is a type of flow-induced vibration (FIV) characterized by low-frequency and high amplitude. Lanchester [51] was the first to describe galloping of a D-section prism with a flat surface that resembles the shape formed during the icing of power lines. Galloping appears in different forms [52]; transverse galloping of high structures and power lines, torsional galloping appeared in bridge decks and the flutter of wings. The structure cross-section significantly affects the instability characteristics [53]; the square prism (rectangular prism with side ratio 1) only experiences a high-speed galloping or vortex shedding in the transverse direction to the flow. In general, galloping occurs at relatively high speeds, after which the amplitude of the oscillations increases dramatically with the flow speed.

2.1.1 Galloping mechanism of a square prism

Following the textbook of Païdoussis et al. [3], we considered an elastically mounted square prism of a side length D allowed only to oscillate in the transverse direction to a steady flow (Figure 2.1). The prism vibration about its static equilibrium position changes its velocity relative to the flow according to the relative angle of attack α.

$$\alpha = \tan\left(\frac{\dot{y}}{U}\right), \tag{2.1}$$

where y is the prism displacement, $(\dot{\cdot})$ means derivative with respect to time and U is the flow velocity. The flow affects the square prism by two forces: a drag force F_D always in relative direction of the flow and a lift force F_L perpendicular to it. The resolution of these

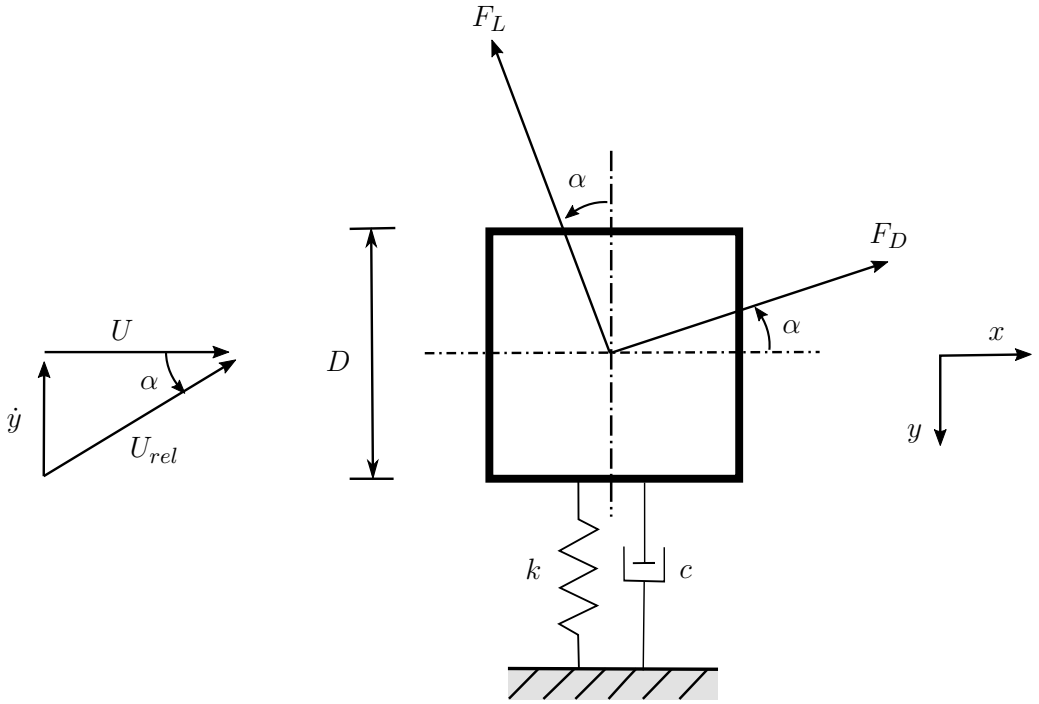

Figure 2.1 Galloping mechanism of a square prism, mounted by an elastic dissipative support of stiffness k and damping coefficient c. The prism is free to oscillate in the y direction transversely to the flow of speed U, U_{rel} is the flow speed relative to a prism vibrates by a velocity $\dot{y}$.

non-dimensional forces in the direction of the prism vibration provides a transverse force F_y. F_y varies as a function of the flow density ρ and speed U and the square prism side length D,

$$F_y = -F_L\, cos\alpha - F_D\, sin\alpha = \frac{1}{2}\,\rho U^2\, D\, C_y. \tag{2.2}$$

To evaluate the stability of an undamped system, we focus on the derivative of the transverse force to the angle of attack $\frac{\mathrm{d}F_y}{\mathrm{d}\alpha}$. An increase in the square prism oscillating velocity ($\dot{y} \uparrow$) raises the relative angle of attack ($\alpha \uparrow$). For negative derivative $\frac{\mathrm{d}F_y}{\mathrm{d}\alpha} < 0$, when the angle of attack increases ($\alpha \uparrow$), transverse force affecting the square prism decreases ($F_y \downarrow$). On contrary, any increase in the velocity increases the normal force component if the system is unstable when $\frac{\mathrm{d}F_y}{\mathrm{d}\alpha} > 0$. That briefly explains the galloping instability phenomena of a square prism.

For an elastically supported square prism of mass per unit length m, and side length D. The

equation of motion in the y-direction describes the galloping mechanism,

$$m\ddot{y} + 2m\omega\zeta\dot{y} + m\omega^2 y = \frac{1}{2}\,\rho U^2\, D\, C_y. \tag{2.3}$$

where ζ and ω are the damping ratio and natural frequency $[rad/s]$, and C_y is the normal force coefficient. This coefficient varies with the relative angle of attack and can be expanded in a Taylor series considering a small angle of attack $\alpha \simeq 0$:

$$C_y = C_y|_{\alpha_o} + \frac{\partial C_y}{\partial \alpha}|_{\alpha_o}\,\alpha + 0\left(\alpha^2\right) + \ldots\,, \tag{2.4}$$

By substituting in equation 2.3, we get

$$m\ddot{y} + 2m\omega\left(\zeta - \frac{\rho U U^2 D}{4m\omega}\,\frac{\partial C_y}{\partial \alpha}|_{\alpha_o}\right)\dot{y} + m\omega^2 y = \frac{1}{2}\,\rho U^2\, D\, C_y|_{\alpha_o}. \tag{2.5}$$

The expression between brackets represents the total damping of the system, which equals the sum of the aerodynamic damping and the structural damping,

$$\zeta_{tot} = \zeta - \frac{\rho U D}{4m\omega}\,\frac{\partial C_y}{\partial \alpha}|_{\alpha_o}. \tag{2.6}$$

The total damping term plays a significant role in system instability. As long as it is positive, the system remains stable. From this term, we can estimate the galloping onset speed U_g^* that corresponds to zero damping $\zeta = 0$ as

$$U_g^* = \frac{U_{crit}}{f_n D} = \frac{4m(2\pi)\zeta}{\rho D^2}\left(\frac{\partial C_y}{\partial \alpha}\right)^{-1}. \tag{2.7}$$

Where f_n is the natural frequency in Hz $(\omega/2\pi)$.

2.1.2 Quasi-steady approach

The variation of the normal force coefficient C_y relative to the angle of attack α is a principal parameter in the square prism galloping. Since the prism vibration is slow compared to the flow speed, the force coefficients of the vibrating prism are equal to the values measured statically at the modified angles of attack in the wind tunnel, according to the Quasi-steady approach. Depending on measurements of the normal force coefficient of a square prism C_y

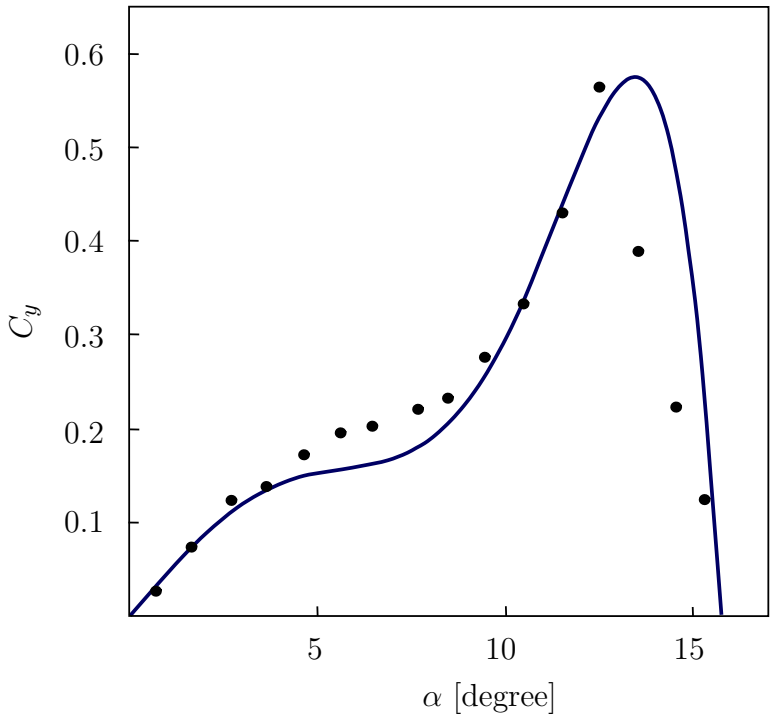

Figure 2.2 C_y variation with square prism angle of attack [54] ; ● experimental data , ——7^{th} order polynomial fitting (A_1 = 2.69, A_3 = -168, A_5 = 6270, A_7 = -59900).

at different angles of attack, Parkinson and Smith [54] obtained a polynomial fitting :

$$C_y = A_1 \left(\frac{\dot{y}}{U}\right) + A_3 \left(\frac{\dot{y}}{U}\right)^3 + A_5 \left(\frac{\dot{y}}{U}\right)^5 + A_7 \left(\frac{\dot{y}}{U}\right)^7. \tag{2.8}$$

Where, A_1, A_2 and A_3 are constants obtained from the fitting of experimental data.

After the substitution with the polynomial of C_y, Parkinson and Smith [54] solved the system governing equation presenting the square prism amplitude response, galloping onset speed, and hysteresis phenomena during transverse galloping. Figure 2.3 shows two stable limit cycles obtained from the directions of increasing or decreasing the flow velocities. The prism response in the region between U_1 and U_2 is variable depending on the initial conditions. We may have a stable limit cycle (small or large) or an unstable cycle.

This approach is convenient only for pure galloping. However, it is not applicable in the region of interference by vortex shedding. Thus, Parkinson found that the quasi-steady approach is quite applicable when $U/f_n D \geq 30$ [55].

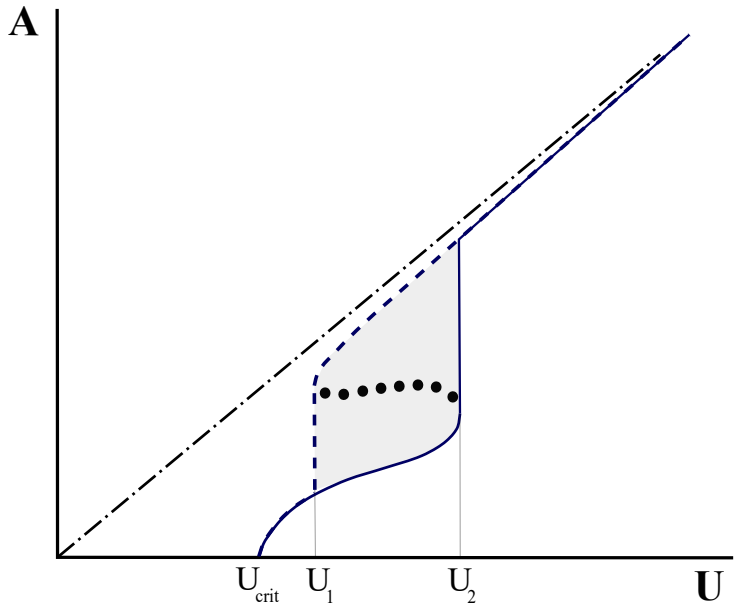

Figure 2.3 A square prism response during galloping [54] ; ——increasing flow velocity, – – – decreasing flow velocity, ● unstable cycle.

2.1.3 Normal force coefficient estimation

Parkinson and Smith fitting, obtained from their experiments, is commonly used for simulating the galloping of square prism [46, 47]. However, we can find other published data presenting different measurements for the normal force coefficient of a square prism. For that reason, Bearman et al. [56] compared some measurements for C_y and reported a minimum deviation of ± 10 in the value of A_1 required as an input of the quasi-steady approach (equation 2.8). In Figure 2.4, we present experimental data of C_y measured by Naudascher et al. [57], Wawzonek [58], Bearman et al. [56] and Parkinson and Smith [54]. The slope of the curve at zero angles of attack is not constant for the different measurements. Moreover, the maximum value of C_y measured by Naudascher is 0.4 corresponding to an angle of nearly 11^o. While Parkinson and Wawzonek measured a maximum c_y of 0.55 at different angles of attack 12^o and 13^o, respectively. The deviation in the measurements of C_y might arise due to the difference in Reynolds number or measurement accuracy. Besides, most of these experiments have been performed in the last century without reporting the measurement uncertainties.

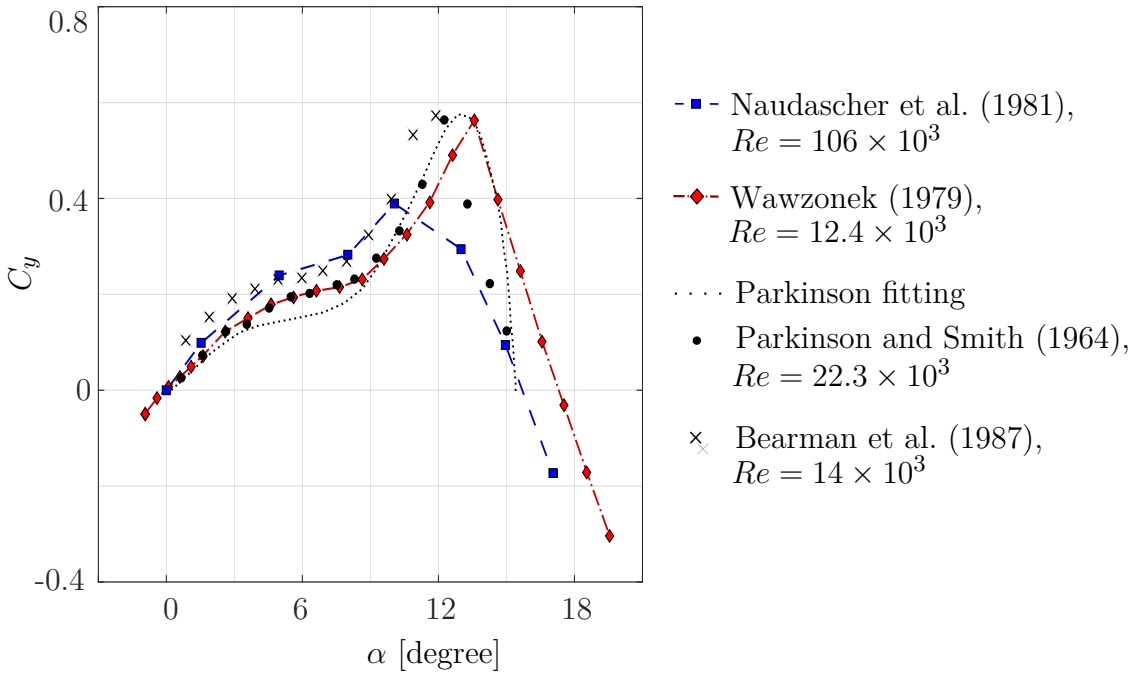

Figure 2.4 C_y variation with square prism angle of attack α.

2.2 Types of vibration absorbers

2.2.1 The Tunned Vibration Absorber (TVA)

Housner et al. [6] provided an extensive review of the work done regarding TVA, which was referred as Tuned Mass Damper (TMD) in some references. The TVA is a mass attachment with a spring element and proper damping properties to keep the mass motion out of phase with the principle system vibration. TVA effectively suppresses vibration only in narrow-band near its natural frequency [59, 60]. The TMD is used to eliminate the first vibrational mode in several systems. The main drawback of this absorber is changing the characteristics of the primary system by adding new frequencies due to its linear stiffness (Figure 2.5). Besides, such absorbers require accurate tunning with the system parameters, which is difficult to remain with the system ageing.

To overcome the drawbacks of the classical TVA, researchers introduced other configurations for the TVA. A system of multiple TVAs increases the absorber damping range compared to the single one [7]. The semi-active TVAs can adapt their properties with time according to the main system frequency improving damper behaviors [8, 9]. Tunable Stiffness Absorber (TSA) is another type that adapts its stiffness for a higher working range [10, 11]. The

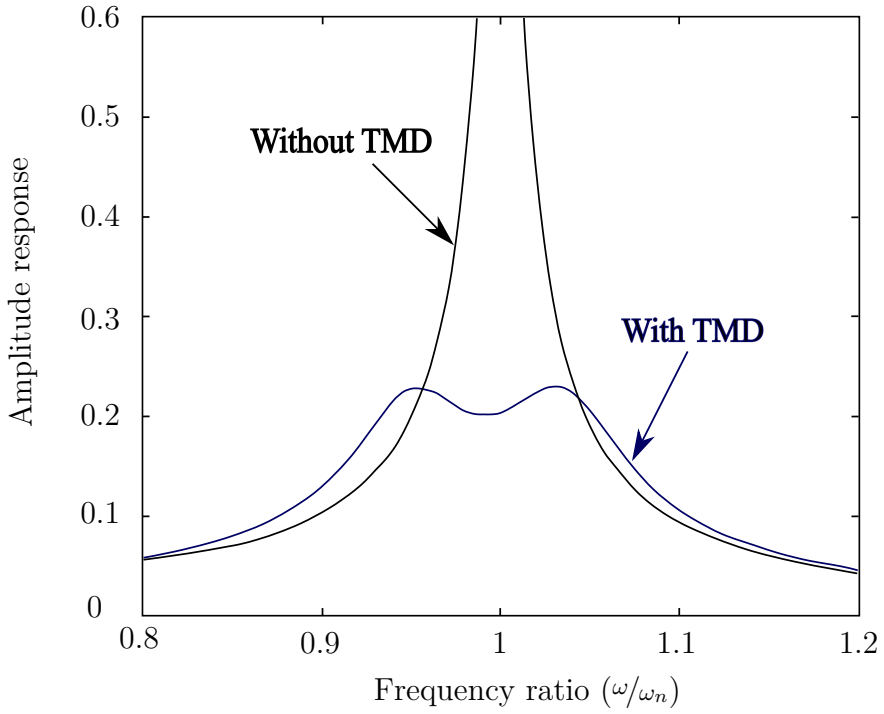

Figure 2.5 Frequency response apmlitudes for a single DOF structure with and without a TMD [1].

advanced TVAs are more complicated contraptions that lose the typical TVA's advantage as a simple and low-cost vibration absorber.

2.2.2 The Quasi-Zero Stiffness Absorbers (QZS)

The design of these oscillators aims to minimise dynamic stiffness at the equilibrium position to enable the oscillator excitation by low-frequency vibrations. For this reason, some references refered to it as an ultra-low frequency vibration isolator [61]. Minimizing the stiffness reduces the natural frequency of a quasi-zero stiffness absorber but results in high static deflection. Combining the oscillator positive stiffness with a spring element of negative stiffness reduces the dynamic stiffness, and prevents the undesired deflection. The quasi-zero stiffness absorbers generally gain their non-linearity from the initial geometry of the spring's configuration [62]. While the advanced type of such absorbers combines the physical nonlinear stiffness of the springs [63] or buckled beams [63] with the non-linearity of the geometry to improve the oscillator characteristics.

Figure 2.6 a shows a common mechanism of these vibration isolators in the unloaded condition, where two oblique springs are used with a vertical spring. The designer optimized system

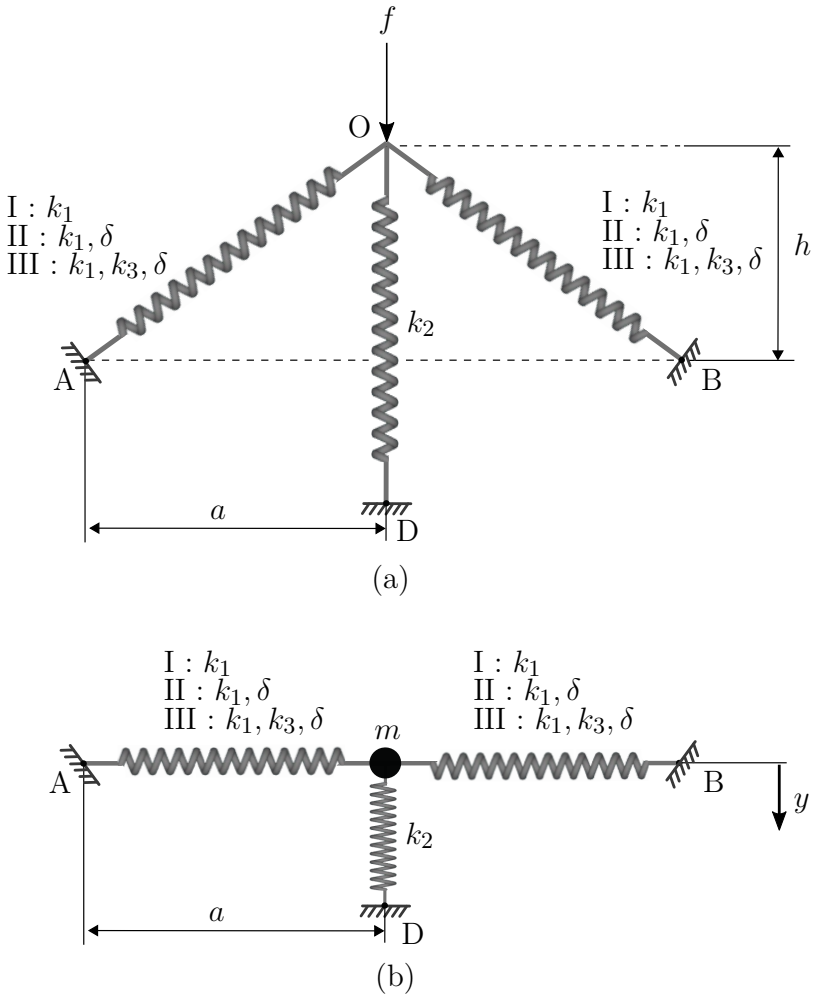

Figure 2.6 A three-spring model of a quasi-zero stiffness mechanism [64]. (a) Unloaded condition, (b) Loaded with a mass.

properties of the spring stiffness k, initial geometry (a, h) and pre-stress (δ) for obtaining zero dynamic stiffness in the loaded condition, after adding the supported mass m (Figure 2.6 b). A considerable study [64] provided a dynamic analysis for the mentioned mechanism considering linear stiffness for the vertical spring k_1 and three different configurations for the oblique springs; linear springs k_1 either without pre-stress I or with pre-stress II, or nonlinear springs k_1, k_3 with pre-stress III. The nonlinear pre-stressed springs improved the oscillator behaviours by decreasing the minimum exciting frequency of the oscillator.

2.2.3 Impact Damper

Impact damper is another absorber that mitigates the vibration due to a momentum transfer from the primary structure to the free mass. There are various configurations for the impact dampers. For the typical single unit damper (Figure 2.7 a), optimal energy absorption required a free mass of $10 - 15\%$ of the total mass of the structure and a clearance of $10 - 20$ times the main excitation amplitude of the primary structure [65]. In the multi-unit damper (Figure 2.7 b), multiple masses are used instead of a larger single one. The multi-unit damper is more beneficial than the single-unit damper in mitigating vibration and noise due to the lower contact forces of small masses that facilitate its motion [12]. Another type of lower noise level is the bean bag impact damper [67] which consists of a flexible bag filled with small particles. Figure 2.7 d presents the particle impact damper [68] that consists of small metal particles filling cavities of the primary structure. Adding spring-damper systems can absorb impact forces and increase the collision time, improving the behaviour of the damper in the two advanced types: the resilient impact damper [69] and the buffered impact damper [70, 71] (Figures 2.7 e and f, respectively). Another type consists of a series of large and small balls shown in Figure 2.7 g is called the linear particle chain [66]. The multiple collisions of small and large balls during vibration dissipate the kinetic energy and improve the behaviour of the damper compared to the single impact damper.

The energy absorbed by the impact damper depends on the number of effective collisions [65] between the free ball and the walls of the vibrating structure. The high noise and effect of impact on shortening the structure life are the main drawbacks of the impact damper. Furthermore, primary system dynamics and the kind of excitation strongly affect its behaviour.

2.2.4 Nonlinear Energy Sink (NES)

Another type of nonlinear stiffness absorbers is the nonlinear energy sink (NES), which typically consists of a mass attached to a spring element of nonlinear stiffness and almost a linear damper (Figure 2.9). The absence of a linear natural frequency [13] enables the NES to interact with the dynamics of a primary system over a broad range of frequencies, which is a considerable advantage for the NES over other types of vibration absorbers. The NES firstly appeared as a vibration absorber for structures [72]. During structure vibration, a portion of the vibrational energy is transferred irreversibly from the primary system to the NES, reducing the vibration amplitudes. This key-concept has been known as Targeted Energy Transfer (TET) [73].

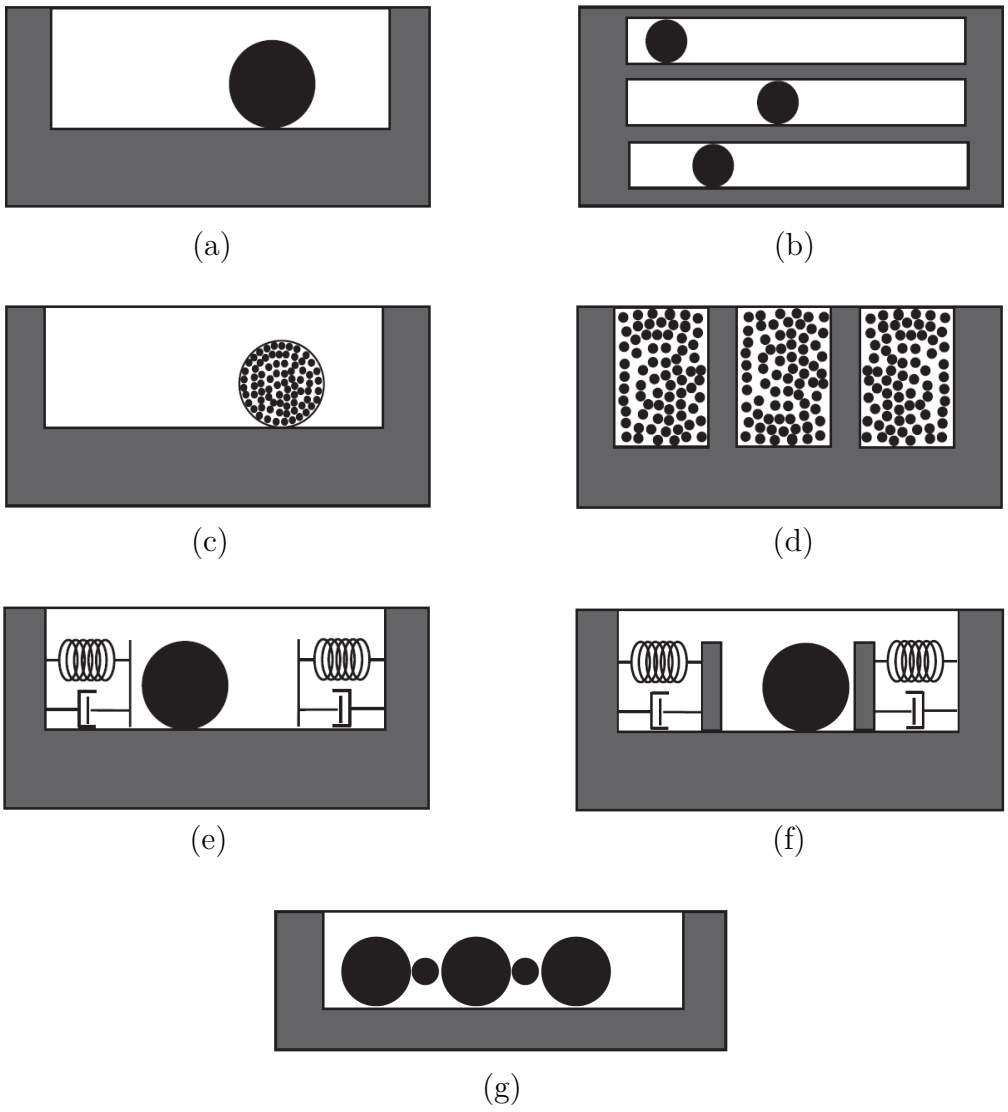

Figure 2.7 Different types of impact dampers [66] ; (a)single unit impact damper, (b) multi unit impact damper, (c) bean bag impact damper, (d) particle/granular impact damper, (e) resilient impact damper, and (f) buffered impact damper.

Targeted energy transfer (TET)

Gendelman [74] observed this phenomenon in a weakly coupled 2-DOF system of a linear damped oscillator (acted as a primary system) and a NES, referring to it as nonlinear energy pumping. A further study [75] numerically analyzed the energy transfer behaviour between the linear oscillator (LO) and a NES at three different energy levels. Figure 2.8 shows the transient responses of both the linear oscillator and the NES due to the direct excitation of the first one, where h is the non-dimensional energy at t=0. Both oscillators showed free damped vibration at the low initial energy level (Figure 2.8 a). Contrarily, the higher initial energy levels resulted in a transfer of energy from the primary system to the NES. After a certain time, the NES absorbed most of the system energy (Figure 2.8 b, c).

Gendelman et al. extended their study to a second part [76] through a resonance capture analysis for the same coupled system. They found that an advantage of the nonlinear stiffness enables the NES to adapt its properties and engage with the dynamics of the primary system. Thus, the NES experiences high-speed oscillations nearly at the resonance frequency of the primary system.

2.3 Classification of nonlinear energy sinks (NESs)

2.3.1 Translative NES

The typical NES [72] consists of a small mass attached to the main structure by an essentially nonlinear spring and a dashpot. This mass is allowed only to make a transnational motion during the system excitation. The great interest in the field of nonlinear energy absorption has continued for the last two decades leading to various configurations of the translative NES.

Grounded Configuration

Vakakis [72] demonstrated the nonlinear TET phenomena in a coupled system of multi-linear oscillators. This study introduced a nonlinear energy sink (NES) in a grounded configuration (Figure 2.9 a), where the NES mass is attached by a nonlinear spring element and a linear damper to the ground and by a linear stiffness spring to the primary structure. The NES was able to mitigate the system vibration during an impulsive load. This study extended the usage of the NES to a multi-DOF system and pointed out the applicability of using an NES as a shock absorber for large structures. Later, Vakakis et al. [77] addressed the importance of the NES damping properties for the dissipation of the transferred energy from a primary

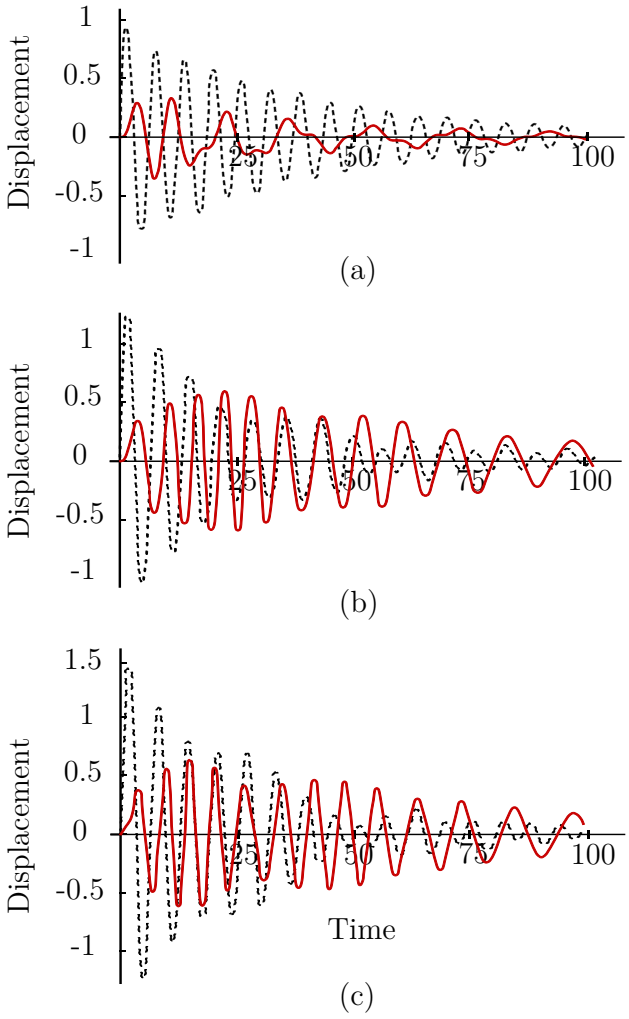

Figure 2.8 Non-dimensional transient responses of a linear oscillator (- - -) and a NES (——) in a weakly coupled system at different excitation levels [75] (a) h=0.5, (b) h=0.8, and (c) h=1.25.

system of linear oscillators. The energy of the NES returns to the primary system in the case of insufficient NES damping. In the same year, Vakakis [78] highlighted the zero nonlinear frequency component of the NES as an essential factor for energy pumping that enables it to engage with the system resonance in any mode.

Returning to the 2-DOF system of weakly coupled linear oscillator and a NES [14], the absence of NES linear natural frequency leads to the appearance of synchronous motions (nonlinear normal modes). These dynamics result in the resonance capture phenomena in certain conditions using a damped NES [79]. In a later study, an analytical and numerical analysis for the dynamics of the given system [80] provided a wide range of system parameters

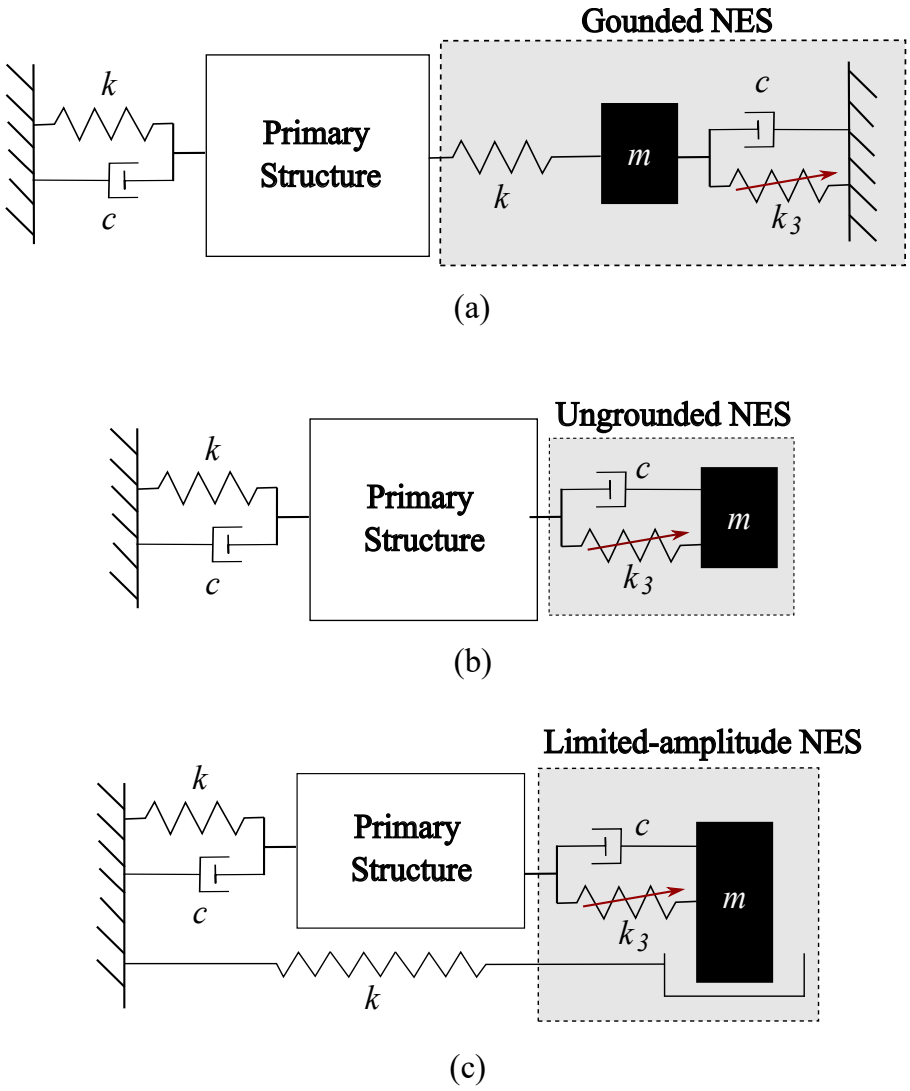

Figure 2.9 Different NES configurations : (a) grounded NES, (b) ungroundedd NES, (c) limited-amplitude NES.

where the energy can successfully transfer over the coupled system.

Energy transfer still occurs with uncertain system parameters [81]. However, optimization techniques could define the best ranges for the system parameters and initial conditions that achieve the ideal transfer of energy between a linear oscillator and a NES [82]. Moreover, introducing any non-smooth friction in the dynamics of the primary structure affects the TET efficiency [83]. By considering these non-smooth terms in the design, we can obtain a more efficient NES.

Ungrounded Configuration

The unground NES appeared as a simpler configuration of the NES [84]. Despite using a relatively lighter mass attachment in such a configuration (Figure 2.9 b), it resulted in two mechanisms of pumping. The first one showed a 1:1 resonance capture for the NES and a primary system of a linear oscillator, while the second exhibited a series of sub-harmonic frequencies. The energy pumping in the system was initiated by nonlinear beats that activated one of the two mentioned mechanisms. That was also studied analytically considering different energy levels of impulsive oscillations in an extended study [85]. Under some conditions, both the different configurations of the grounded and the ungrounded NESs may lead to the same system dynamics [15]. However, the grounded NES can improve the energy pumping phenomena according to the design parameters [86]. A series of studies [87, 88, 89] addressed the favourable system parameters and initial conditions required for the ideal irreversible TET. A later study [90] introduced some analytical formulas to describe the decay in displacement, velocity, and energy of the NES.

Sapsis et al. [91] used oblique intentional springs, similar to what is seen in the quasi-stiffness absorbers, and dampers to introduce three different configurations of NESs. The stiffness nonlinearity came from the initial geometry of springs (Figure 2.10). In this study, the zero linear stiffness component of the proposed NESs enabled resonance interaction at several modes over a wide range of frequencies. The damping nonlinearity enhanced the effective damping of the primary structure with no considerable effect on the effective stiffness.

NES with limited amplitude

Due to the absence of linear stiffness, the expected high amplitude of the ungrounded NES was inacceptable in many applications. Geng et al. [16] developed a limited-amplitude NES by adding a linear stiffness spring restricting the motion of the NES mass to limit the NES amplitude (Figure 2.9 c). The numerical simulations illustrated that introducing piecewise spring in the limited-amplitude NES weakened its vibration suppression effect. However, the optimization of the piecewise stiffness and the gap width between the linear stiffness spring and the NES mass highly improved the behaviour of such a NES. Moreover, the experiments validated the suppression effect of the limited-amplitude NES and its sensitivity to the added linear stiffness and the gap width. Limiting the NES amplitudes reduces its space requirement and expands its applicability to more systems.

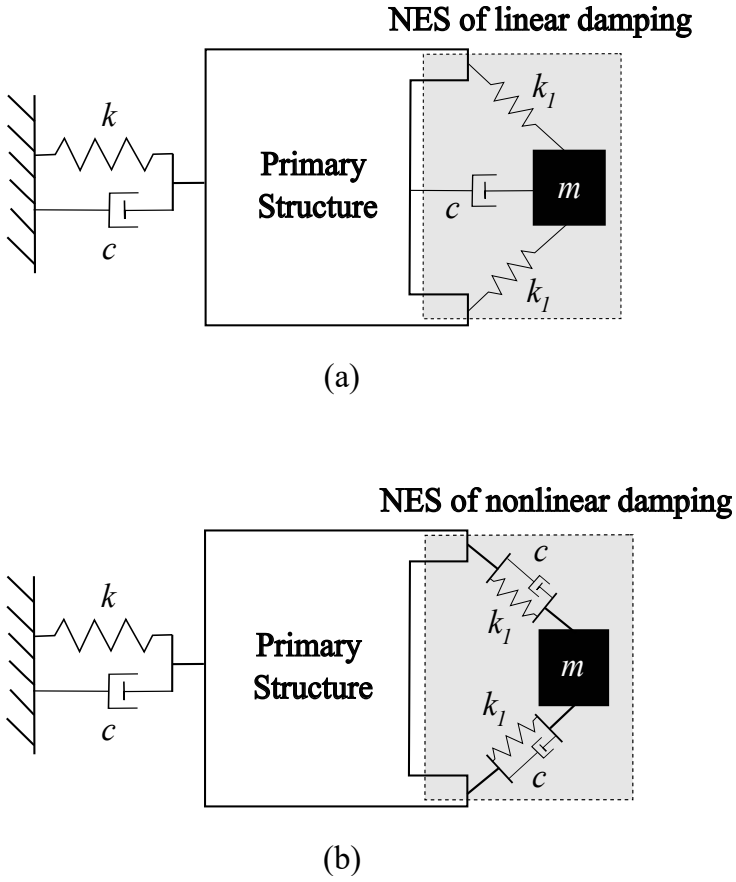

Figure 2.10 NES different configurations experience its non-linearity from the geometry of its configuration (a) NES with linear damping, and (b) NES with nonlinear damping.

Bi-stable NES

AL-Shudeifat [17] improved the NES behaviour by changing the geometry of the springs attaching the NES mass to add a negative stiffness component (Figure 2.11). At low energy levels, the modified NES vibrated around its initial position. While increasing the excitation energy level surprisingly raised the NES stroke to find another equilibrium position at the right side (Figure 2.11 b). The bi-stability increased the capacity of the translative NES showing a considerable improvement in the NES robustness. The bi-stable NES could absorb 97-99% of the energy of the primary structure over a wide range of energy levels [17]. Fang et al. [92] provided a deeper view of the dynamics of the bi-stable NES through an analytical and experimental study. The author presented a different configuration of a bi-stable NES using an Euler beam as a spring element. The experiments validated all the mentioned dynamics of the bi-stability, the resonance capture, and the nonlinear oscillations.

The bi-stable NES is a more stabilized vibration absorber, even out of the tuning range, com-

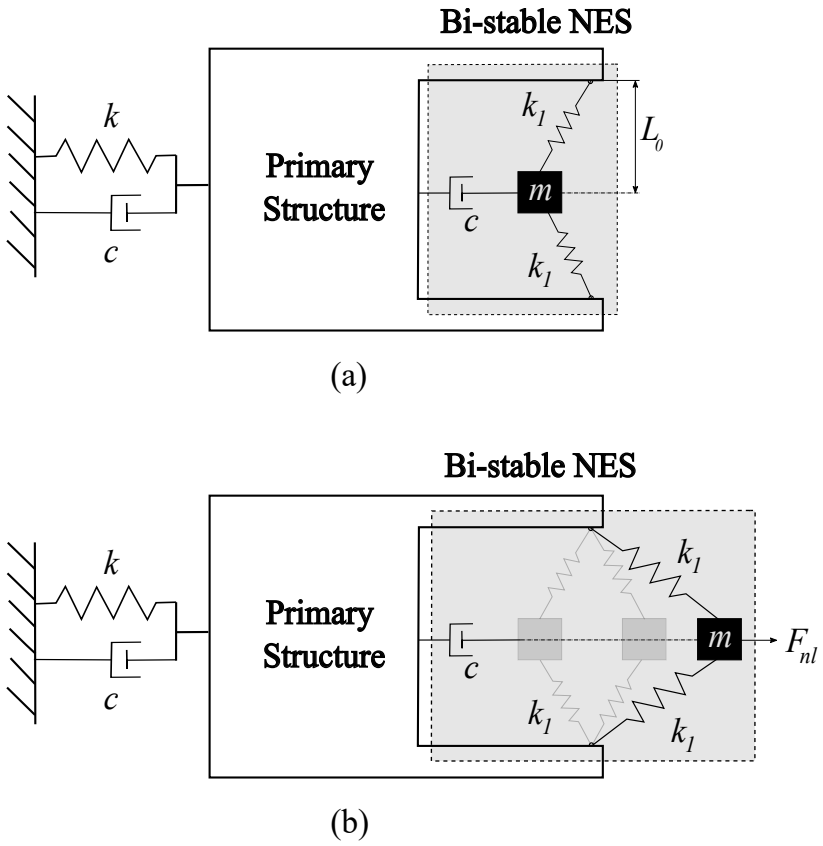

Figure 2.11 Bi-stable NES (a) unloaded, (b) at high energy levels

pared to the cubic-stiffness NES and the linear TMD [93]. Nevertheless, later work enhanced the behaviour of the bistable NES by optimizing its parameters. Qiu et al. [94] applied the multiple scales method to study a periodically excited system of a linear oscillator coupled with a bi-stable NES. The bi-stable NES was robust over a wide range of exciting amplitudes and experienced four different response modes depending on the energy level. This study confirmed that the $1:1$ resonance capture phenomenon results in an efficient energy transfer, arguing that $1:3$ sub-harmonic resonance can benefit the energy transfer. Moreover, it addressed a criterion for the optimum design of bi-stable NES. Recently, an interesting study [27] introduced permanent magnets, generating a non-contact restoring force in and smoother way, to replace springs of the bi-stable NES. That magnetic bi-stable NES showed a better transient response when coupled with a primary structure under a seismic load. Finally, we can say that the bi-stable NES improves the TET phenomena compared to the typical NES over a broad range of energy levels but with more complex mechanisms.

Multi-DOF NES

The multi-DOF NES (Figure 2.12), introduced by Tsakirtzis et al. [95], absorbs energy at different frequencies contrary to the resonance capture phenomenon observed for the single-DOF NES. Musienko et al. [96] provided the design procedures for a multi-DOF NES and explained its advantage. The author showed that the interaction between the two oscillators of lighter mass attachments enhanced the efficiency of energy pumping, reducing the displacements of the two oscillators below that of the primary system. Besides, the multi-DOF NES broadened the range of energy levels at which the TET can occur [97]. A comparison between three different configurations of multi-ball NESs [91], presented in Figure 2.10, confirmed that the 2-DOF NES was more effective in the absorption of impulsive load, showing slow and fast energy transfer over a wide range of initial excitations. An experimental study [18] validated the high effectiveness of a 2-DOF NES in damping impulsive excitation over a wide range of initial energy levels. Although the multi-DOF NES can enhance the energy pumping phenomenon, it increases the complexity of the NES dynamics.

2.3.2 Vibro-impact NES (VI-NES)

Refs. [21, 98] described a similar structure of a single unit impact damper as a VI-NES, showing the effect of ball impact in mitigating the vibration that resulted from a harmonically forced linear oscillator. Tao et al. [99] highlighted the chaotic characteristics of a linear oscillator coupled with a VI-NES with no spring elements. The multi-unit impact damper also appeared as two parallel VI-NESs in another study [100] showing its efficiency in the vibration reduction compared to a single VI-NES.

The VI-NES combining the advantages of both the translative NES and the impact damper has appeared in various studies. Figure 2.13 shows two different configurations of the single

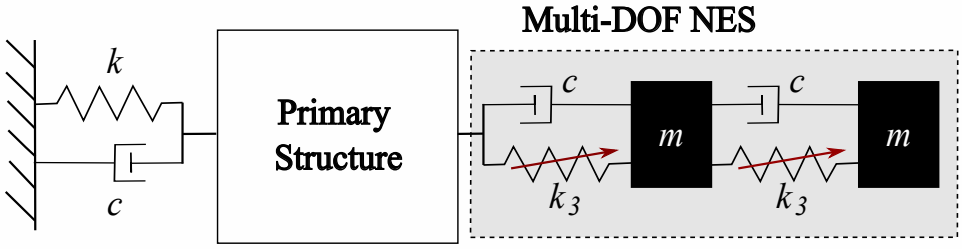

Figure 2.12 Multi-DOF NES

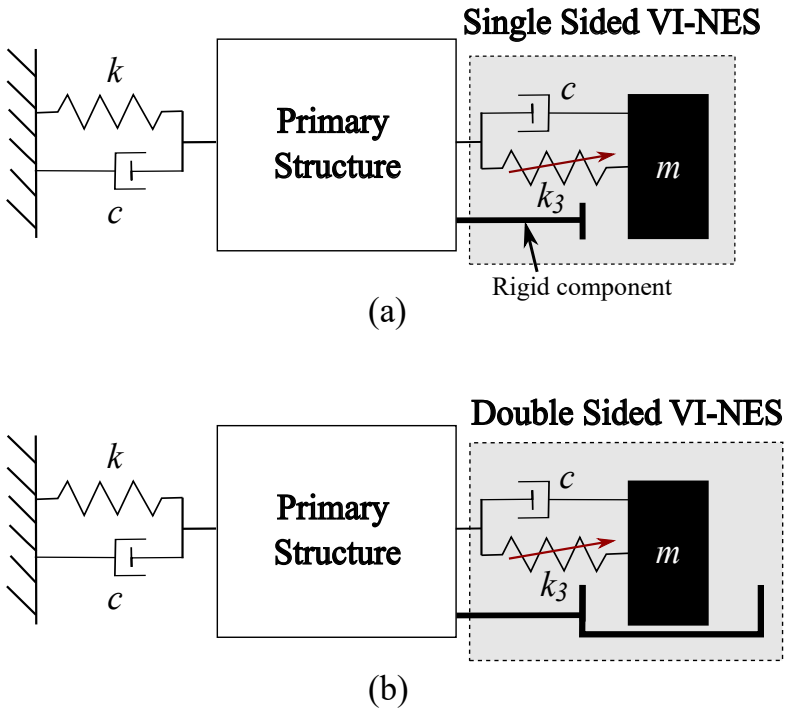

Figure 2.13 (a) Single-Sided VI-NES configuration, (b) Double-Sided VI-NES configuration

and double-sided VI-NESs [101]. Optimal behaviour for such a kind of NESs requires low stiffness and relatively high mass, as well it depends on the clearance between the NES mass and the primary structure wall [102]. The single-sided VI-NES (Figure 2.13 b) showed the best performance in mitigating vibration of structures over a wide range of energy levels[103]. For the mitigation of multi-floor structures, Nucera et al. [104] found that this non-smooth stiffness NES was more efficient on the ground floor. While the smooth cubic stiffness NES is favourable at the higher floor for its relatively light mass. Many studies investigated the efficiency of the single-sided VI-NES in eliminating the vibrational energy of large-scale structures [48, 105, 106]. While others focused on studying the system dynamics [107, 108] and optimizing the mechanisms of TET for VI- NESs [109]. Wang et al. [110] introduced another configuration for the VI-NES with a modified track for the impact mass. Advanced types of VI-NESs used magnetic-nonlinear forces with the impact coupling to improve the energy absorption close to what was observed by the single-sided VI-NES [111, 112].

2.3.3 Track NES

Wang et al. [23] proposed the track NES, in which the auxiliary mass moves in a smooth and symmetric racetrack without spring elements (Figure 2.14 a). The shape of the given track defines the damping and restoring force of such NESs. This study compared the effect of a

tune-in TMD, a typical cubic stiffness NES and a track NES in reducing the vibration of a 2-DOF structure due to an impulsive or seismic load. The authors highlighted the robustness of the track NES and the flexibility of its restoring force. An optimization for the design of a fourth polynomial order track shape followed the numerical analysis. In the same year, the first experiments of the track NES [113] validated its efficiency to mitigate the vibration of 2-DOF structures. The energy transfer across high modes enabled by the track NES accelerated the dissipation rate to control the structure response over a wide band of frequencies. Moving to a larger-scale structure, Lu et al. [114] experimentally reduced the vibration response of a five-story steel structure by an optimized track NES. The track NES of a mass 10% that of the primary structure could absorb the vibration of a seismic excitation over a broad frequency range.

Later, Wang et al. [116] analytically investigated a single-sided vibro-impact track NES (Figure 2.14 b) to mitigate the response of a multi-story building. Although, the single-sided track NES requires smaller space compared with a smooth track NES. It was more effective in reducing the structure vibration due to the collision of the NES mass with the walls of the primary system. In a numerical study [24], an optimal designed single-sided track NES effectively reduced the seismic response of a 32-story structure. The short-stroke and the slight damping of such NES reduced its potential cost. Thus, the single-sided track NES is a low-cost promising device that provides alternatives for costly strategies used in controlling high building response against seismic excitations.

A two-phased track NES is a modified version of such NESs [115] with higher efficiency in mitigating the response of large-scale structures. The two-phased trackrace defined by two different radii (Figure 2.15 b) provided a low phase to accommodate the auxiliary mass at small displacement and a high phase adapting higher-amplitude dynamics. A larger track ra-

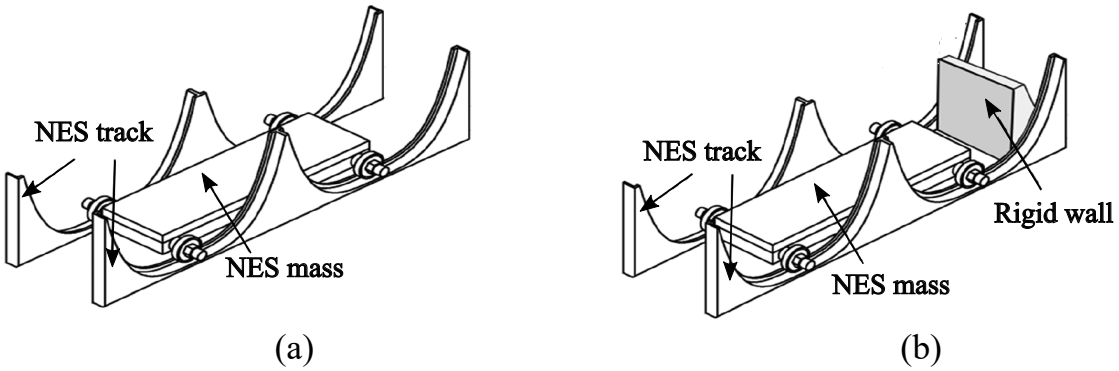

Figure 2.14 Track NES configurations [24] : (a) typical track NES, (b) singlesided vibroimpact track NES.

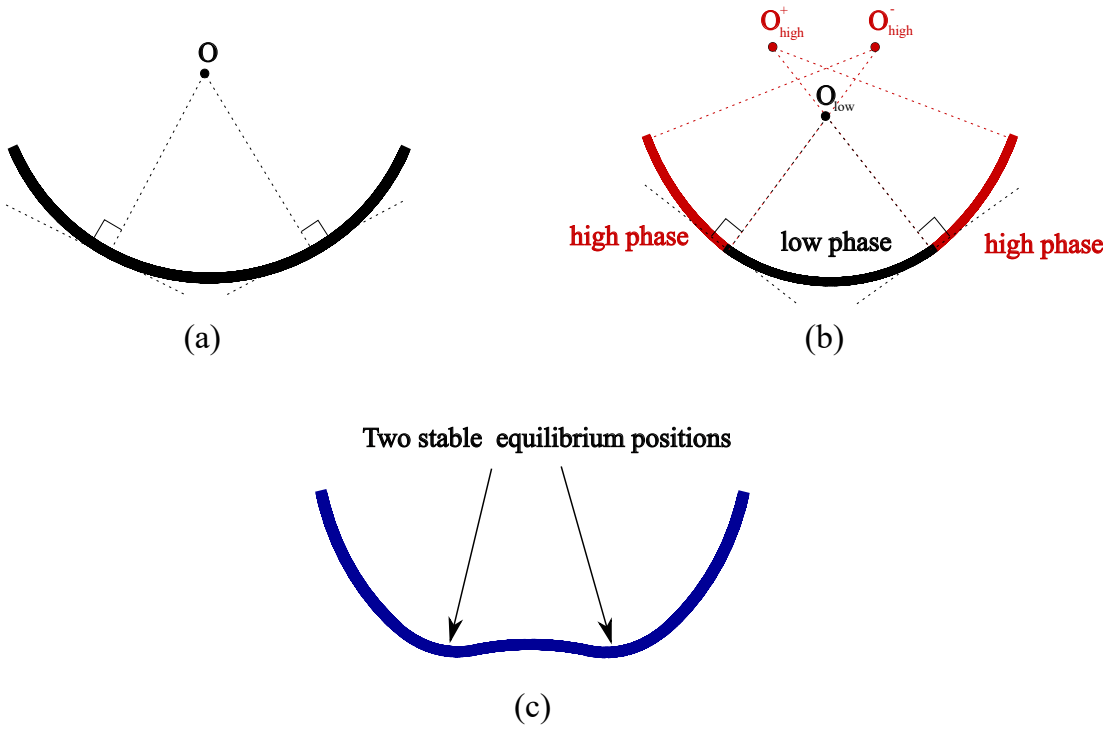

Figure 2.15 Track shapes of varoius track NES types ; (a) typical track NES, (b) two-phased track NES [115], and (c) bi-stable track NES.

dius decreases the restoring force at the edges of the track. The numerical simulations showed that a two-phased track NES of 10% mass ratio could reduce the maximum displacement of the structure base by 40%.

Wang et al. [117] referred to the restoring force decrease following the increase in the NES displacement as the peaking behaviour. That behaviour is responsible for the high frequencies experienced by the track NES and improves the energy absorption of the track NES. The deep understanding of the track NES dynamics facilitated its practical implementation for advanced vibration control strategies. Recently, an experimental and theoretical study [25] validated the extended working range and the better energy robustness of a new bi-stable track NES that combined the advantages of both the peaking behaviour of the track NES and the negative stiffness of the bi-stable NES. The track design of this integrated NES granted two stable equilibrium points, leading to a restoring force of linear and nonlinear terms. The interaction of the linear and nonlinear dynamics increased the rate of the irreversible energy transfer at higher vibration modes.

2.3.4 Rotative NES

Considering the main advantage of the NES to interact with the dynamics of a primary structure over a wide range of frequencies, Gendelman et al. [118] introduced a simple rotator with a rigid coupling to the primary structure as a new type of NES (Figure 2.16 a). The ability of the NES to rotate with variable frequencies without any spring elements simplified the device construction. However, the dynamics of the rotative NES showed more complexity. The rotative NES experienced three different regimes: oscillatory, intermittent, and rotational. The third one is the most effective regime characterized by a high rate of energy transfer and results in a strongly modulated response (SMR) for the primary structure.

An analytical study [119] demonstrated how a rotative NES engaged with the resonance of a linear oscillator at different modes by adapting its dynamics to mitigate the vibration of the primary system. The rotator experienced two different angular speeds; the slower coincides with the frequency of the primary system, and the higher speed is a multiple of it by integer number depending on the system energy. A later study [19], discussing the rotational NES effect on a cylinder in three-dimensional turbulent VIV, introduced a line mass (thin cylinder) as a rotating mass. The proposed rotative NES reduced the amplitudes of the cylinder VIV.

Instead of the rigid bar attaching the tip mass in the typical rotative NES, Saeed et al. [20] used an elastic one with a radial DOF in a rotary-oscillatory NES (Figure 2.16 b). This adaptation increased the capacity of the NES and reduced the required number of oscillations experienced by the device to absorb the same amount of energy. Hence, the rotary-oscillatory NES is more effective in mitigating the undesired response of structures due to rapid excitation over a high range of energy levels.

2.4 The NES as a suppressor for FIV

The NES has widely appeared as a suppressor for types of FIV in many structures. Many studies have implemented the NES to reduce the wing flutter. As well, NESs mitigate the vibrations of pipes conveying fluids. Moreover, various designs of NESs, integrated with cylindrical structures, can reduce the amplitudes of VIV and delay the galloping of prisms.

2.4.1 Wing instabilities

Lee et al. [120, 121] integrated a typical translative NES into a two-DOF wing model and demonstrated the beneficial role of the NES in delaying the wing flutter. The analytical and numerical analyses [120] exhibited three different regimes; periodic cycles of attenuation

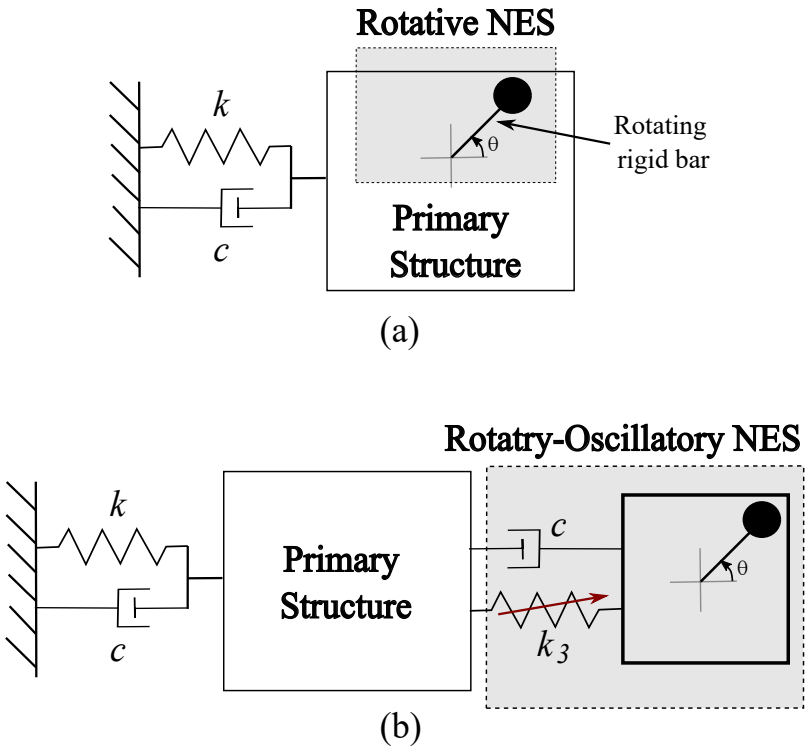

Figure 2.16 (a) Rotative NES, (b) Rotary-Oscillatory NES

and growing of oscillations, intermediate suppression, and complete absorption. A series of resonance captures affecting the system dynamics was the main reason for the observed regimes. The experimental realization of the problem [121] validated the NES capability in reducing the limit cycle oscillations (LCO) of a rigid NACA 0015 airfoil in heave and pitch. The NES engaged with the wing dynamics experiencing 1 : 1 resonance captures with the aeroelastic modes of the wing section. As a result, it increased the wing critical speed by 26% of its original value. Decreasing NES stiffness or damping and enlarging the mass provided the best suppression efficiency for the NES. This study pointed out the light NES as a low-cost and robust solution for suppressing wing instabilities. A comparable study [122] confirmed the NES suppression effect on the amplitudes of the pitch and heave of an airfoil through numerical investigations. The mass and location were leading parameters for NES design. Besides, the decaying characteristics of the NES were important in dissipating the energy absorbed from the primary system. Later, Bharath and Samy [123] optimized the NES design for maximizing its suppression effect on the pitch and heave responses of wings.

Lee et al. [124] enhanced the suppression efficiency by using multi-DOF NES. The authors presented two configurations for the multi-DOF NES, where the NES masses were linked in series or parallel. The masses-in-series configuration is superior and more robust than the

single-DOF NES of the same total mass. Nevertheless, the parallel type was not efficient in reducing the limit cycle oscillations of the wing. Hubbard et al. [125] added a rotative NES at the tip of a flexible swept wing of constant-thickness to control its response. The analytical analysis of the given system and the experiments provided a minimum amount of energy beyond which the NES can engage in a $1:1$ resonance with the wing in the second bending mode, absorbing its vibration. The numerical simulations approved that the rotative NES of higher stiffness also interacted with the wing dynamics in the first torsional mode at a higher excitation energy level. Thus, the rotative NES can passively suppress the wing response in one or more aeroelastic modes depending on design considerations.

Zhang et al. [126] coupled two NESs at the leading and trailing edges of a 2-DOF wing section to delay wing instabilities to larger speeds compared to a single NES. The NESs interacted with the wing dynamics, exhibiting $1:1$ and $3:1$ resonance captures and resulting in a high rate of energy transfer at various modes of the wing. The rate of energy transfer depended on the NES location and the vibrational mode. Thus, the NES at the leading edge suppressed the heave mode, while the one at the trailing edge controlled the wing response in the pitch mode. A later study [127] found that the NES was no longer able to suppress wing response when the natural frequency of the pitch mode equals three times that of the heave mode.

Guo et al. [128] numerically studied the NES effect on an airfoil with a free-play control surface and nonlinear stiffness in pitching. The NES was able to increase the flutter speed of the wing and limited its oscillation to small values. The larger NES mass led to the higher suppression efficiency. The study recommended the aileron position as the best location for NES in the case of an airfoil with a control surface. Hubbard et al. [129] mounted a NES at the wingtip to control its transonic aeroelastic instability in wind tunnel tests. The winglet-mounted NES design stabilized the wing over a wide range of working conditions and increased its flutter speed. The experimental realization confirmed the suppression effect of the NES in the second bending mode, contrary to the torsional mode where the NES was ineffective. The computational analysis provided the insignificance of moderate friction damping effect on the NES behaviour. The NES parameters were optimized [130] to increase the dynamic pressure by 40% at the critical conditions compared to the wing without NES.

Panel flutter is another type of aeroelastic instability that affects aircraft skin at high speeds. In the first study presenting the NES as a passive absorber for panel flutter, Pacheco et al. [131] numerically compared the energy injected by the flow to that absorbed by the NES to assess the NES effect. The NES increased the panel stability against perturbation at speeds lower than the flutter speed. Besides the capability of the NES in delaying the flutter, it still absorbed energy at high velocities reducing the amplitudes of limit cycle oscillations. The

authors highlighted the NES stiffness and damping and the streamwise location of the NES as leading parameters for the design. The NES as well controlled the response of transonic flutter of wings [132]. The NES interaction modulated the system dynamics forming new equilibrium positions and leading to a region of elimination for the LCO. At higher speeds, the NES partially suppressed the wing response depending on the initial conditions. The optimal design of the NES required a minimum damping coefficient and optimized stiffness to maximize its efficiency. Moreover, the NES mitigated the nonlinear response of a three-dimensional hypersonic wing [38]. The NES increased the flutter speed and improved the stability of the wing at pre-flutter speeds. Beyond flutter speed, the NES engaged with the system dynamics in a $1:1$ resonance capture. Thus, it eliminated the nonlinear oscillations but did not last for higher dynamic pressures. Besides the great effect of the NES mass and location on its suppression efficiency, these parameters controlled the aeroelastic shapes of the wing. Recently, Fernandez-Escudero et al. delayed the wing flutter occurrence by implementing a NES as a wings flap [39]. The advantage of stiffness nonlinearities in controlling the wing response was validated experimentally and numerically.

2.4.2 Vibration of fluid-conveying pipes

NESs can suppress the excessive vibration of pipes conveying fluid over a wide range of velocities compared to traditional passive methods. Yang et al. [133] numerically examined the energy transfer across apipe conveying fluid coupled with a typical NES and approved the capability of the NES in absorbing the induced vibration. Mamaghani et al. [134] illustrated the NES effect on suppressing the response of a conveying-fluid pipe under periodic excitation. The NES absorbed the vibration due to the external harmonic load leading to a strongly modulated response for the pipe. The optimization of the damping and location of the NES with the predicted force magnitude and flow velocities could lead to the maximum benefit of the NES. The authors recommended the midspan of a fixed-fixed pipe as the best location for a coupled NES. The study compared the responses of the pipe with an optimized linear absorber and with the NES, highlighting the NES's beneficial role in suppressing the vibration without changing the system characteristics.

Zhao et al. [135] considered the nonlinearity of the pipe response in a similar problem. The study confirmed the NES suppression efficiency related to the TET phenomena. NES stiffness variation resulted in complexity in the system's nonlinear response. A NES also was able to control the flutter instabilities of a cantilevered pipe conveying fluid. Zhou et al. [136] used a NES to increase the flutter critical speed and reduce the amplitude of its oscillations. A parametric study showed that the increase in the NES mass and damping delayed the

occurrence of flutter. NES parameters controlled the system response, while the best location of the NES was affected by the flutter mode shape.

Khazaee et al. [40] implemented more than one NES in series and parallel configurations to suppress the response of a transporting-fluid pipe. The suppression region of the multi NESs exceeded that of a single NES, which enhanced the energy transfer mechanism. An optimization considering the uncertainties effect provided a critical number for NESs, above which the NES suppression efficiency decreased. The bi-stable NES as well interacted with the pipe dynamics and was able to suppress its vibration. Yang et al. [137] promoted the bi-stable NES over the typical one as it was faster in absorbing energy and had a higher robustness and suppression efficiency. The optimal design of the bi-stable NES was able to dissipate 98.2% of the system energy.

2.4.3 VIV and galloping instabilities of cylindrical structures

In the last decade, the NES has appeared as a solution for suppressing flow-induced vibration (FIV) of cylindrical structures. Many studies investigated the effect of the translative NES on the VIV of a cylinder. Tumkur et al. [41] used a two-DOF reduced-order model for VIV to investigate the dynamics of a cylinder coupled with a translative NES. The NES 1:1 resonance capture phenomena resulted in the energy transfer across the system, reducing the amplitudes of VIV. Mehmood et al. [42] employed a similar approach showing the dependence of the suppression efficiency on the initial conditions. The numerical simulations provided a critical mass ratio and a value for the NES damping below which the NES was ineffective in suppressing the cylinder response. Chen et al. [138] simulated the response of a two-DOF elastically supported cylinder with an NES. The NES effectiveness in reducing VIV amplitudes was improved by increasing its mass and stiffness. The change only in the NES mass shifted the lock-in region. The authors succeeded in suppressing the wake-induced vibration of two identical cylinders by the same technique. Dai et al. [43] employed the wake-oscillator models for evaluating the fluid forces due to VIV and confirmed the NES's capability in suppressing VIV. The authors explained the various dynamics of the NES, pointing out the effect of the multiple stable responses in enhancing the energy transfer and reducing vibration amplitudes. A recent study [139] addressing a similar problem at low Reynolds number revealed a chaotic response for the cylinder coupled by NES. The numerical simulations provided a range of mass ratios for the NES, out of which the NES would be ineffective in suppressing the cylinder vibration.

Analytical and numerical studies have investigated the suppression efficiency of the rotative NES on VIV of cylindrical structures. Blanchard et al. [140] employed the multi scales me-

thod and complexification-averaging to study the dynamics of a two-dimensional cylinder coupled with a rotative NES. The authors used a reduced-order model for the fluid loads and highlighted strongly modulated responses of the cylinder due to TET from the cylinder to the rotator. The numerical simulations provided that the lighter NES requires a larger radius and higher damping to sustain a convenient suppression efficiency. Moreover, the NES indirectly affected the flow surrounding the cylinder [141], and a proper NES mass could elongate the wake increasing the cylinder stability. Tumkur et al. [142] pointed to the complex responses arising due to the dynamic interaction between a vibrating cylinder and a rotative NES. Besides the effect of such NESs on the wake vorticity, it led to chaotic responses at low Reynolds number. Ueno and Franzini [45] studied the effect of NES parameters by presenting the oscillation amplitude of the cylinder as functions of the mass, the radius and the damping of the NES for the lock-in range of reduced velocities. A developed rotative NES composed of a line mass mitigated the vibration of a cylinder in a turbulent three-dimensional flow [44]. The energy absorption capability of the NES mitigated the cylinder oscillations and reduced the drag load by 50%. Locking up the rotating mass directly permitted the VIV to start [143]. The indirect effect of the NES on the surrounding flow raised an interesting problem concerning the fluid-structure interaction. Chen et al. [144] found that the NES was more functional in mitigating the VIV of high mass ratio cylinders than lower ones. The study confirmed that increasing the NES mass and radius enhanced the NES suppression effect and mentioned the dependence of the optimal NES damping on the mass ratio of the structure. Recently, Franzini [145] replaced the rigid bar attaching the rotating mass with an elastic one with a radial DOF. The elastic rotative NES reduced the amplitude of the VIV by 25%, which is better than the suppression effect of an identical NES with a fixed radius.

We can only find a few contributions regarding passive suppression of galloping by NES. Dai et al. [46] analytically investigated the response of a square prism fitted with a translative NES. This study pointed out the influence of the NES parameters on the onset speed of galloping and the strongly modulated responses of the prism. Teixeira [47] addressed a similar problem with considering a rotative NES. Throughout the numerical simulations, the NES could reduce the vibration amplitudes of the prism to half its original values.

2.5 Automatic Ball Balancer (ABB)

While the rotative NES uses a rotating rigid bar with a tip mass, an automatic Ball Balancer (ABB) consists of free metal balls. These balls rotate in a circular track due to dynamic interaction with a vibrating rotor [50, 146]. I experimentally validated the great effect of the device on reducing unbalanced rotor vibration [147] during my master research. The auto-

matic balancing phenomenon works properly at speeds beyond the angular natural frequency of the rotor, where the ball tends to move away from the imbalance, as the rotor geometric centre and the imbalance mass are located on opposite sides, relative to the mass centre. At low speeds below the rotor natural frequency, the ABB can not balance the system when the rotor geometric centre and the imbalance mass are in phase. The ball friction with the balancer track is considered as a critical parameter affecting the balancer behaviour [148]. An increase in friction widens the stable range of the balancer with an undesired effect on the transient responses. In addition to the conventional ball balancer presented in Figure 2.17, we can find other configurations. Adding a nonlinear suspension to the conventional ball balancer improved its effectiveness in damping the rotor vibration [149]. In another study [150], the balancing mass can move radially along a rigid bar beside the tangential motion to enhance the transient response. Although rotor dynamics are different from the galloping mechanism presented in the current research, we value the simplicity of the ball balancer that helps in its implementation in practical applications.

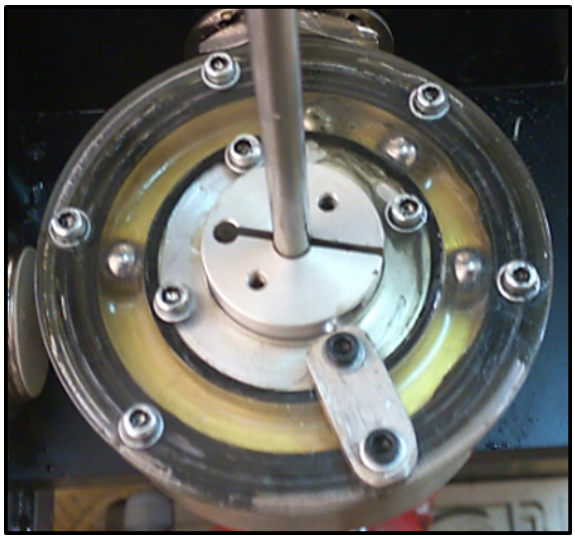

Figure 2.17 Automatic Ball Balancer

CHAPTER 3 PROBLEM STATEMENT

NESs possess consierable advantage in comparison to other vibration absorbers: the absence of a linear natural frequency, and their ability to interact with the dynamics of a primary system over a broad range of frequencies. The experimental work on NESs is limited comparing to the theoretical work found in the literature and mostly deals with the NES as a passive suppressor for buildings vibration. A few contributions are concerned with the passive suppression of wing aeroelastic instabilities by a NES. In terms of cylindrical structure instabilities, experiments only validated the VIV model of the cylinder without examining the NES capability in modulating its responses. Most of the proposed experimental NESs are complicated and difficult to be practically implemented in industrial applications. The ball-track configuration of an ABB is inspiring for developing a purely rotative NES, applicable for practical implementation.

In the current research, we introduce a ball-in-track configuration as a purely rotative NES. The design simplicity and the low-cost production of the proposed NES facilitate its practical implementation with a square prism model in wind tunnel tests. Moreover, we improve the suppression efficiency of the proposed NES by using multiple balls instead of a large one of equivalent mass. The collisions between balls enhances the energy transfer across the coupled system of the prism and the ball-in-track (BIT) NES.

3.1 Research objectives

3.1.1 Main objective

The main objective of our research is to develop a simple and robust nonlinear energy sink (NES), based on the ball-in-track configuration, capable of mitigating the galloping of a square prism.

3.1.2 Specific objectives

For achieving the main objective and enhancing the ability of the rotative vibration absorber, we pass through three specific objectives.

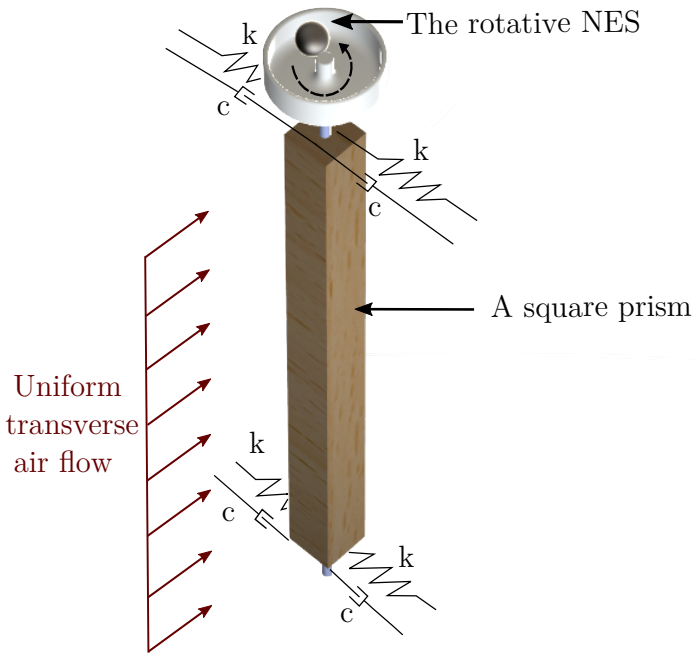

Figure 3.1 The designed model the square prism with a purely rotative NES

Demonstrate and characterize the proposed NES experimentally

Design, and fabricate a ball-in-track rotative NES to be easily mounted on a square prism model, as depicted in Figure 3.1. Test the rotative NES experimentally by comparing the galloping amplitudes of a prism with and without the NES. Explain the different NES dynamics and their effect on the prism response. Define the main NES parameters and demonstrate their influence on NES behaviour.

Simulate and explain the dynamics of the prism-NES system at high flow speeds beyond the limit of experiments

Derive a mathematical model for the prism-NES system. Measure the normal force coefficient affecting the square prism as a function of angle of attack and introduce it as an input for the numerical model (see Fig. 3.2). Obtain an accurate expression for the ball damping coefficient through free rotation tests. Validate the model with the experiments of objective 1. Then use the model to explore the system dynamics at high flow speeds out of the experiment's limitation. Resolve the power flow analytically across the prism-NES integrated system to explain the NES dynamics and predict its maximum power capacity.

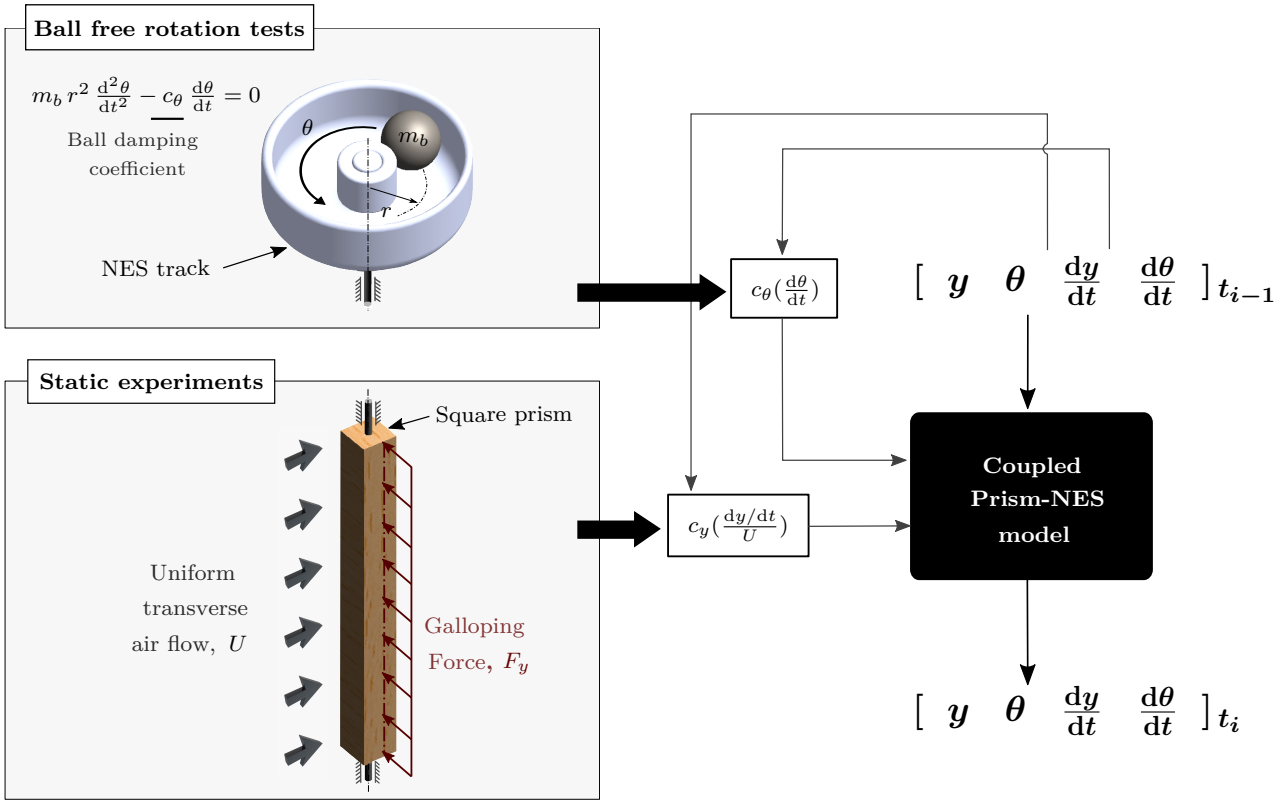

Figure 3.2 The proposed model for simulating the dynamics of prism-NES integrated system.

Improve the suppression efficiency of the NES by using multiple balls

Test different multi-ball NESs highlighting the effect of ball number on the suppression efficiency of the NES in mitigating the galloping of a square prism model (see Fig. 3.3). Identify the main parameters affecting the behaviour of a multi-ball NES. Explain the effect of ball collisions on the NES behaviour. Illustrate how increasing the ball's number affects the NES track crowdedness and shifts the NES mass centre.

3.2 Description of research progression

This research focus on applying a ball-in-track NES to mitigate the galloping of a square prism. We introduces the research contributions in three journal articles:

- **Article 1**: Wind Tunnel Demonstration of Galloping Mitigation with a Purely Nonlinear Energy Sink.

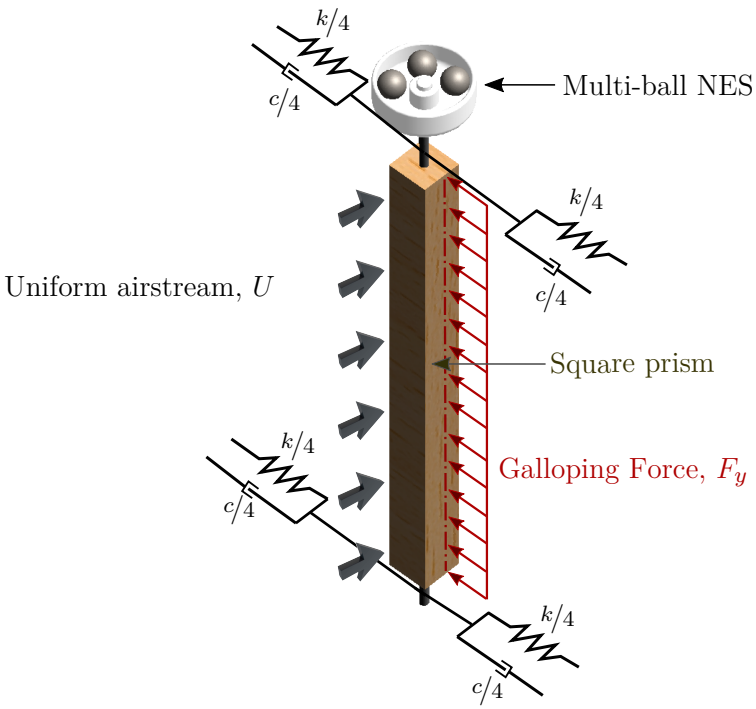

Figure 3.3 Multi-ball NES coupled with a square prism model.

- **Article 2**: How a Ball Free to Orbit in a Circular Track Mitigates the Galloping of a Square Prism.
- **Article 3**: Multiple Balls Rotating in a Circular Track Experimentally Mitigate the Galloping of a Square Prism.

Each article presents a specific objective. Article 1 addresses the first specific objective, experimentally validating the effect of the ball-in-track NES on mitigating the galloping of a square prism model. Wind tunnel tests illustrate the different NES response modes : oscillatory, intermittent and rotational, and show their impact on the prism response. A parametric study is followed to demonstrate the influence of the main NES parameters on its behaviours. Article 2 advances the second specific objective of our research providing numerical simulations and analytical for the dynamics of the prism-NES integrated system. A model employing the fitting of experimental data for the ball damping coefficient C_θ and the square prism normal force coefficient C_y as inputs is developed for the realistic simulation of the system dynamics. The simulations illustrate the different NES dynamics observed in the experiments and predict an ineffective regime at high flow speeds that we cannot test due to the limit of the experimental setup. A proposed power flow analysis clarifies the energy

transfer mechanism across the coupled system, which gives more insight into how the ball-in-track NES works. The numerical and analytical work done in Article 2 complies with the experimental results of Article 1, explaining the behaviour of the NES and predicting its effective range.

After approving the idea of the ball-in-track NES experimentally in Article 1 and explaining its working theory in Article 2, Article 3 covers the third specific objective of the current research by presenting how the suppression efficiency of the proposed NES increases by using multiple balls instead of one. Ball collision is an additional mechanism for energy absorption in the multi-ball NES. Besides, the interaction between multiple balls in the same track prevents the continuous rotational response and leads to different dynamics compared to the single ball NES. We explain the concept of the multi-ball NES and theoretically express the main parameters affecting its behaviour. Additionally, Wind tunnel testing of NES different configurations illustrates the ball number effect on the behaviour of the multi-ball NES.

CHAPTER 4 ARTICLE 1: WIND TUNNEL DEMONSTRATION OF GALLOPING MITIGATION WITH A PURELY NONLINEAR ENERGY SINK

Michael M.Selwanis, Guilherme R.Franzini, Cédric Béguin, and Frédérick P.Gosselin

This chapter represents the first article, published at "Journal of fluids and structures" in January 2021. DOI : http://dx.doi.org/10.1016/j.jfluidstructs.2020.103169.

Abstract

Galloping is a critical type of flow-induced vibration (FIV) arising on power transmission lines, high rise buildings, pipe and cables bundles in the oil and gas industry. In this paper, we present a purely nonlinear energy sink (NES) that mitigates the galloping of a square prism. The NES is composed of a ball rotating freely in a circular track attached to the prism. The ball's dynamics is coupled to that of the prism in a purely nonlinear way by inertia. We experimentally assess how this simple NES reduces the prism vibration by comparing the prism amplitude responses with and without the NES. A supplementary video presents these experiments, during which the NES ball exhibits different dynamics in three regimes ; oscillatory, intermittent, and rotational. We characterize the ball behaviour and its effect on the prism response in each regime. The oscillatory regime appears at low flow speeds at which both the prism and the ball oscillate with small amplitude. The intermittent regime represents a transition mode within a small range of flow speeds and corresponds to a small jump in the vibration amplitude of the prism. The rotational regime appears at higher flow speeds, where the ball oscillates with relatively high angular speeds resulting in a strong modulated response of the prism. The design of the NES allows to easily vary its track dimensions to use a ball of different sizes and masses. Accordingly, we demonstrate the influence of the main NES parameters, which are the ball mass, NES track radius, ball friction, and radial clearance between NES track walls and the rotating ball, on both the prism response and the ball behaviour. The NES we present is directly amenable to mitigate other types of FIV.

Keywords : Non-linear energy sink, Vibration suppression, Square prism, Galloping, Energy transfer, Wind tunnel tests.

4.1 Introduction

Transverse galloping is a critical type of flow-induced vibration (FIV) that commonly occurs at high flow speeds. During heavy wind, galloping may have destructive effects on many structures such as skyscrapers, transmission lines, and road signs. A linear Tuned Mass Damper (TMD) is a simple device used for damping vibration of structures. This mass-spring-damper system [151] is tuned to change the natural frequency of the system. A TMD works efficiently in a narrow frequency band but adds new potential resonances to the main structure. Contrary to the TMD, another particular class of suppressors known as nonlinear energy sinks (NES) have no linear natural frequency [13] and can engage with the primary vibrating systems over a broad range of frequencies reducing its vibration amplitude.

A NES is a passive vibration suppressor that consists of a mass added to a primary structure and characterized by a non-linearizable stiffness and usually linear damping properties [13]. A NES without direct attachment to the primary structure [98, 99] is a special type of such devices with zero-stiffness, their dynamics is purely nonlinear. A NES works by Targeted Energy Transfer (TET) [73, 152] : during vibration, a portion of the energy is transferred irreversibly from the primary structure to the NES reducing vibration amplitudes.

The great interest in the field of nonlinear energy absorption has led to various NES designs. In a vibro-impact NES, the impacts of balls with rigid walls dissipate energy [22]. In a translative NES, a small mass attached to the main structure by an essentially non-linear spring and a dashpot absorbs vibration during its translational motion [49, 153]. While in a rotative NES [20], a rotating rigid bar with a tip-mass attached to the main structure represents another technique for vibration suppression. The rotative NES is a simple and promising device that can damp vibration without a spring element [45].

Only a few contributions are concerned with the passive suppression of galloping by a NES. Dai et al. [46] analytically and numerically studied the response of a square prism fitted with a translative NES. This study pointed out the influence of the NES parameters on the onset of the critical galloping velocity, as well as the strongly modulated responses of the prism. Teixeira et al. [47] addressed a similar problem with considering a rotative NES. Throughout the numerical simulations, the NES can reduce the vibration amplitudes of the prism to half its original values.

However, in the last decade, researchers have used various NES designs to suppress a particular type of FIV different from galopping, e.g., vortex-induced vibrations (VIV). Tumkur et al. [41] investigated the dynamics of a cylinder fitted with a translative NES using Computational Fluids Dynamics (CFD) and reported a 75 % reduction in the cylinder vibration

amplitudes due to vortex shedding. A similar approach was employed by Mehmood et al. [42], who pointed out the dependence of the suppression efficiency with the initial conditions. Blanchard et al. [44] focused on VIV suppression using a rotative NES. The authors used CFD approaches for computing the fluid loads and highlighted the significant energy transfer that appears in the strongly modulated responses of the cylinder. Conversely, Dai et al. [43] employed the wake-oscillator models for evaluating the fluid forces due to VIV and showed that a translative NES can similarly modulate the cylinder responses. s. Ueno and Franzini [45] studied the effect of the NES parameters on the oscillation amplitude of the cylinder.

Experimental investigations related to NESs are fewer than theoretical ones and mostly deal with the NES as a passive suppressor for building vibration. Wierschem et al. [18] tested a 2-DOF NES to damp impulsive excitation showing a good effect for TET on improving the structural damping. In a similar study [154], a vibro-impact NES highly enhanced the damping properties of a structure. Wang et al. [110] examined a different vibro-impact NES showing its effect on mitigating impulsive and seismic excitation. Wierschem et al. [48] used a system of NESs to reduce the structural vibrations generated from transient loads due to blast testing of a large scale steel structure.

In terms of mitigating FIV with a NES, few experiments are available in the literature. Dongyang et al. [49], Dai et al. [43] performed experiments only to validate the VIV model of the cylinder. Despite a number of theoretical studies concerning various NES designs, few experimental demonstrations are available and even fewer industrial applications are reported. This is possibly due to the practical difficulties of implementing complex NES designs with cams, springs and other moving structures.

The automatic ball balancer (ABB) [147] is a different type of passive devices used for the reduction of rotor vibration generated from system imbalance. An ABB consists of metal balls rotating freely in a circular track due to dynamic interaction with rotor vibration [50]. The balls are required to reach a certain position to counteract the system imbalance then stop relative to the rotor. The simplicity of such balancers has extended their use to some applications such as optical disc drives [155] and washing machines [156]. However, the concept of ABB is different from a rotative NES that depends on energy dissipation to damp the vibrating structure. Whereas ABBs are fabricated with minimal friction to allow the balls to counter the rotary imbalance, a rotative NES requires dissipative forces for damping. Nevertheless, the simplicity and robustness of the ABB is highly inspiring for the design of a rotative NES.

This paper experimentally demonstrates the mitigation of the galloping of a square prism due to the dynamic interaction with a purely NES. As schematized in Figure 4.1, we use a ball free

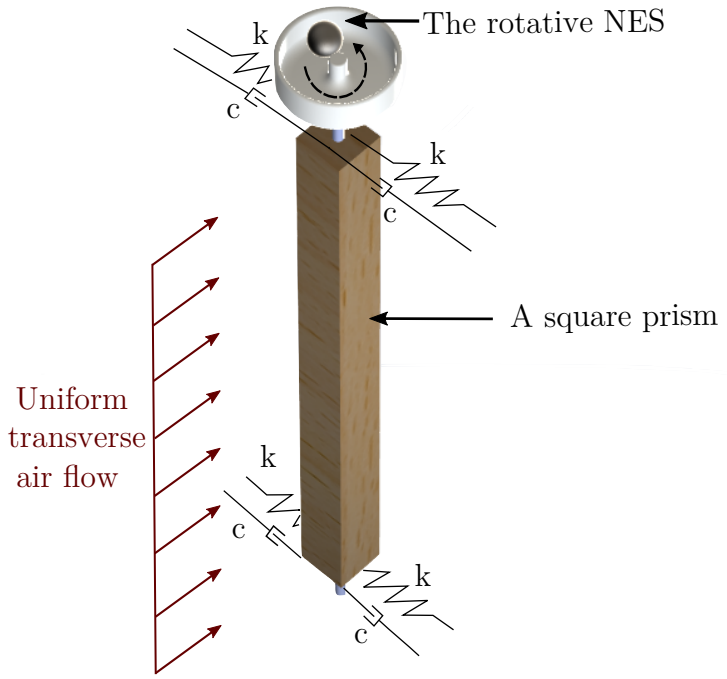

Figure 4.1 Three-dimensional drawing of the square prism model with the proposed NES

to roll in a circular track as a simple NES without direct attachment to the primary system. The paper is structured in four sections. Following this introduction, section 4.2 presents the experimental arrangement and the model description. Section 4.3 presents the results in three parts : the influence of the proposed NES on reducing the galloping amplitude, the different dynamical regimes, and the effect of the main NES parameters on its behaviour and the prism galloping response. Finally, section 4.4 brings the conclusion. In the supplementary information, we provide a video succinctly presenting the experimental setup and highlighting the article's main conclusion.

4.2 Methodology

We performed the experiments in the closed-loop wind tunnel (Model 407-B, ELD, Lake City, MN, USA) of the mechanical engineering department of Polytechnique Montréal. The wind tunnel test section is $60 \times 60\,\mathrm{cm}^2$ and the maximum air speed produced is $90\,\mathrm{m/s}$.

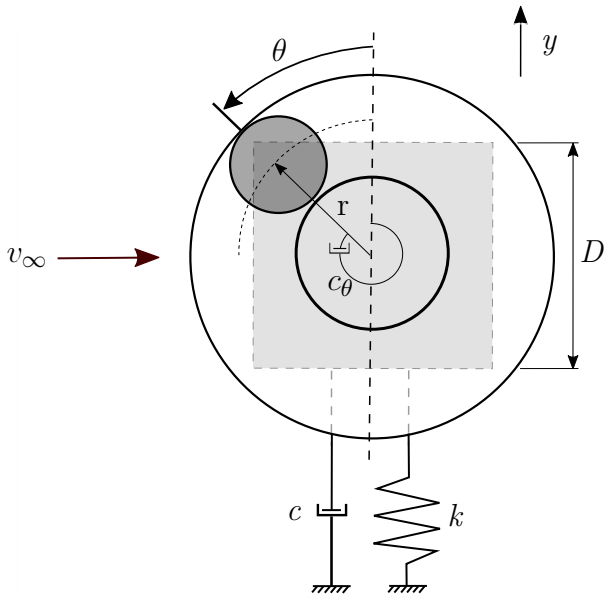

Figure 4.2 Schematic drawing of the vibrating prism with the rotative NES

4.2.1 Model description

The schematic drawing of our model (Figure 4.2) shows a square prism of side length D mounted on two identical supports of equivalent stiffness k, and a damping coefficient c. The prism can only vibrate transversely, with displacement y, to a free stream of velocity U, resulting in automatic rotation of the NES ball in a circular track of mean radius r. The ball angular displacement θ is positive counter-clockwise. A ball damping coefficient c_θ affects the ball rotation due to friction and air resistance. The ball moves on a horizontal plane. Hence, its motion is not affected by the gravitational acceleration.

We designed a lightweight prism spanning almost the entire height of the wind tunnel test section without too much blockage effect. Figure 4.3(a) presents the square prism model of 5 cm side length and 58 cm height made of balsa wood and covered with a vinyl smooth. The prism blocks 8.1% of the test section area. Two end plates (2) made of light Formica with 33 cm length, 13 cm width, and 0.1 cm thickness installed at the two ends of the square prism prevent air from escaping the wind tunnel test section.Another pair of smaller plates (3) of 15 cm length and 14 cm width are installed 8 cm away from each end. These inner plates help approach two-dimensional flow conditions ; see ref. [56]. The square prism is mounted onto two identical elastic supports allowing cross-wise oscillations. Each support consists of two leaf springs (4) as shown in Figure 4.3(b). The length of the leaf springs is long compared to the maximum allowed vibration amplitude. Therefore, the square prism is assumed to

behave as a single degree of freedom (DOF) system vibrating transversely to the flow.

Free vibration tests allowed evaluating the equivalent total oscillating mass $M = 1.39\,\text{kg}$, the natural frequency $f_n = \omega/2\pi = 2.56 \pm 0.01\,\text{Hz}$ and structural damping ratio $\zeta_y = \delta/2\pi = 0.01$, see Table 4.1. In our experiments, the prism transverse vibration is restricted by the slot length of 15 cm in the top and bottom boards of the wind tunnel test section, which allows a maximum amplitude A of 7.5 cm (equal to 1.5 times the square prism side length). We only tested one mass ratio for the prism and cannot infer about other mass ratios that can be a question of future work, notably modelling work.

This paper provides parametric study on the effect of main NES parameters in the non-dimensional form for easier generalization. Consequently, we define the following dimensionless parameters : the non-dimensional vibration displacement $\hat{Y}$ and amplitude $\hat{A}$; the reduced velocity U_r ; the NES mass ratio $\hat{m}$ and radius ratio $\hat{r}$; and the relative radial clearance $\hat{\mu}$ that relates the radial clearance μ between the NES track walls and the ball to the ball radius r_b :

$$\hat{Y} = \frac{y}{D}, \quad \hat{A} = \frac{A}{D}, \quad U_r = \frac{U}{\omega D}, \quad \hat{m} = \frac{m_b}{(M + m_b)}, \quad \hat{r} = \frac{r}{D}, \quad \hat{\mu} = \frac{\mu}{r_b}. \tag{4.1}$$

4.2.2 NES design and fabrication

We propose a simple NES design (Figure 4.4) consisting of the main body (1), various size bushings (2), steel balls (3), and a lubricating fluid (4). We built the NES to be about the size of the prism dimension and made it as light as possible. A 3D printer (Ultimaker3, Ultimaker) printed the NES components with white Poly-Lactic Acid (PLA) plastic. This modular design aims to easily vary the main NES parameters by swapping some parts. Bushings of various

Table 4.1 Physical parameters of the experiment

Cross-section side length, D	5 cm
Prism length, L	58 cm
Equivalent stiffness, k	360 N/m
Total oscillating mass, M	1.39 kg
Natural frequency, f_n	2.56 Hz
Structural damping ratio, ζ_y	0.01
Critical flow speed, U_c	6.5 m/s
The lock-in flow speed, $U_{lock-in} = f_{vs}D/S_t$	0.96 m/s
Onset velocity ratio, $\Lambda = U_c/U_{lock-in}$	6.8
Reduced flow velocity, $U_r = U/\omega D$	2.6 - 28.5

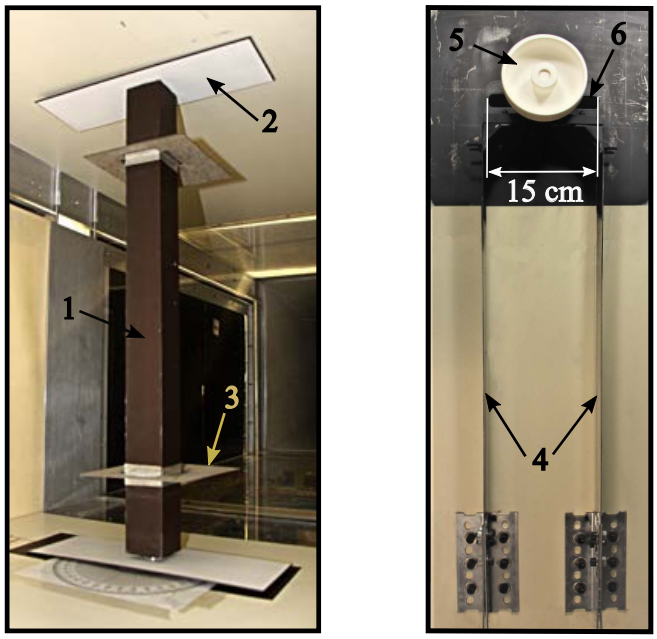

Figure 4.3 Experimental set-up showing (a) the model inside the wind tunnel test section and (b) the test section top view. The main components are numbered : (1) the manufactured square prism, (2) outer plates, (3) inner plates, (4) the support that mainly consists of two leaf springs, (5) the NES main body attached to the upper end of the square prism, (6) a slot of 15 cm length

sizes allow varying the racetrack inner and outer radii. Lubrication of the NES track decreases the friction between the rotating ball and the NES body, thus changes the ball damping.

4.2.3 Measuring system

A high-speed Camera (Motion BLITZ Cube 4, MIKROTRON) captured the motion of both the prism and the NES ball with a resolution of 0.085 mm to allow for post-treatment image analysis. The memory of the high-speed camera and the frame dimensions limit the recording time to 40 seconds. A MATLAB code was written to process the recorded image series and plot the prism vibrating displacement y and the ball angular displacement θ with time t. To ensure a steady-state, three minutes elapsed each time between setting the new wind tunnel flow speed and starting the camera recording. We repeated the measurement for incrementing flow speed with increasing values to plot the prism maximum amplitude A (max abs y(t)) *versus* flow speed U demonstrating the system response.

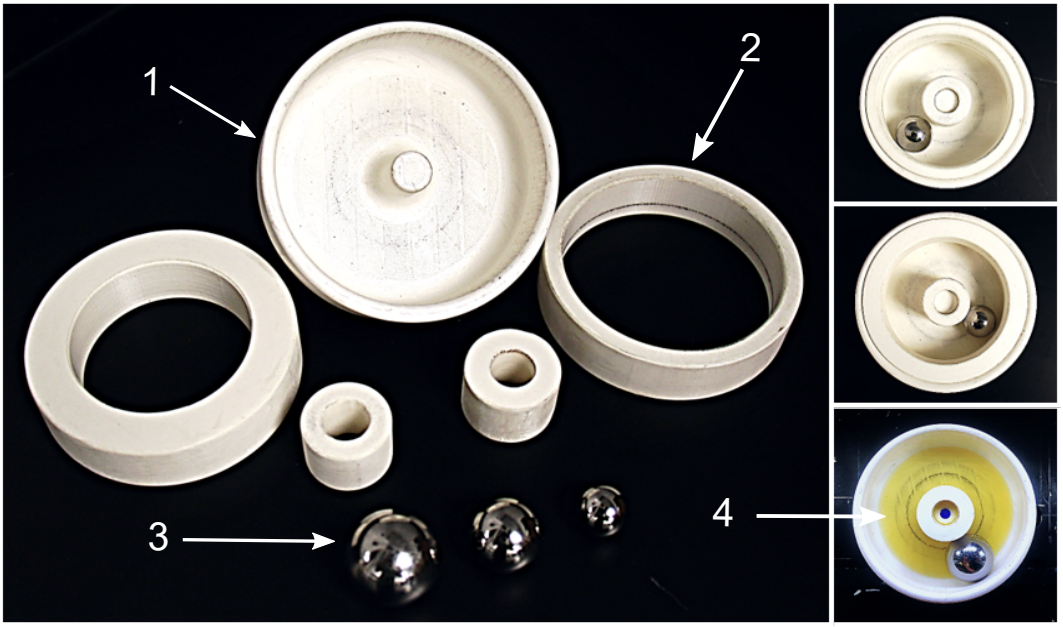

Figure 4.4 Exploded view for NES parts : (1) NES main body, (2) various size bushings, (3) metal balls, and (4) a lubricating fluid.

4.3 Results

We present the results of this study in three parts : the NES effect on mitigating the galloping of the square prism; the different dynamical regimes experienced by the NES; and a parametric study on the NES parameters. Original data of the current study, including all measurements and the image-processing code, are available at Mendeley data `http://dx.doi.org/10.17632/7kzcgvsx2x.2`.

4.3.1 NES Effect on the Prism Response

We recorded the dynamics of the prism without NES for incrementing flow speed. To clarify the nature of the vibrations, we compare the critical velocity measured for galloping versus the expected lock-in velocity for VIV. We define a critical flow speed U_c at which the prism starts to gallop exceeding 4 mm amplitude. This speed is observed experimentally as 6.5 m/s. Considering a Strouhal number S_t of 0.133 for a square prism [56], the lock-in flow speed of our model $U_{lock-in} = {}^{f_{vs}D}/_{S_t} = 0.96\,\mathrm{m/s}$. Hence, the onset velocity ratio, $\Lambda = {}^{U_c}/_{U_{lock-in}} = 6.8$ (table 4.1), and the square prism response without the NES shows a pure galloping with minimal interaction with vortex shedding. We repeated the measurement with a NES of mass ratio $\hat{m} = 0.08$, and a radius ratio $\hat{r} = 0.6$. In this subsection, the measured data is

presented in dimensional form without any post-treatment.

Figure 4.5 compares the maximum vibration amplitudes of the prism with and without the NES at different flow speeds. Beyond the critical speed U_c, the prism galloping amplitude dramatically increases with the flow speed to exceed the limit of our experiment 75 mm at a flow speed of 12.7 m/s. The prism response with the NES, presented in Figure 4.5 by the dashed line, shows a significant decrease in vibration amplitude. The NES maintains the prism vibration displacements below 5 mm up to a flow speed of 11.2 m/s. With increasing flow speed, a little jump in the vibration amplitude occurs at a flow speed of 12.7 m/s. Then, the amplitude of the prism with the NES plateaus until a flow speed of 20.2 m/s. In this flow speed range, the vibration amplitude does not exceed 30 mm. Above this flow speed, the NES is ineffective and unable to keep the prism vibration below the maximum allowed amplitude. The NES increases the flow speed at which the prim galloping amplitude reaches the limit of our experiment from 12.7 to 21.7 m/s.

Figures 4.6(a-c) present the amplitude spectra obtained from the Fast Fourier Transform (FFT) of the vibrating prism displacement in semi-log scale at different flow speeds 9.7, 11.2 and 12.7 m/s. Figures 4.5(a) and (b) compare the frequency response of the prism with and without the NES. The NES has no significant effect on the natural frequency of the prism $f_n = 2.56$ Hz even at higher flow speed $U = 12.7$ m/s where the ball rotates achieving complete revolutions.

We can observe that the NES engages with the system dynamics resulting in the transfer of energy from the vibrating prism to the NES in the form of ball rotation kinetic energy. Hence, the NES delays galloping occurrence and significantly mitigates the prism amplitudes for flow speeds between 9.7 m/s and 20.2 m/s. This range of flow speeds can be referred to as the NES effective range. At higher flow speeds, the galloping of the prism increases and the prism energy is too high to be absorbed by the NES. One of the main advantages of the NES is that it does not change the characteristics of the primary system contrary to other vibration absorbers of linear stiffness.

4.3.2 Different NES Dynamics

We demonstrate the different NES dynamics from the time history of the NES ball angular displacement and its effect on the prism response at different flow speeds. The NES experiences three different response modes ; oscillatory, intermittent, and rotational. Figure 4.7 shows the time histories of the prism displacements and the ball angular displacements at nine flow speeds U between 9 and 20.2 m/s. For the three lower speeds, Figures 4.7 (a-c) present both the dynamics with and without NES. For Figures 4.7 (d-i), $U \geq 12.7$ m/s, the

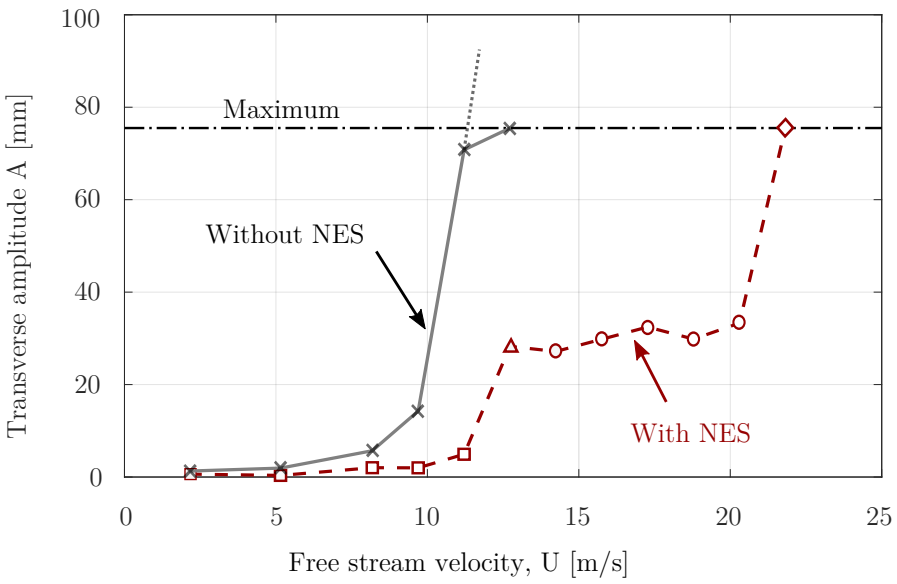

Figure 4.5 The prism responses with and without the NES of mass ratio $\hat{m}$=0.1, and a radius ratio $\hat{r}$=0.6, presenting oscillatory ▫, intermittent △, and rotational ○ regimes, and the point that reaches the maximum allowed amplitude ◇.

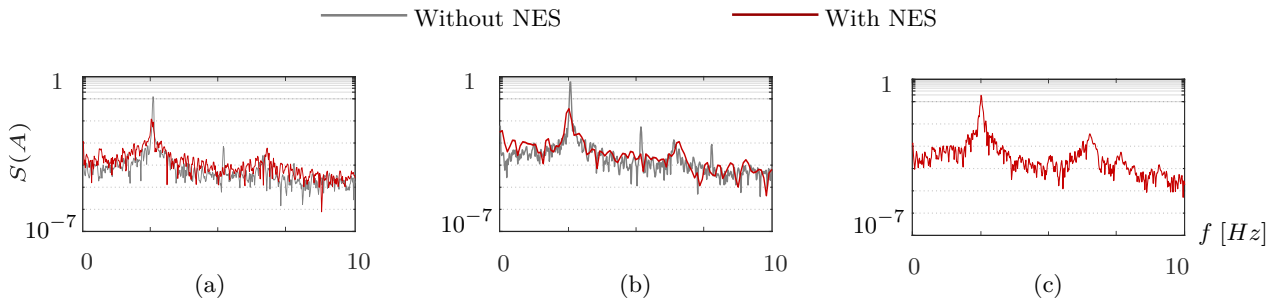

Figure 4.6 The amplitude spectrum of the vibrating prism with NES (red curve) at different flow speeds U = : (a) 9.7 m/s; (b) 11.2 m/s; (c) 12.7 m/s. The amplitude spectrum of the vibrating prism without NES (grey curve) is shown only in (a) and (b).

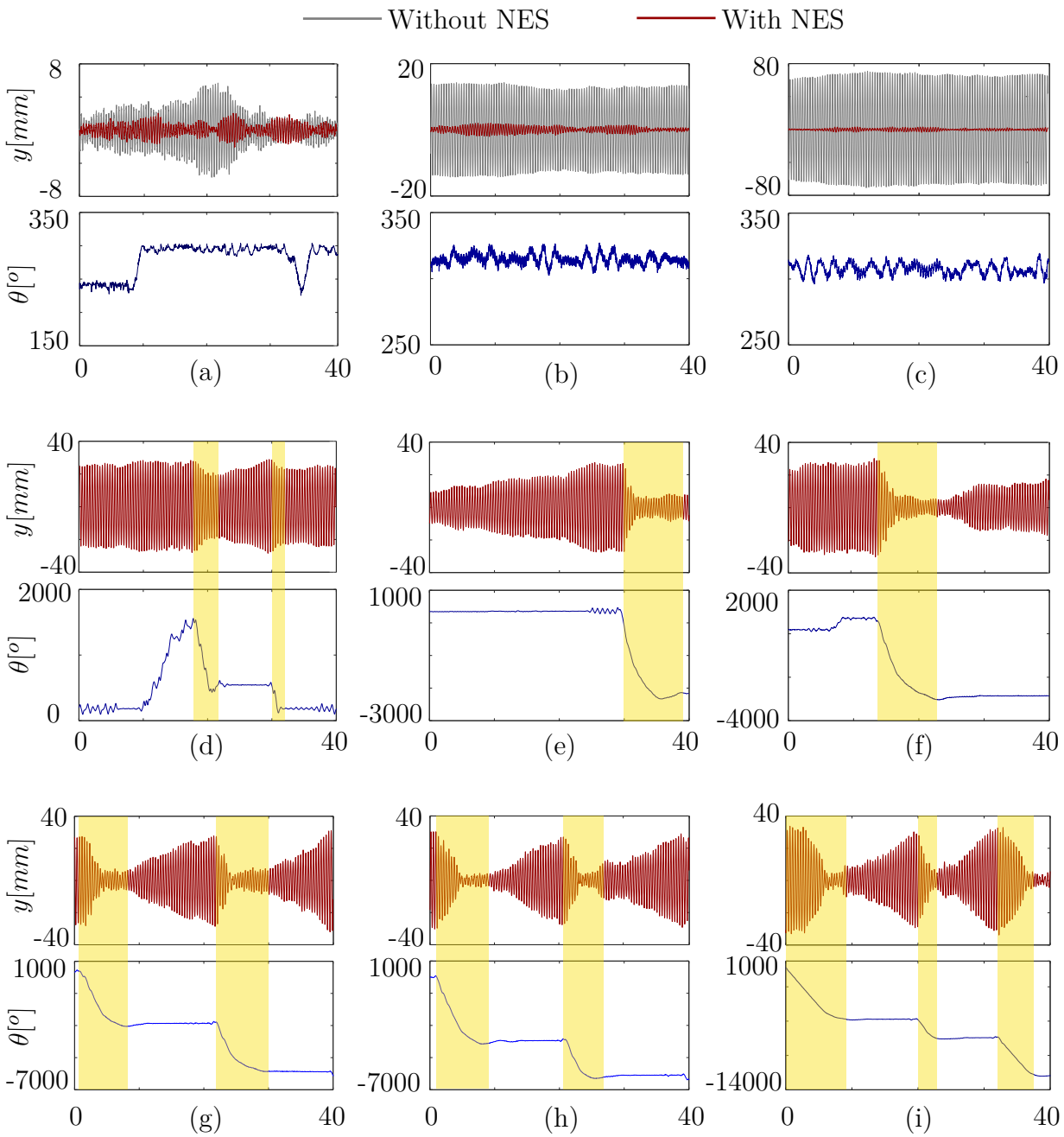

Figure 4.7 Time histories of the prism displacement $y(t)$ and NES ball angular displacement $\theta(t)$ in degrees at different flow speeds $U =$: (a) 9.0 m/s ; (b) 9.7 m/s ; (c) 11.2 m/s ; (d) 12.7 m/s ; (e) 14.2 m/s ; (f) 15.7 m/s ; (g) 17.2 m/s ; (h) 18.7 m/s ; and (i) 20.2m/s.

prism without NES reaches the maximum allowed amplitude of the setup. The behaviour of the NES and its impact on the dynamics of the prism can be broken down into three regimes, which we named according to the ball behaviour.

The *oscillatory regime* is shown in Figures 4.7 (a-c), where the NES ball angular displacement does not exceed 75^o. However, it reduces the prism galloping amplitude. Figure 4.7 c shows a significant reduction in the maximum amplitude by the NES from 70 mm to 5 mm at a flow speed $U = 11.2$ m/s.

The *intermittent regime*, shown in Figure 4.7 (d), appears as a transition between two different regimes in a small range of flow speeds. The ball rotates with relatively low angular speed keeping the prism vibration amplitude below 28 mm. This regime is characterized by a nearly steady vibration for the prism and a ball rotation of a small number of successive complete revolutions not exceeding five revolutions.

The *rotational regime* appears in a higher range of flow speeds from 14.2 to 20.2 m/s, as shown in Figures 4.7 (e-i). The prism shows a strongly modulated response of periodic cycles of attenuation and growing vibration amplitude. During each cycle, the prism vibration amplitude grows to reach a maximum value of 30 mm, then decreases sharply due to ball rotation. The vibrating prism transfers energy to the NES in the form of kinetic energy resulting in high angular speeds of the rotating ball. The ball rotation and the consequent energy dissipation through the TET mechanism drastically mitigate the prism galloping amplitude to less than 0.1 mm. From Figures 4.7 (e-i), we can also observe that the frequency of the repeated periodic cycles of the reducing and growing amplitudes increases at higher flow speed. The strongly modulated response of the vibrating prism observed experimentally in the rotational regime is similar to that previously predicted by Tumkur et al. [142], and demonstrates the energy transfer between the prism and the rotative NES during its galloping.

At large reduced velocities, beyond the rotational regime, the NES is ineffective and the galloping amplitude is above the limits of our experimental setup. We can say that the amount of energy extracted by the vibrating prism from the airflow exceeds the energy dissipation rate of the NES. Another hypothesis is that the inertial coupling between the NES and the prism is no longer beneficial at large amplitudes. Testing these hypotheses should be part of future work.

4.3.3 Influence of main NES parameters

We explore the influence of each of the main NES parameters individually. The modular NES design presented in section 4.2.2 allows easy modification of the main parameters.

Depending on the ball mass, the mass ratio $\hat{m}$ can be varied between 0.02 and 0.08. Bushings of different sizes allow varying the NES radius ratio $\hat{r}$ (from 0.4 to 0.7) and the NES track relative clearance $\hat{\mu}$ (from 0.066 to 0.33). We reduce the ball friction with the NES track by adding a lubricating fluid to investigate the effect of the friction.

We compare the prism response with various NES configurations and define NES regimes based on the difference between the non-dimensional maximum and minimum vibration amplitudes. This difference is variable across the different regimes: a large value in the rotational regime and a small one in the oscillatory regime. We developed a MATLAB code to automatically categorizes the NES regimes depending on this difference and plot a NES regime mapping for each configuration of parameters based on the following criterion:

$$\begin{aligned} \text{if} \quad & max(\hat{A}) - min(\hat{A}) > 0.2 \quad \Rightarrow \quad \text{rotational regime,} \\ \text{else if} \quad & max(\hat{A}) - min(\hat{A}) > 0.1 \quad \Rightarrow \quad \text{intermittent regime,} \\ \text{else} \quad & \quad \Rightarrow \quad \text{oscillatory regime.} \end{aligned}$$

Mass ratio $\hat{m}$

Figure 4.8 a presents the non-dimensional maximum amplitude $\hat{A}$ *versus* the reduced flow velocities U_r for the prism with NES configurations with different mass ratios $\hat{m}$ of 0.02, 0.04, and 0.08, considering a constant radius ratio $\hat{r} = 0.6$ and a relative radial clearance $\hat{\mu} = 0.066$. The NES of the smallest mass ratio $\hat{m} = 0.02$ reduces the maximum amplitude in a small range of flow speeds $U_r \leq 19.2$. For mass ratios $\hat{m} = 0.04$ and 0.08, the prism maximum amplitude increases steadily with flow speeds until reduced flow velocities of 15.6 and 13.7, respectively. Then, it jumps at higher flow speed coinciding with the NES transition from the oscillatory to the intermittent regime and continues with slight changes until another higher jump exceeding the limit of the experiment at reduced flow velocities $U_r = 25$ and 27, respectively. This means that increasing the NES mass ratio expands the NES effective range. However, lower mass ratio NES configurations result in smaller vibration amplitudes in the low-speed range.

Figure 4.8 b shows a NES regime mapping for the three different mass ratios. The oscillatory regime ends at a reduced flow velocity between 14.7 and 16.5 for both mass ratios 0.04 and 0.08. The intermittent regime starts and remains only for a small range of velocities until $U_r = 16.5$. While for the smallest mass ratio, $\hat{m} = 0.02$, the oscillatory regime range expands to eliminate the occurrence of the intermittent regime. For the three different mass ratios, the rotational regime starts at the same reduced velocity of 16.5 until reaching the maximum allowed amplitude.

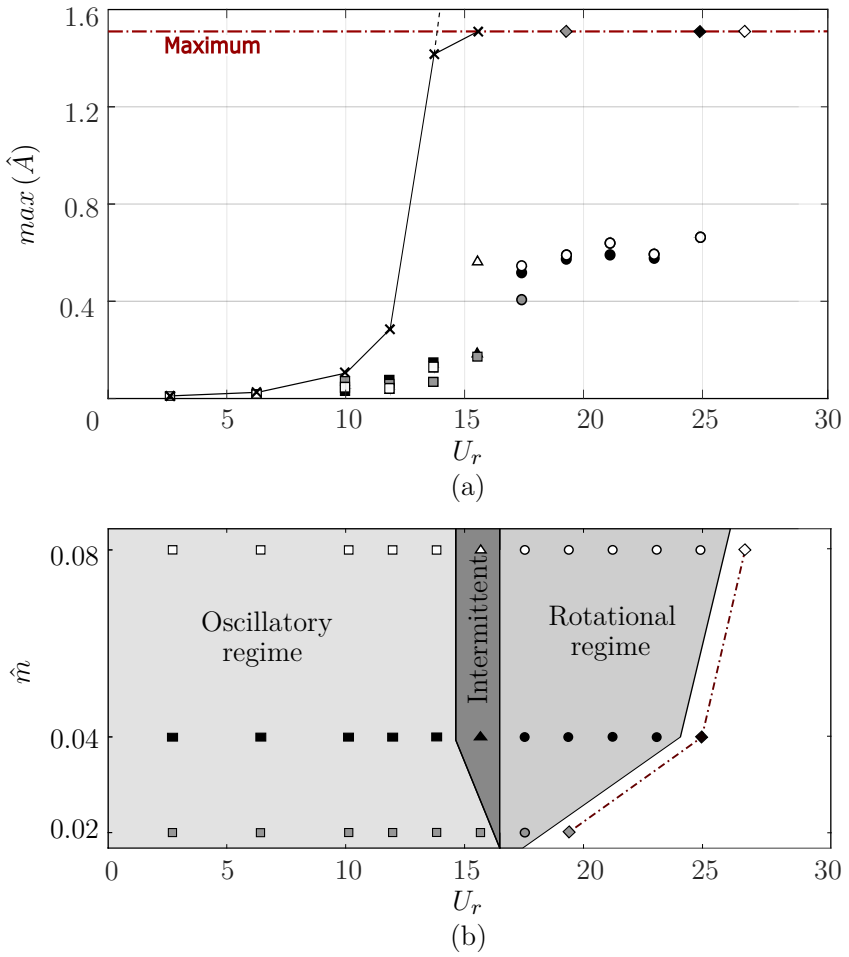

Figure 4.8 (a) Prism responses without ⇢ and with different mass ratio NESs $\hat{m}$= 0.02 (gray marks), $\hat{m}$ =0.04 (black marks), and $\hat{m}$=0.08 (white marks) at a constant $\hat{r}$ =0.6, (b) NES regime mapping presenting oscillatory ▫, Intermittent △, and Rotational ○ regimes, and the points that reach the maximum allowed amplitude ◇.

Radius ratio $\hat{r}$

The behaviour of the NES is greatly affected by the NES radius ratio. A ball of 56 g mass and 24 mm diameter is used to obtain three different radius ratios $\hat{r}$ = 0.4, 0.6 and 0.7, considering a constant mass ratio $\hat{m}$ = 0.04 and relative radial clearance $\hat{\mu}$ = 0.066.

Figure 4.9 a compares the prism responses with the three different NES configurations. The prism with the smaller radius ratio NES oscillates with lower amplitude. The NES effective range at a radius ratio $\hat{r}$ = 0.7 is smaller than that at lower radius ratios of 0.4 and 0.6. Thus, increasing the NES radius ratio results in increasing the prism vibration amplitudes and decreasing the NES effective range.

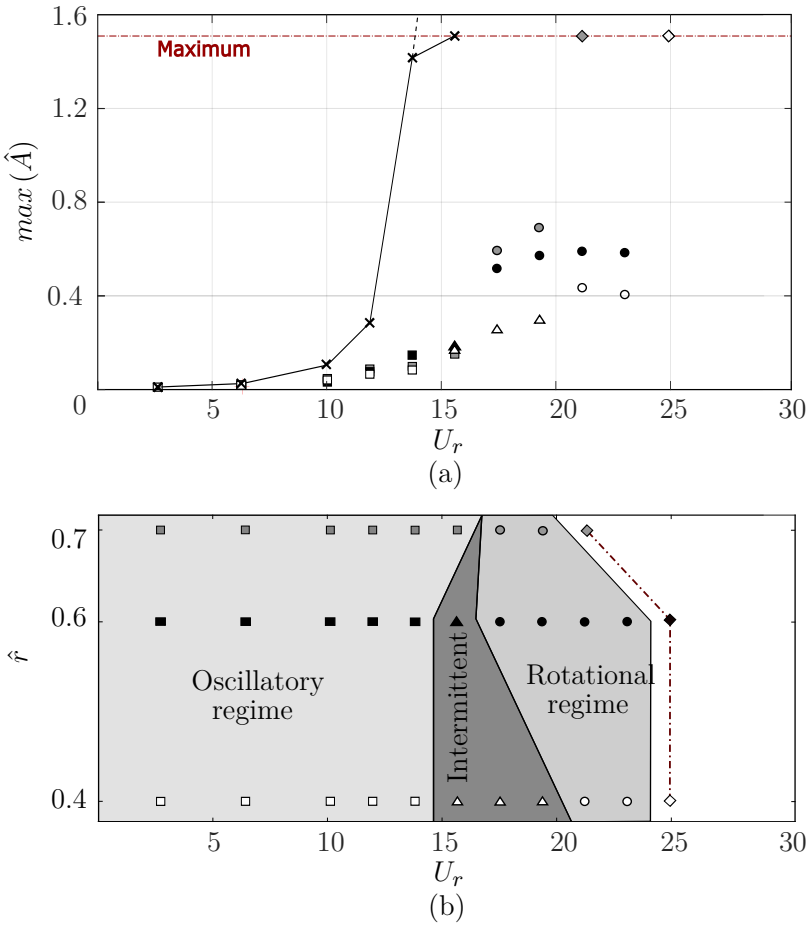

Figure 4.9 (a) Prism responses without ⊸ and with different radius ratio NESs $\hat{r}$= 0.7 (gray marks), $\hat{r}$ =0.6 (black marks), and $\hat{r}$=0.4 (white marks) at a constant $\hat{m}$ =0.04, (b) NES regime mapping presenting oscillatory ▫, Intermittent △, and Rotational ○ regimes, and the points that reach the maximum allowed amplitude ◇.

The NES regime mapping in Figure 4.9b shows the effect of NES radius ratio variation on the ball behaviour. The oscillating regime range is the same for both radius ratios 0.4 and 0.6 and expands to eliminate the occurrence of the intermittent regime at the radius ratio of 0.7. The intermittent regime is observed from a reduced velocity $U_r = 14.7$ and ends at reduced velocities of 20.3 and 16.5 for NES configurations with radius ratios 0.4 and 0.6, respectively. For the highest value of radius ratio $\hat{r} = 0.7$, the rotational regime starts directly after the oscillatory regime at a reduced velocity of 16.5. The starting reduced velocities of the rotational regime are 20.3, 16.5, and 16.5 at the different radius ratios of 0.4, 0.6 and 0.7, respectively. Hence, increasing the NES radius ratio has a significant effect in narrowing the intermittent regime range.

Ball friction

The ball damping ratio ζ_θ has an important effect on the NES behaviour. Ball damping comes predominantly from the friction between the ball and the NES track. It is difficult to get an exact value for the ball damping ratio as it depends on uncertain parameters such as air resistance, and the ball behaviour (rolling or slipping). We added lubricating oil to reduce the ball friction with the NES track walls. We tested a lubricated and a dry NESs with the same parameters $\hat{m} = 0.08$, $\hat{r} = 0.6$ and $\hat{\mu} = 0.066$ to investigate the effect of ball damping variation.

The prism responses with the two NES configurations are presented in Figure 4.10 a. The lubricated NES is more effective than the dry one in reducing the galloping amplitudes of the prism at the reduced flow velocities $13.6 < U_r < 17.4$. Figure 4.10 b shows the NES regime mapping for both the lubricated and the dry NES. The oscillatory regime range expands in the case of the lubricated NES to eliminate the appearance of the intermittent regime. While the rotational regime range is delayed by the lubricating fluid to start at a reduced velocity $U_r = 19.3$ instead of 17.4. A possible explanation for this finding is that the ball can rotate with higher angular speeds and absorb more energy from the system in the presence of lubrication due to decreased friction.

NES track relative clearance $\hat{\mu}$

Increasing the radial clearance $\hat{\mu}$ affects the ball rotation and increases the magnitude of the impacts between the ball and the NES track walls leading to different dynamics. Changing the inner bushing size allows achieving three relative NES track clearance values of 0.066, 0.2, and 0.33 for the same NES of mass ratio $\hat{m} = 0.08$ and radius ratio $\hat{r} = 0.61 \pm 0.01$.

The NES responses, presented in Figure 4.11 a, are highly affected by the radial clearance. Increasing the radial clearance reduces the prism galloping amplitude, however, it does not change the NES effective range. Figure 4.11 b presents the NES regime mapping for the three different radial clearances. Increasing the radial clearance widens the oscillatory regime range and shifts the intermittent regime with no change in its range. We observe the oscillatory regime up to reduced flow velocities of 14.7, 18.3, and 20.2 at different radial clearances of 1, 3, and 5 mm, respectively. The findings at higher radial clearance may be explained by the effect of the ball impact with the NES track walls that appear as an additional way for nonlinear energy absorption.

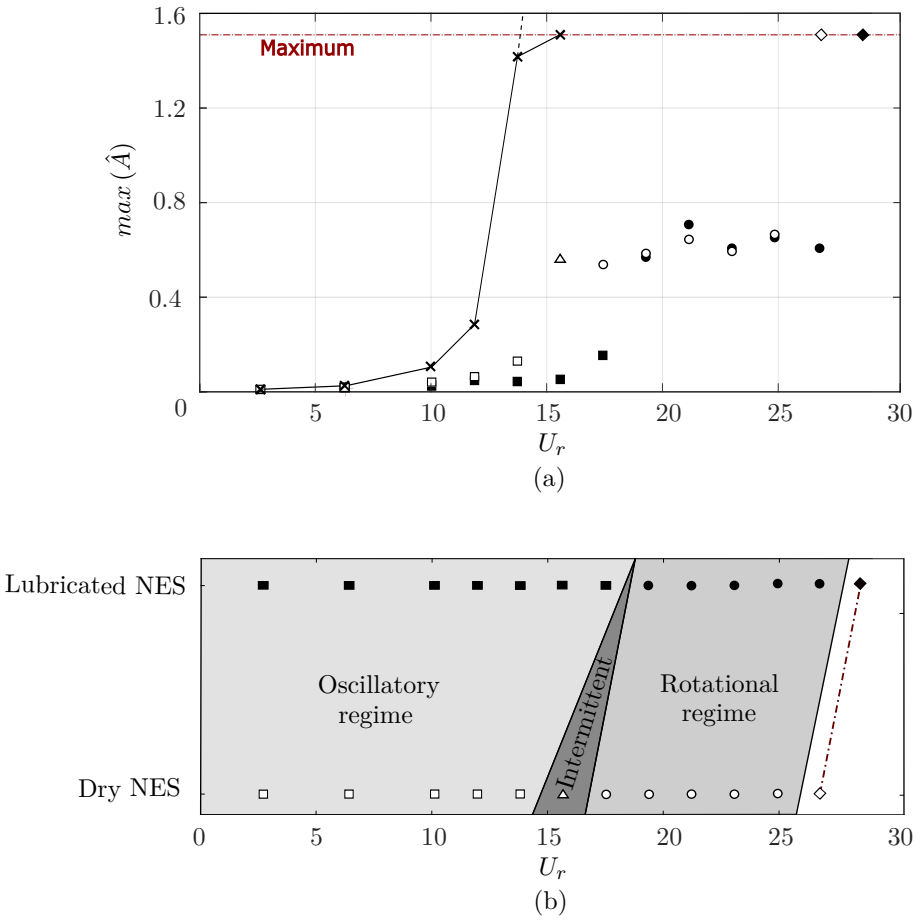

Figure 4.10 (a) Prism responses without $\nrightarrow\!\!\!\!\!\!\times$ and with a dry (white marks) and lubricated (black marks) NESs with the same mass and radius ratios $\hat{m}$= 0.08, $\hat{r}$ =0.6, (b) NES regime mapping presenting oscillatory ▫, Intermittent △, and Rotational ○ regimes, and the points that reach the maximum allowed amplitude ◇.

4.4 Conclusion

The typical form of a rotative NES presented in the literature consists of a tip mass coupled to a primary structure by a rigid bar of fixed length. In this research, we designed a new rotative NES using a free metal ball moving in a circular track without direct coupling to the primary system proposing a simple, robust and effective way of nonlinear energy absorption. At least to the authors' knowledge, experimental investigation focusing on the galloping suppression using NES is not found in the literature and is the major novelty of this paper.

The rotative NES proposed in this study successfully mitigates the galloping of a square prism with no effect on its natural frequency. Wind tunnel experiments exposed the mechanism of

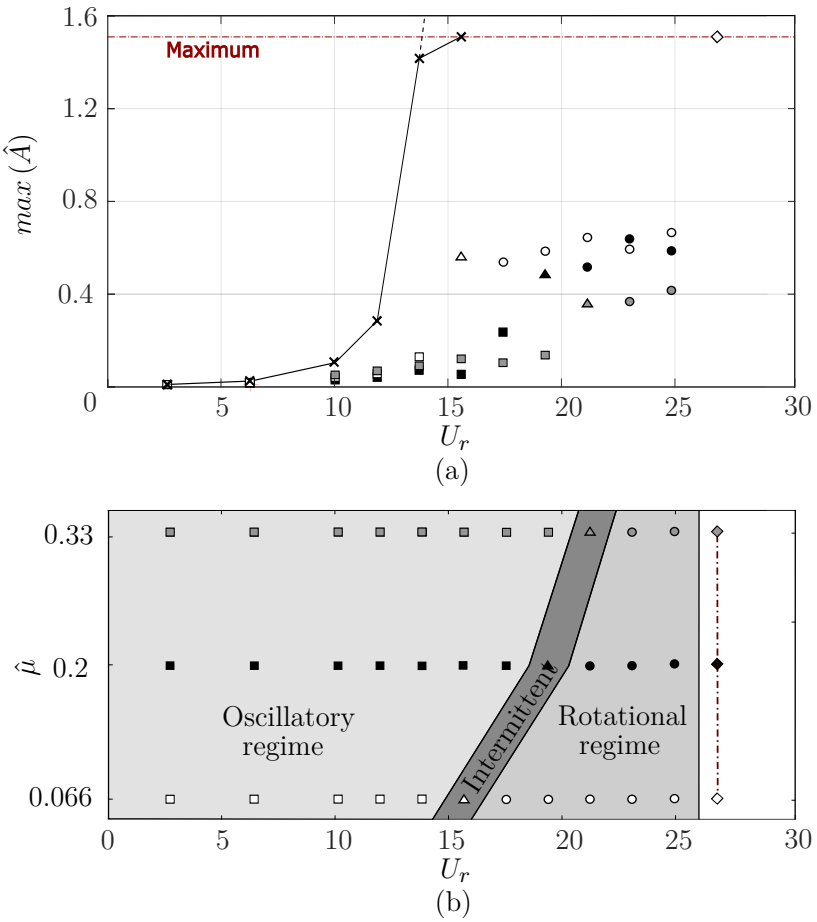

Figure 4.11 (a) Prism responses without ⇜ and with NESs of varying track relative clearance ; $\hat{\mu}$= 0.33 (gray marks), $\hat{\mu}$=0.2 (black marks), and $\hat{\mu}$=0.066 (white marks) at a constant mass and radius ratios $\hat{m}$ =0.08, $\hat{r}$ =0.61 ±0.01, (b) NES regime mapping presenting oscillatory ▫, Intermittent △, and Rotational ○ regimes, and the points that reach the maximum allowed amplitude ◇.

action of the proposed NES and highlighted its three different response modes: oscillatory regime, intermittent regime, and rotational regime. At low flow speeds in the oscillatory regime, the NES ball oscillates with a small amplitude not exceeding 70 degrees, however, it increases the critical galloping velocity. At higher flow speeds, the intermittent regime appears within a small flow speed range. The ball oscillates with relatively low angular speeds to keep the prism amplitude less than 30 mm resulting in a nearly steady vibration of the prism. At higher flow speeds still, the rotational regime shows the maximum reduction for the prism vibration, where the NES ball rotates with high angular speeds and absorbs a high amount of energy. The ball rotation directly reduces the prism vibrations resulting in periodic cycles of reduction and growing in the prism vibration displacement.

The design of the NES allows for easy changes of its main parameters by swapping some components. Capitalising on this advantage, we experimentally quantified the influence of the main NES parameters on both the prism galloping response and the NES regime mapping over flow velocities. Increasing the mass ratio increases the NES effective range, and leads to the appearance of the intermittent regime coinciding with a small jump in the prism amplitude response. On the contrary, increasing the radius ratio decreases the NES effective range, and reduces the intermittent regime range rising the prism vibration amplitudes. Decreasing the ball friction with the NES track increases the NES effective range, and reduces the intermittent regime range. Hence, it eliminates the small jump in prism amplitude coinciding with the starting of the intermittent regime. We highlight the clearance between the NES track walls and the rotating ball as an effective parameter. Increasing the radial clearance significantly reduces the prism vibration amplitudes. For the range of parameter values considered here, the most efficient NES possess the highest mass ratio and radial clearance, and the lowest radius ratio.

The simple structure of the presented NES may extend its usage to many applications. It can damp wind-induced galloping on different types of structures such as power lines, high mounted signboards, long slender structures and skyscrapers. Our experiments are limited to a maximum non-dimensional amplitude of 1.5. Consequently, an accurate numerical model is important in future work to predict the NES behaviour and prism dynamics at high vibration amplitudes. These mathematical models are under development.

CHAPTER 5 ARTICLE 2: HOW A BALL FREE TO ORBIT IN A CIRCULAR TRACK MITIGATES THE GALLOPING OF A SQUARE PRISM

Michael M.Selwanis, Guilherme R.Franzini, Cédric Béguin, and Frédérick P.Gosselin

This chapter represents the second article, submitted to "Nonlinear Dynamics" in October 2021. Preprint DOI : https://doi.org/10.21203/rs.3.rs-973095/v1.

Abstract

Transverse galloping is a type of flow-induced vibration (FIV) that leads to critical design considerations for engineering structures. A purely nonlinear energy sink (NES) composed of a ball free to rotate in a circular track experimentally mitigated the galloping of a square in a previous study. The current study introduces a model for simulating the dynamics of the square prism coupled with a ball-in-track (BIT) NES and predicting the system behaviour at high flow speeds beyond the limits of the previously presented experiments. Numerical simulations employ the fitting of experimental data as inputs to define parameters. Wind tunnel static experiments provide the galloping force coefficient C_y relative to the prism angle of attack. Additionally, free rotation tests allow evaluating the ball damping coefficient c_θ as a function of its mass and the NES track radius. The result of the rotation tests provides a critical angular speed beyond which the ball damping increases non-linearly. We point out the damping variation as an advantage of the BIT-NES ; less damping at low angular velocities helps the ball start its rotation, while relatively large damping at higher speeds dissipates more energy from the vibrating system. Numerical results exhibit four response modes for the NES ; oscillatory at low flow speeds, intermittent within a small range of higher flow speeds, rotational at higher flow speeds, and ineffective regime at flow speeds out of the NES effective range. Modelling the primary mass as a parametric excitation source for the NES provides an analytical estimation of the boundary between the oscillatory and intermittent regimes. Furthermore, we advance an analytical analysis of the power flow across the integrated prism-NES system to explain the NES behaviour and predict the limit of its effective range.

Keywords : Nonlinear energy sink, Ball-in-track (BIT) NES, Vibration suppression, Square prism, Galloping, Energy transfer, Wind tunnel tests, Ball Friction, Power analysis.

5.1 Introduction

Nonlinear energy sinks (NESs) represent a specific class of vibration absorbers. A typical NES is composed of a mass attached to the primary system by a spring element of non-linearizable stiffness and appropriate damping properties. The absence of linear natural frequencies enables such absorbers to engage with the dynamics of the primary structure and reduce its vibration amplitudes over a wide range of frequencies [13]. Purely nonlinear energy sinks are a particular type of these devices with no direct coupling to the primary structure [98, 99], and interact with the principal vibrating system only due to dynamical interaction. In general, the NES works according to the Targeted Energy Transfer (TET) theory of Gendelman [73], which is also referred to as energy pumping [152]. This key-concept states that a portion of the energy is transferred irreversibly from the vibrating system to the NES as kinetic energy during the NES motion, reducing the vibration amplitude without a significant change in the system characteristics.

The interest in the area of nonlinear energy absorption has resulted in the development of many designs for NESs. Depending on the NES degree of freedom, we can find two different types ; the translative NES that only makes a translational motion [49, 153], and the rotative NES [20] composed of a rotating masss. A Vibro-impact NES is a more advanced type [22] that uses the impact of the NES mass with the walls of the structure as an additional way of energy absorption. The purely rotative NES is a simple and promising device that can damp vibration without a spring element [45].

Following the explanation of the energy transfer phenomena that automatically occurs between a primary linear oscillator and a nonlinear damper [74], Vakakis [26] applied the NES to mitigate the response of a structure subjected to an impulse load. Since then, engineers have applied the NES in several applications, including civil engineering structures, mechanical systems, aeronautics and energy harvesting. In the civil engineering field, the NES absorbs the seismic excitation [28] of structures, and protects buildings from earthquake loading [29]. The NES was presented as a suppressor for structural elements such as beams [30], and plates [31]. Many studies implemented the NES as a vibration absorber in different mechanical systems ; rotary systems [33], flywheel [32], and self-excited systems [34]. Moreover, NESs can suppress the vibrations of helicopter blades [35]. Besides the NES damping effect, integrating such oscillators in piezoelectric [37] or magneto-electric [36] systems is an intriguing way for harvesting the energy of a vibrating system.

Concerning the mitigation of flow-induced vibrations, NESs were able to delay the flutter instability of wings [38, 157] and mitigate the oscillations of pipes conveying fluid [40].

NESs of various designs have been implemented in many structures to reduce the impact of flow-induced vibrations. Tumkur et al. [41] computationally simulated the vortex-induced vibration (VIV) of a cylinder coupled with a translative NES, which could reduce the VIV amplitudes by 70 %. In a comparable study, Mehmood et al. [42] discussed the effect of initial conditions considered in the simulation on the NES efficiency. Further, Dai et al. [43] computed the fluid loads affecting a cylinder due to VIV using the wake-oscillator models and highlighted the strongly modulated response resulting from the energy transfer with a translative NES. Blanchard et al. [44] adopted computational fluid dynamics (CFD) for estimating the fluid forces and demonstrated that a rotative NES similarly modulates the cylinder dynamics. NES parameters, particularly the mass, affect its capability of reducing the vibration amplitude of the cylinder [45]. Recently, Franzini [145] has used an extensible arm with a tip-mass added to add a radial degree of freedom to the traditional rotative NES, which increased the NES suppression resulting in a 25% decrease in the maximum amplitude of a cylinder in VIV.

Only a few researchers have introduced the NES as a suppressor for transverse galloping, which is another type of flow-induced vibration generated by heavy winds that can lead to catastrophic effects on high rising structures. A numerical study [46] investigated the effect of a translative NES in delaying the galloping of a square prism, demonstrating the influence of NES parameters on its behaviour. In a similar problem, a rotative NES reduced the galloping amplitudes of a prism to 50 % of its original values [47]. The Quasi-steady approach [54] was used for describing the galloping forces. Indeed, square prism galloping involves a hysteresis phenomenon due to a pitchfork bifurcation of the galloping solution within a small range of flow speeds beyond the galloping onset velocity. In this parameter range, the prism amplitude depends on the initial conditions ; it exhibits a lower limit cycle for increasing flow speed (small initial displacement) and follows the upper branch limit cycle on decreasing flow speed (large initial displacement). In studies using NESs to mitigate galloping, this phenomenon is ignored by considering only small initial displacements for the vibrating prism. The discussion stated that the NES delayed the galloping but did not address the NES ability to absorb the high-amplitude galloping that already occurred. We proposed a purely rotative NES composed of a free ball rotating freely in a circular track to mitigate the galloping of a square prism in a previous study [158]. The rotating ball engaged with the system dynamics and successfully reduced the galloping amplitudes over a wide range of flow speeds in wind tunnel experiments. The limitation of the experimental setup restricted the tests of high-amplitude galloping.

Here we present a mathematical model for the coupled system of the galloping prism and the BIT-NES to simulate its dynamics in a parameter range not easily accessible in experiments.

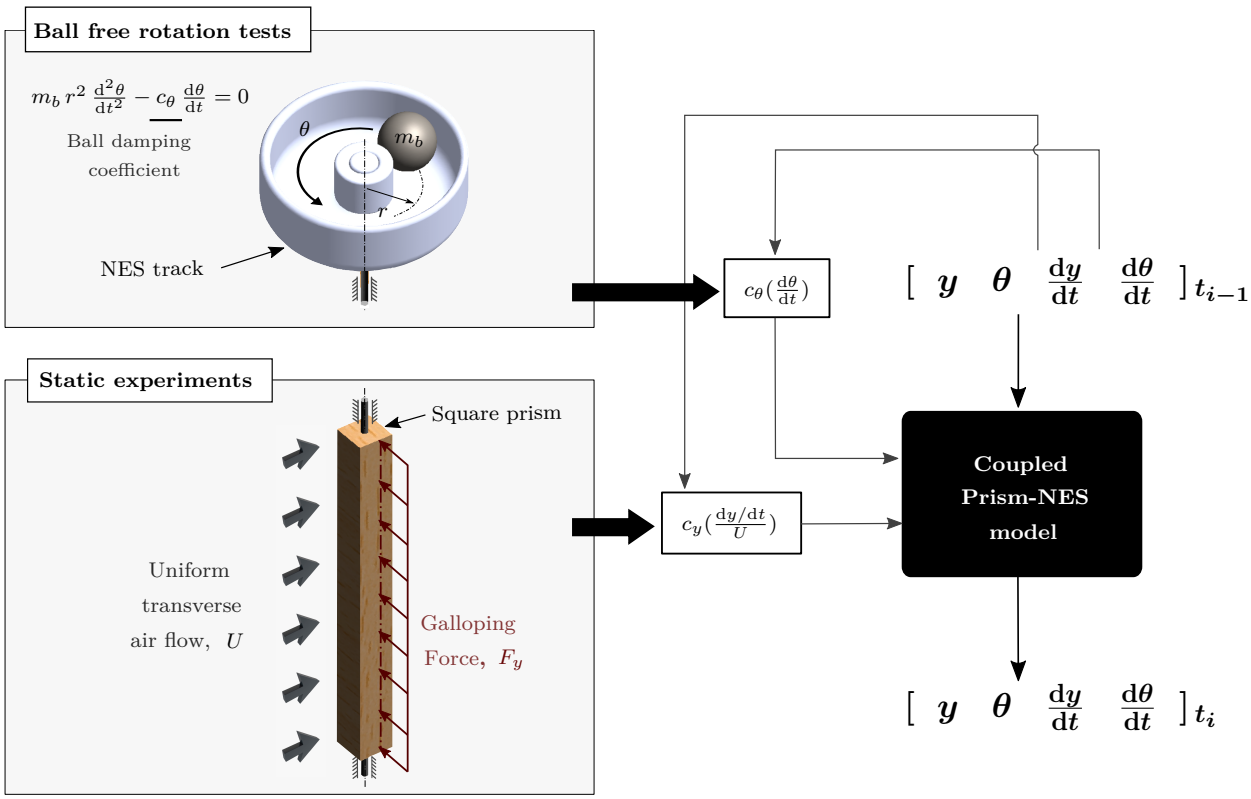

Figure 5.1 Diagram showing the ball rotation decay experiments, static wind tunnel experiments and the proposed model that employs these experimental data as inputs to integrate position and velocity of prism y, $\frac{dy}{dt}$ and ball θ, $\frac{d\theta}{dt}$ from time t_{i-1} to time t_i.

Quasi-static experiments characterise the galloping force coefficient of the prism model C_y as a function of the angle of attack. Additionally, we estimate the ball damping coefficient c_θ from the decay rate of the ball angular speed in free rotation tests. The developed model, schematized in Figure 5.1, employs the measurements of C_y and c_θ as inputs to compute the prism response.

The paper is structured in four sections. Following the introduction, Section 5.2 presents the proposed model and the evaluation of of each of the galloping force C_y and the ball damping coefficients. Additionally, this section demonstrates the experimental setup and the results of both the wind tunnel static experiments and the free rotation tests. Section 5.3 exhibits the numerical results for the prism response with and without the NES, showing the NES capability in delaying the galloping occurrence and its dynamics at different response modes. In Section 5.4, we derive an analytical estimation for the limit boundary of the NES oscillatory

regime, depending on modelling the primary system mass as a parametric excitation source for the NES. Besides, a power flow analysis of the prism-NES coupled system provides an analytical expectation for the critical flow speed, beyond which the NES can not mitigate high-amplitude galloping. Finally, Section 5.5 addresses the conclusion.

5.2 Mathematical model

Our model simulates the dynamics of a square prism system coupled with a rotative NES (Figure 5.2). We consider an elastically supported square prism of mass M, length l and side length D that vibrates transversely to a free stream of velocity U under the effect of the supporting equivalent stiffness k, and the structural damping coefficient c . A ball of mass m_b rotating freely in a circular track of mean radius r represents the rotative NES. The friction between the rotating ball and the NES track results in a ball damping coefficient c_θ. The NES ball rotates due to dynamic interaction with the prism vibration reaching its own angular coordinate θ (positive in counter-clockwise direction) independently of the prism displacement y. Hence, a 2-DOF mathematical model simulates the dynamics of our system ; the equation of motion of the vibrating prism in the transverse direction to the flow and ball equation of motion in the tangential direction.

$$(M + m_b)\,\frac{\mathrm{d}^2 y}{\mathrm{d}t^2} + m_b r\left(\frac{\mathrm{d}^2\theta}{\mathrm{d}t^2} sin\theta + (\frac{\mathrm{d}\theta}{\mathrm{d}t})^2 cos\theta\right) + c\dot{y} + ky = \frac{1}{2}\rho U^2 lD\, C_y, \tag{5.1}$$

$$m_b r^2\,\frac{\mathrm{d}^2\theta}{\mathrm{d}t^2} + m_b r\frac{\mathrm{d}^2 y}{\mathrm{d}t^2}\, sin\theta + c_\theta\,\frac{\mathrm{d}\theta}{\mathrm{d}t} = 0. \tag{5.2}$$

where C_y is the galloping force coefficient, and the natural frequency of the prism is defined as $\omega = \sqrt{\frac{k}{M+m_b}}$. To evaluate the parameters of our experimental system, we experimentally estimate the galloping force coefficient C_y and the ball damping coefficient c_θ, to use them as inputs for the numerical model.

5.2.1 Measurement of the galloping force coefficient

Through static experiments in the closed-loop wind tunnel of the mechanical engineering department of Polytechnique Montréal (Model 407-B, ELD, Lake City, MN, USA), a 6-axis force/torque balance of 0.0125 N and 0.001 N.m resolution (GAMMA, ATI Industrial Automation, Apex city, NC, USA) measured the galloping force coefficient of a square prism (Figure 5.3). A square prism model, Figure 5.3a, of length l and side length D made of balsa wood, the same model presented in our previous study [158], is fixed to the force balance (5)

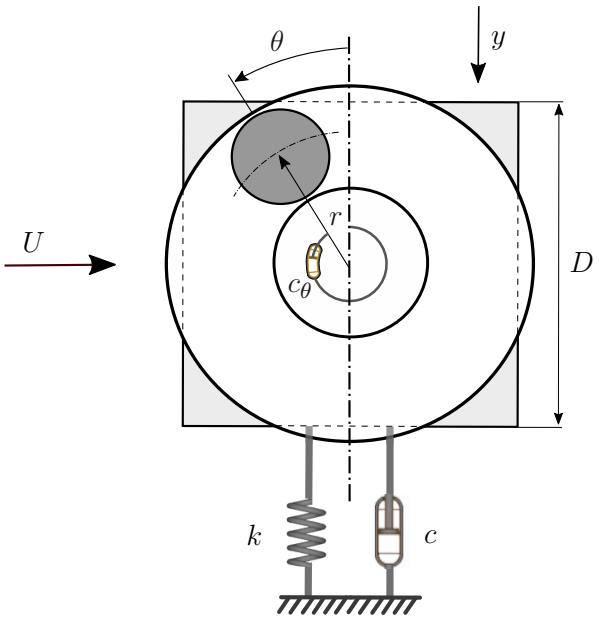

Figure 5.2 Schematic drawing of the prism-NES integrated system

from the upper end. A thin plate of Formica (8) attached to the lower side of the test section supports the other end of the prism preventing any deflection in the X-Y plane. We install two plates (7), of 15 cm length and 14 cm width, 8 cm away from the ends of the prism to help approach two-dimensional flow conditions ; see Bearman et al. [56]. The lengths between the ends of the prism and the supporting are l_1 and l_2 at the lower and upper ends, respectively. The force balance rotates with a servo motor (BE231FJ-NPSN, Parker, Cleveland city, OH, USA) to directly measure the reaction force R_y and the moment M_x as shown in Figure 5.3 a.

To eliminate any error that may arise from the deviation in the angle measurement, the KolmogorovSmirnov (K-S) test compared the C_y values measured at the positive and those measured at the negative angles of attack. This statistical method mainly quantifies how the distribution functions of two data samples are similar. A developed MATLAB code shifted the measured C_y curves within the uncertainty ranges by 0.65^o to achieve the best symmetry based on the KolmogorovSmirnov test, see appendix A. A spline of a smoothing parameter $p = 0.999995$ fitted the measured data after eliminating the systematic error representing the final C_y curve as a function of the prism angle of attack, $\alpha = (\mathrm{d}y/\mathrm{d}t)/U$.

$$C_y = 1.813\left(\frac{\mathrm{d}y/\mathrm{d}t}{U}\right) + 24.15\left(\frac{\mathrm{d}y/\mathrm{d}t}{U}\right)^3 - 563.3\left(\frac{\mathrm{d}y/\mathrm{d}t}{U}\right)^5 + 459\left(\frac{\mathrm{d}y/\mathrm{d}t}{U}\right)^7. \tag{5.3}$$

Based on the static equilibrium state of the prism (Figure 5.3b) and assuming a uniform

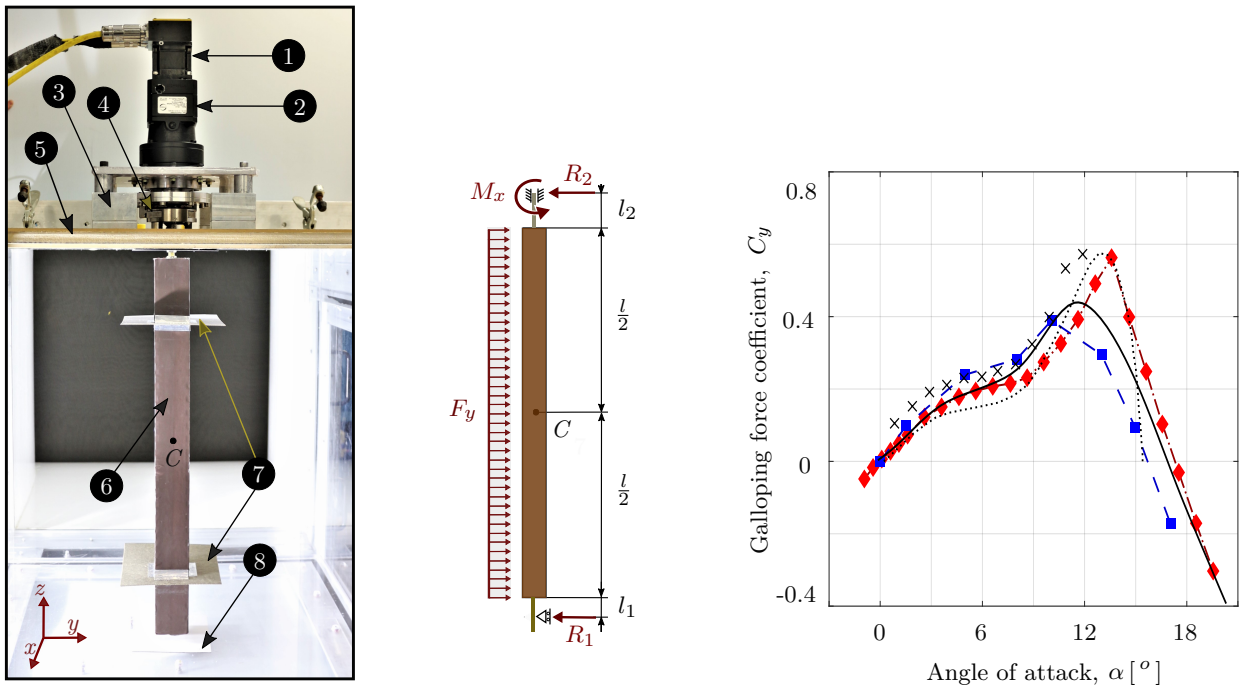

(a) (b) (c)

Figure 5.3 (a) Static experiments setup ; 1- servo motor, 2- gear reducer, 3- aluminum frame, 4- Force balance, 5- a wooden panel, 6- square prism model, 7- inner plates, 8- outer plates. (b) Free body diagram of the square prism. (c) C_y variation with square prism angle of attack α ; —C_y curve of the current study at $Re = 101 \times 10^3$,(see Appx. A for more details), -■-Naudascher et al. [57] at $Re = 106 \times 10^3$, -◆-Wawzonek [159] at $Re = 12.4 \times 10^3$, ·····Parkinson and Smith [54] at $Re = 22.3 \times 10^3$, × Bearman et al. [56] at $Re = 14 \times 10^3$.

distributed aerodynamic loading along its length, we compute the galloping force F_y from the measured loads M_x and R_2. R_1 and R_2 are the reaction forces in y-direction at the lower and upper ends of the prism, respectively, and M_x is the moment measured by the force balance at the upper end of the prism in x-direction.

$$F_y = \left(\frac{l + l_1 + l_2}{l/2 + l_1}\right) R_2 + \left(\frac{1}{l/2 + l_1}\right) M_x = \frac{1}{2} C_y(\alpha)\, \rho\, U^2 l D, \tag{5.4}$$

where ρ is the flow density, U is the speed of air stream, l is the length of the prism, D is the side length of the square prism, and C_y is the galloping force coefficient. We measured F_y at different angles of attack α, starting from 0^o to 27^o using a step of 3^o in both directions. For each angle, the measurement starts after setting the zero value of the sensor at a stationary flow condition to avoid any residual force with the motor due to rotation. We measure

the aerodynamic coefficient at a fixed flow speed $U = 30\,\mathrm{m/s}$ that corresponds to $Re = 101 \times 10^3$. In each test, two minutes elapsed after reaching the required flow speed to ensure a steady-state. Then, we recorded 150 values of the force coefficient C_y in the consecutive 30 seconds, from which we estimate the average value with a range of fluctuation. Measurement fluctuation was always below 2.5% for all reported readings.

In Figure 5.3b, we compare our measurements to some of the previously published data [54, 56, 57, 159]. Comparing to Naudascher et al. [57], the measured C_y curve has a small difference of 0.05 in the maximum value of C_y and a shift of 2 degrees in the angle of attack corresponding to it. Other measurements at lower Reynolds number $12 \times 10^3 < Re < 23 \times 10^3$ show a higher maximum value for C_y that corresponds to higher angles of attack. Otherwise, all measurements are close for angles of attack below 12^o. Accordingly, we use the C_y fitting of our experiments as an input for the numerical model to introduce accurate values for $C_y(\alpha)$, presenting the specificity of our model.

5.2.2 Representation of the ball damping coefficient

The ball dynamics is more complicated than that of an attached mass in the traditional rotative NES. The ball behaviour exhibits a combination of sliding and rolling. Characterizing the ball damping is a considerable challenge for the realistic simulation of the prism-NES dynamics. We performed free-rotation tests for estimating the ball damping coefficient. The exponential decay curve of the maximum amplitude represents the damping in a traditional mass-spring system. For the ball's continuous rotation in our NES, it is convenient to calculate the ball damping from the decay of its angular speed. Since the decay curve varies exponentially, the exponential power used for estimating the damping coefficient does not change.

In the free-rotation tests, a step motor (CM231FJ-115753, Parker) clamped on a wooden plate of a metal-frame test rig rotates the NES track (Figure 5.4a). A precise metal adaptor directly connects the motor axis with the NES track to enable fast rotation. For safety requirements, a hollow cylindrical shield of acrylic surrounds the NES to prevent any damages that could result from the ball flying out of the track. We control the angular position, speed and acceleration of the motor to rotate the NES for six complete revolutions at a 50 rad/s angular speed. Then, stopping the motor allows the ball to rotate freely, overcoming the friction with the track walls. A high-speed camera captures the angular position of the ball with a resolution of 0.2^o to allow for post-treatment image analysis. A developed MATLAB code traces the position of the ball and estimates its average speeds over a revolution $(\mathrm{d}\theta/\mathrm{d}t)_i = 2\pi/T_i$, where T_i is the time taken by the ball to complete the i^{th} revolution.

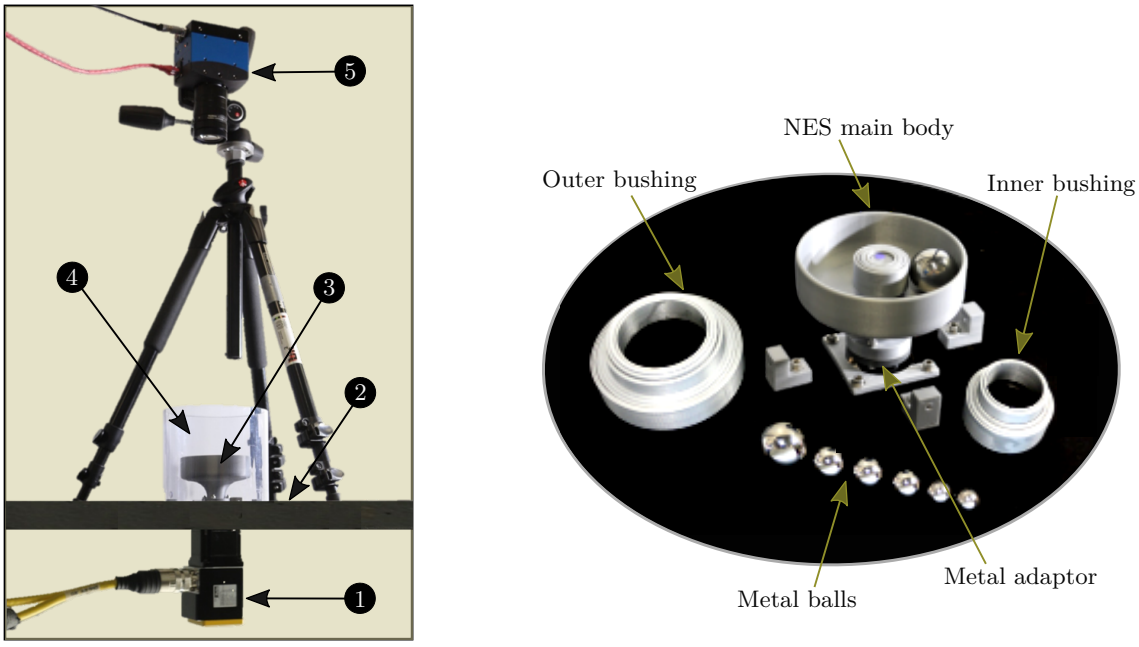

(a) (b)

Figure 5.4 Free-rotation tests : (a) Experimental setup ; 1- servo motor, 2- test rig, 3- the rotative NES, 4- cylindrical shield, 5- high-speed camera. (b) Exploded view of the NES.

Depending on the linear variation of the ball angular positions in the free rotation test (Figure 5.5a), we assume a constant ball angular speed $(\mathrm{d}\theta/\mathrm{d}t)_i$ over each complete revolution. Figure 5.5b presents the decay of the angular speed of a 111 g ball rotating in a circular track of a mean radius $r = 30\,\mathrm{mm}$. The ball speed $\dot{\theta}$ decreases rapidly from 40 to 7.7 rad/s, then the rate of decay diminishes for $(\mathrm{d}\theta/\mathrm{d}t) < 8$ rad/s. Two exponential curves were required for the best fitting of all the estimated values of the ball angular velocity. Each of them provides a ball damping coefficient for a certain angular speed range. The exponential term e^{bt} represents the decay rate of the ball angular speed, where $b = c_\theta/2m_b r^2$ based on the equation of motion of a free-rotating ball in the tangential direction

$$\frac{\mathrm{d}^2\theta}{\mathrm{d}t^2} + \frac{c_\theta}{m_b\, r^2}\,\frac{\mathrm{d}\theta}{\mathrm{d}t} = 0. \tag{5.5}$$

The free-rotation test of this NES configuration provides a damping coefficient $c_{\theta 2} = 0.00018$ kg.m^2/s at high ball angular speeds $(\mathrm{d}\theta/\mathrm{d}t) > 7.5$ rad/s, and a smaller one $c_{\theta 1} = 0.000017$ kg.m^2/s at lower speeds.

The NES design (Figure 5.4b) allows for changing the width and the mean radius of the track using 3D-printed bushings of small thickness to accommodate different ball sizes. We

performed free-rotation tests for many NES configurations. The behaviour observed using the 111 g ball was a general behaviour observed in the free-rotation tests of other NES configurations, whose results are shown in Table 5.1. We fitted each of the two damping coefficients by a spline curve to express it as a function of the ball mass (m_b) and the NES track mean radius (r). Then employ it as an input for the numerical model working with different NES configurations.

$$\begin{aligned} c_{\theta_1} = (&0.4 + 1.7\, m_b - 45.1\, r - 52.6\, m_b^2 + 23.9\, m_b\, r + 1694\, r^2 \\ &+35.6\, m_b^3 + 1917\, m_b^2\, r - 5483\, m_b\, r^2 - 19940\, r^3) \times 10^{-4}, \end{aligned} \tag{5.6}$$

$$\begin{aligned} c_{\theta_2} = (&-0.3 + 0.2\, m_b + 32.2\, r - 2.4\, m_b^2 - 15.1\, m_b\, r - 1232\, r^2 \\ &-52.5\, m_b^3 + 352.9\, m_b^2\, r - 1818\, m_b\, r^2 + 15590\, r^3) \times 10^{-3}. \end{aligned} \tag{5.7}$$

The ball damping experiments come with a critical angular speed $(\mathrm{d}\theta/\mathrm{d}t)_c = 8 \pm 1.2$ rad/s, above which we can not ignore the ball contact with the NES sidewall.At higher angular speeds, the ball contacts two surfaces, the NES flour and the outer sidewall. As a result, it slides and experiences more friction. The friction variation is a considerable advantage for the ball-in-track NES over the traditional rotative NES. Less friction at low speeds helps the ball to rotate, while the increased friction at high speeds dissipates more energy from the system.

5.2.3 Non-dimensional analysis and Model validation

For generalisation, we define non-dimensional parameters : non-dimensional vibration displacement Y ; dimensionless time τ ; structural damping ratio ζ_y ; ball damping ratio ζ_θ ; mass

Table 5.1 Ball damping coefficients [kg.m/s] of different NES configurations.

	$m_b = 0.014$ kg		$m_b = 0.028$ kg		$m_b = 0.056$ kg		$m_b = 0.111$ kg	
r [m]	c_{θ_1}	c_{θ_2}	c_{θ_1}	c_{θ_2}	c_{θ_1}	c_{θ_2}	c_{θ_1}	c_{θ_2}
0.02	2	11	3.4	24	5.4	44		
0.025	2.9	15	4.7	34	8.3	61	14.2	134
0.03	3.8	22	7.1	48	11.3	88	16.8	183
0.036	5.2	26	8.9	55	18.7	115		

Note : All the values in the table should be multiplied by $\times 10^{-6}$ to define the ball damping coefficient c_θ in kg.m^2/s.

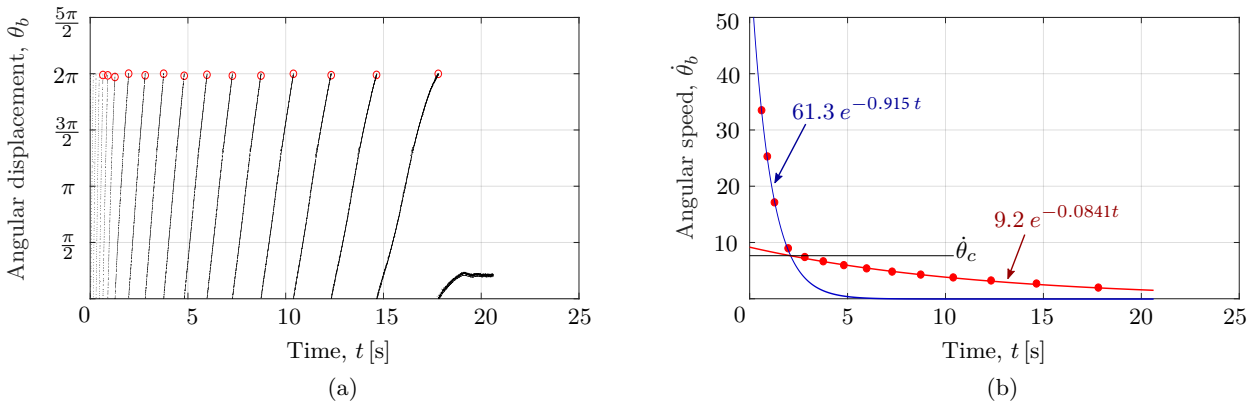

Figure 5.5 Results of the free rotation tests; (a) Ball angular position *vs* time, marking the end of each revolution (○). (b) The decay in the ball angular speed over each revolution, representing the measured values (●) and the exponential fittings (— $61.3\, e^{-0.915\, t}$, — $9.2\, e^{-0.0841\, t}$).

ratio (reference air-flow) m^*; reduced velocity U_r; NES mass ratio $\hat{m}$ and radius ratio $\hat{r}$:

$$\begin{aligned} Y &= \frac{y}{D}, \qquad \tau = \omega t, \qquad \zeta_y = \frac{c}{2\,(M+m_b)\,\omega}, \qquad \zeta_\theta = \frac{c_\theta}{2 m_b r^2\,\omega}, \\ U_r &= \frac{U}{\omega D}, \qquad m^* = \frac{M+m_b}{\rho l D^2}, \qquad \hat{m} = \frac{m_b}{M+m_b}, \qquad \hat{r} = \frac{r}{D}. \end{aligned} \tag{5.8}$$

Accordingly, the governing equations can be expressed in the non-dimensional form as

$$\ddot{Y} + 2\zeta_y \dot{Y} + \hat{r}\,\hat{m}\left(\ddot{\theta}\sin\theta + \dot{\theta}^2\cos\theta\right) + Y = \frac{U_r^2}{2m^*} C_y, \tag{5.9}$$

$$\ddot{\theta} + 2\zeta_\theta\,\dot{\theta} + \frac{\ddot{Y}}{\hat{r}}\sin\theta = 0. \tag{5.10}$$

where; $(\dot{\cdot})$ is the derivative with respect to the dimensionless time τ.

To validate our model, the simulated response of the prism-NES system, as well as the boundaries between NES regimes, are compared with the experiments reported by Michael M. Selwanis et al. [158]. We consider different NES configurations presented in the reference experiments; $\hat{m} = 0.08$, 0.04 and 0.02 at a constant $\hat{r}$ of 0.6 (Figure 5.6a), and $\hat{r} = 0.7$, 0.6 and 0.5 at a constant $\hat{m}$ of 0.04 (Figure 5.6b). All the comparisons are done for low amplitude galloping responses below $\hat{A} = 1.5$ due to the experiment's amplitude limitation. The experiments provided measurements at certain flow speeds for the galloping amplitudes and characterized three regimes for the NES, which we present with different marks. While the

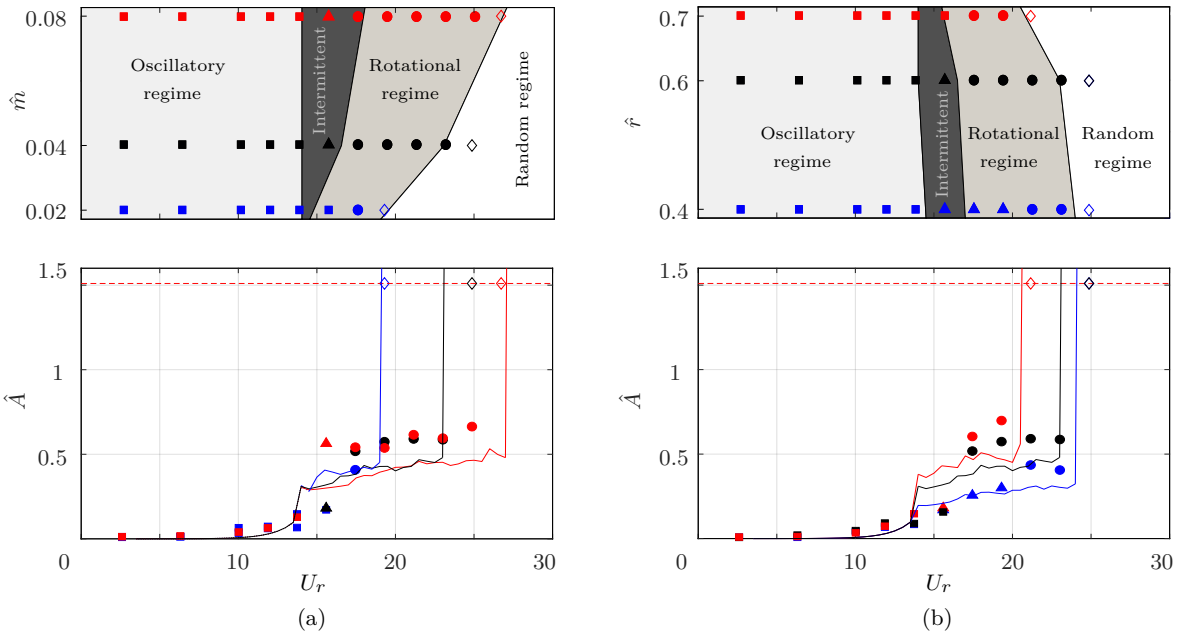

Figure 5.6 Model validation comparing the our simulations for the prism response (continuous curves) and the NES regime mapping with the previous experiments [158], represented by marks for each of the NES regimes ; oscillatory ■, Intermittent ▲, and Rotational ● regimes, and the points that reach the maximum allowed amplitude ⋄. The comparison are done for six various configuration of the NES : (a) $\hat{m} = 0.08$ (red), $\hat{m} = 0.04$ (black) and $\hat{m} = 0.02$ (blue) at constant $\hat{r} = 0.6$, (b) $\hat{r} = 0.7$ (red), $\hat{r} = 0.6$ (black) and $\hat{r} = 0.4$ (blue) at constant $\hat{m} = 0.04$.

simulations are presented by continuous lines and the boundaries estimated for each regime are shaded by different colours to exhibit the NES regime mapping.

The prism response curves present the maximum amplitude of the prism *versus* the reduced flow velocity. At low flow speeds, the prism is stable with the NESs of $\hat{r} = 0.6$ (Figure 5.6a) until the galloping onset speed $U_c = 11$, beyond which the prism amplitude jumps to $\hat{A} = 0.6$ in the experiments and to 0.4 in the simulations. The NES mitigates the prism vibration delaying the occurrence of large-amplitude galloping to a critical flow speed U_{crit}. The experiments reveal a range for U_{crit} between the velocity at which the prism amplitude hits the setup limitation ($\hat{A} = 1.5$) and the previously recorded point. The numerical predictions for U_{crit} agree with the range of experiments for most cases. However, we observe a small deviation between the estimated value and the experiments in the case of $\hat{m} = 0.08$ and $\hat{r} = 0.6$. Figure 5.6 b presents the prism responses with NESs of $\hat{m} = 0.04$ and variable $\hat{r}$. Decreasing the NES radius reduces the prism amplitudes and increases U_{crit}. The estimated prism amplitudes show an acceptable deviation compared to the measured values. Regarding the NES regime mapping, the boundaries between the oscillatory and the intermittent

regimes predicted by the numerical model match with the experiments in all cases except two : the NES of $\hat{m} = 0.02$ and $\hat{r} = 0.6$, U_{crit} =14 instead of 16, and the NES of $\hat{m} = 0.04$ and $\hat{r} = 0.7$, U_{crit} =15 instead of 16. The numerical predictions of the transition between the intermittent and the rotational regimes differ from the experiments only for a NES of $\hat{m} = 0.08$ and $\hat{r} = 0.6$ and that of $\hat{m} = 0.04$ and $\hat{r} = 0.4$, U_{crit} =18 and 16.5 instead of 17 and 20, respectively.

The simulations predict the same behaviour observed in experiments. Increasing $\hat{m}$ from 0.02 to 0.04 and 0.08 at a constant $\hat{r} = 0.6$ expands the NES effective range and widens the range of the intermittent regime. While the decrease of $\hat{r}$ from 0.7 to 0.6 and 0.4 at a constant $\hat{m} = 0.04$ reduces the galloping amplitudes, expands the intermittent regime and delays the large-amplitude galloping.

5.3 Numerical results

In the current simulations, ode45 numerically integrates Eqs. 5.9 and 5.10 with a constant time step $\Delta\tau$ =0.01 and maximum simulation time $\tau_{max} = 3000$. The selected initial conditions $Y(0) = 0.5$, $\theta(0) = 0.1$, $\dot{Y}(0) = 0$ and $\dot{\theta}(0) = 0$, lead to zero initial energy of the NES. The characteristic non-dimensional amplitude $\hat{A}$ represents the maximum value of $Y(\tau > \tau_{max}/3)$ to avoid transient response. Our numerical model simulates the dynamics of the prism-NES system at incrementing reduced velocities $3.5 < U_r < 30$, substituting the initial displacement $Y(0)$ of the prism at each flow speed by the maximum amplitude $\hat{A}$ at the previous velocity.

5.3.1 NES Effect on galloping response of a prism

To assess how the NES of mass ratio $\hat{m}$=0.08 and a radius ratio $\hat{r}$=0.6 mitigates the prism galloping, we compared the prism non-dimensional amplitudes $\hat{A}$ with and without the NES in Figure 5.7 at different flow reduced velocities. We incremented the reduced flow velocity by a step of 0.5 starting from $U_r = 3.5$ up to 30, then decremented it back down with the same velocity step. In the direction of increasing flow speed, the prism amplitude without the NES starts to rise at the galloping onset speed $U_c = 11.5$, which we determined when the prism non-dimensional amplitude $\hat{A}$ reaches 0.1. Then, the prism response increases significantly and reaches a lower limit cycle up to a reduced flow velocity $U_r = 17.5$. Above this speed, the prism amplitude $\hat{A}$ grows linearly from 4.2 to reach 8.7 at $U_r = 30$. The NES affects the prism galloping response ; it increases the galloping onset speed U_c to 13.5 as compared to without NES 11.5. The prism amplitude with the NES does not exceed 0.6 in a wide range

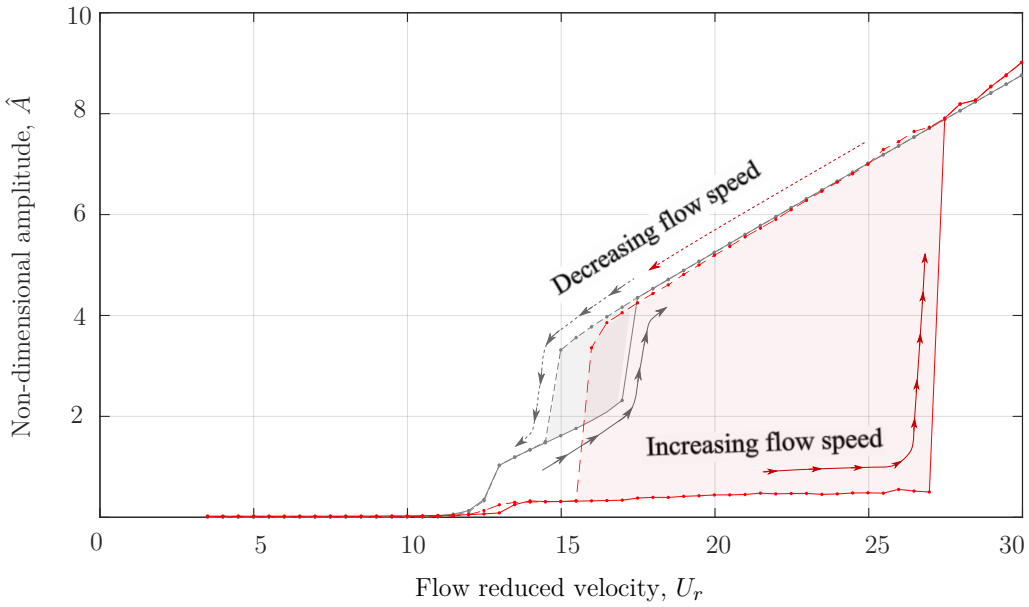

Figure 5.7 Numerical simulation of the prism responses with (red curves) and without a NES (gray curves), of a mass ratio $\hat{m}$=0.08, and a radius ratio $\hat{r}$=0.6, in the directions of increasing $U_r = 3.5 : 0.5 : 30$ (—) and decreasing flow velocity $U_r = 30 : -0.5 : 3.5$ (- - -).

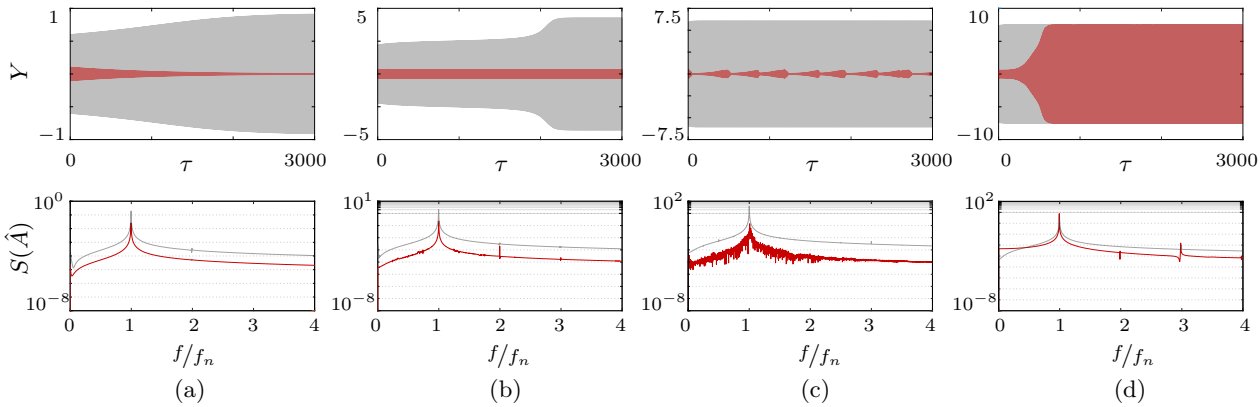

Figure 5.8 The time response and amplitude spectrum of the vibrating prism with (red curve) and without the NES (gray curve), of $\hat{m} = 0.08$ and $\hat{r} = 0.6$, at different flow reduced velocities $U_r =$: (a) 12.5, (b) 17.5, (c) 22.5, (d) 27.5. The frequency responses are presented on a semi-log scale.

of flow speeds $14 < U_r < 27$; which we termed as the NES effective range. At higher flow speeds, the NES is ineffective and may cause an increase in the prism amplitudes. For the prism without NES, we only observed two limit cycle branches between $14 < U_r < 17$. With the NES, the simulation predicts a larger velocity range with two branches $16 < U_r < 27$. For the upper branch (decreasing flow speeds), the NES has no considerable effect on the galloping amplitudes of the prism at high flow speeds $30 > U_r > 16$. At a reduced flow velocity $U_r = 15.5$, the NES can mitigate the prism galloping and reduces its non-dimensional amplitude $\hat{A}$ from 3.5 down to nearly 0.35. The NES maintains the prism amplitudes around this value for a range of lower speeds $15 > U_r > 13$ and kills the prism vibration at $U_r = 12$.

Galloping of the square prism considered here involves a hysteresis phenomenon over a range of flow speeds $14.5 < U_r < 17.5$, at which the prism response depends on the initial conditions. With increasing flow speed, the prism follows the lower limit cycle branch. The NES delays the galloping occurrence in this case to much higher flow speeds, mitigating the prism amplitudes in a wide range of flow speeds. With decreasing flow speed, the prism amplitude reaches the upper limit cycle due to the relatively large initial displacement of the prism. The NES is much less effective or ineffective in absorbing high-amplitude galloping of the upper branch. Since the NES behaviour depends on the excitation level, the NES is efficient to delay the occurrence of galloping but less effective in stabilizing a prism experiencing very large amplitude galloping.

To evaluate the NES influence on the prism response in the direction of increasing flow speed, we present the displacement time histories and the frequency responses of the prism with and without the NES at reduced flow velocities U_r of 12.5, 17.5, 22.5, and 27.5 (Figure 5.8). While the prism without NES starts to gallop at $U_r = 12.5$ (Figure 5.8a), increasing its non-dimensional displacement Y to 0.9, the prism-NES system is still stable exhibiting the same natural frequency. At $U_r = 17.5$ (Figure 5.8b), the NES limits the prism amplitude to $\hat{A} = 0.3$ in comparison to 4.2 for the prism without NES. At $U_r = 22.5$ (Figure 5.8c), adding the NES reduces the prism amplitude from $\hat{A} = 6$ to 0.5, resulting in a strongly modulated response of the prism. The NES does not change the natural frequency of the prism at $U_r = 17.5$ and $U_r = 22.5$. At a reduced flow velocity $U_r = 27.5$ (Figure 5.8d), the NES of mass ratio $\hat{m}$=0.08 is no longer effective in reducing the prism amplitudes. Generally, the NES delays the galloping occurrence and mitigates the prism amplitudes without affecting its natural frequency, even in the NES effective range. That is the main advantage of the NES compared to other vibration absorbers.

5.3.2 Different dynamics experienced by the NES

Since the NES behaviour depends on the excitation level, the change in the galloping force at each flow speed affects the NES dynamics. Based on the NES behaviour, we classify the prism-NES system dynamics into four regimes ; oscillatory, intermittent, rotational, and ineffective. The time histories of the prism displacement and the NES ball angular displacement and speed at reduced flow velocities $U_r = 12.5$, 15, 17.5, 25 and 27.5 exhibit the different dynamics of the system in the four regimes (Figure 5.9). Figure 5.9 a shows the selected points on the prism response curve and presents the NES regime mapping in the two cases of increasing and decreasing the flow velocity.

The *oscillatory regime* appears at low reduced flow velocities $U_r < 14$. Figs. 5.9 b presents the NES and the prism responses in this regime at $U_r = 12.5$: the ball oscillates slowly with a small angular displacement not exceeding 10^o, then stops in the 0° position. The ball angular speed does not exceed 2% of the prism natural frequency. Despite the small oscillations of the NES ball, the NES mitigates the prism amplitudes delaying the occurrence of high-amplitude galloping.

The *intermittent regime*, characterized by almost steady vibration of the prism (Figs. 5.9 c and 5.9d), appears as a transition regime existing within a small range of reduced flow velocities $14 < U_r < 18$. The ball oscillates back and forth with an amplitude close to 200° at the beginning of this regime $U_r = 15$. While, at the end of this regime $U_r = 17.5$, the ball behaviour changes to rotate in a few complete revolutions with a low non-dimensional angular speed $\dot{\theta} < 0.8$ and thus out of sync with the prism vibrating at a dimensionless frequency of 1. The NES maintains the prism galloping amplitudes $\hat{A}$ below 0.35 during the whole range of the intermittent regime.

In the *rotational regime* (Figure 5.9 e), the NES ball rotates continuously for more than 5 revolutions with higher angular speed $\dot{\theta}$ that fluctuates around 1, i.e., approximately equal to the prism frequency. The ball rotation directly reduces the galloping amplitudes from 0.5 to 0.05 before stopping. Then the prism amplitude grows again. This cycle of reduction and growing of the prism amplitude is repeated, resulting in a strongly modulated response of the vibrating prism.

At higher flow speeds $U_r \geq 27.5$, the *ineffective regime* (Figure 5.9 f) appears, in which the ball can not engage with the system frequency at high amplitude galloping. Thus, the ball rotates, alternating its directions with high angular speeds approaching 4 times the prism natural angular frequency. These fast rotations of the ball are insufficient to damp the prism motion. In the ineffective regime, the NES is no longer beneficial in mitigating the galloping

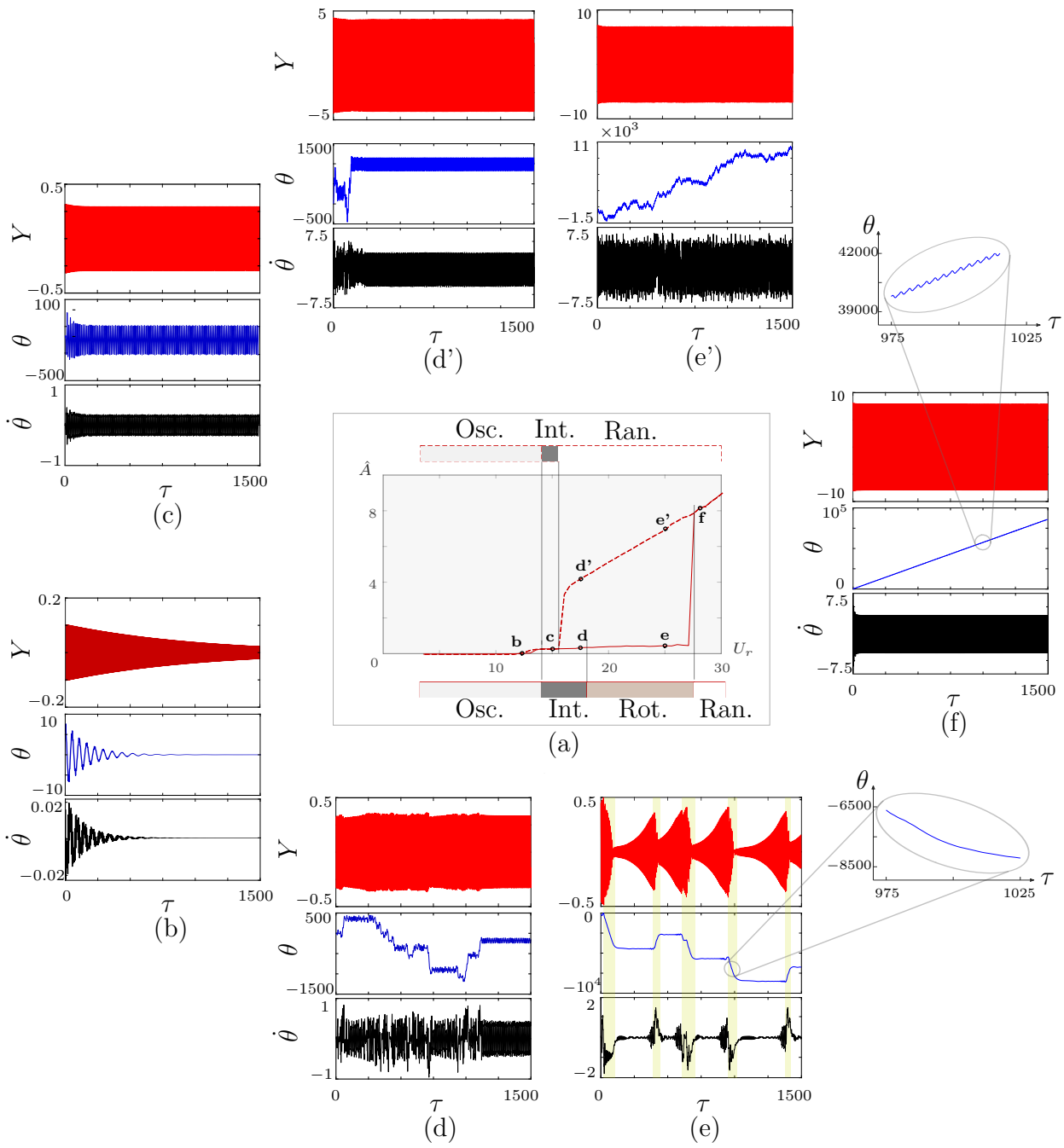

Figure 5.9 Time histories of the prism non-dimensional displacement Y (red curve), NES ball angular displacement θ in degrees (blue curve), and the the ball angular speed $\dot{\theta}$ (black curve) showing NES dynamics at various flow speeds. (b) Oscillatory, $U_r = 12.5$; (c, d) Intermittent, $U_r = 15$ and 17.5, respectively; (e) Rotational, $U_r = 25$; (f) ineffective regime, $U_r = 27.5$; (e' and d') are the NES different dynamics observed in case of slowing down the flow to $U_r = 17.5$ and 25, respectively. Only the interval $0 \leq \tau \leq 1500$ is shown.

amplitude at high flow speeds out of its effective range as the energy extracted by the vibrating prism from the airflow exceeds the energy dissipation rate of the NES.

Upon slowing down the flow from $U_r = 30$, the prism-NES system experiences an ineffective regime for $U_r \geq 27.5$. Then the system behaviour changes at $U_r = 25$ and 17.5 (Figs. 5.9 e' and d', respectively). The NES ball experiences ineffective rotation at $U_r = 25$, which changes to large oscillations at 17.5 with no damping effect on the prism amplitudes. At $U_r < 16$, the NES can damp the galloping of the prism, reducing its non-dimensional amplitude from $\hat{A} = 3.8$ to 0.3 (Figs. 5.9 a). We observe the NES intermittent response when slowing down the flow in a narrow range of reduced flow speeds $14 < U_r < 16$. While, the oscillatory regime appears at the same flow speed range $U_r < 14$, comparing to the case of accelerating flow.

We confirm that the NES response depends on the excitation level of the primary system. In the oscillatory regime, the kinetic energy consumed to oscillate the NES ball with small oscillations is enough to absorb the energy extracted from the flow by the prism at low flow speeds and delay the galloping occurrence. When the energy extracted by the prism from the air stream increases at higher flow speeds, the balls rotates fast in the intermittent regime and faster in the rotational regime to absorb the prism energy. According to the targeted energy transfer TET mechanism in the prism-NES system, the rotational regime is the most efficient. The NES ball engages with the prism dynamics and rotates with the prism natural frequency in a so-called 1:1 resonance capture phenomenon. That leads to the strongly modulated response of the prism illustrating the nonlinear energy transfer in the prism-NES system. At higher flow velocities, the energy of the prism exceeds the maximum energy absorbed by a ball rotating with the prism natural frequency, which we define as the capacity of the NES. Thus, the ball rotation is ineffective and can not mitigate the galloping amplitudes.

5.4 Analytical estimations

In this section, we analytically determine the boundary between the NES oscillatory and intermittent regimes by modelling the primary mass as a parametric excitation for the NES. Additionally, a proposed power flow analysis estimates the limit of the NES working range and explains the dynamics of the NES in the rotational regime.

5.4.1 Parametric excitations

Based on the method presented by Gentelman [118], we qualitatively distinguishes between NES different regimes by examining the behaviour of the NES ball from the perspective of a

parametric excitation. Assuming a sinusoidal motion for the prism, and substituting in the equation of motion of the rotating ball, equation 5.10, we obtain :

$$Y = Y_0 \, cos\, \tau, \tag{5.11}$$

$$\ddot{\theta} + 2\zeta_\theta \, \dot{\theta} - \frac{Y_0}{\hat{r}} \, cos\, \tau \sin\theta = 0. \tag{5.12}$$

By setting $\ddot{\theta} = \dot{\theta} = 0$, we obtain the equilibrium points at $\theta = 0, \pi$. The oscillatory regime is characterized by the ball's small oscillations around these points at which $sin\theta \simeq \theta$. By substituting in equation 5.12, we obtain a particular case of the damped Mathieu equation, $\ddot{\theta} + \lambda \, \dot{\theta} - (\delta + \eta \, cos\, \tau) \, \theta = 0$ [160].

$$\ddot{\theta} + 2\zeta_\theta \, \dot{\theta} - \frac{Y_0}{\hat{r}} \, \theta \, cos\, \tau = 0, \tag{5.13}$$

where here $\lambda = 2\zeta_\theta, \ \delta = 0$, and $\eta = -\dfrac{Y_0}{\hat{r}}$.

In the previous section, we characterize the oscillatory regime a one with small ball oscillations. Thus, the stability analysis of equation 5.13 can determine the transition boundary from the oscillatory regime to the intermittent regime ; stable equilibrium points indicate the oscillatory regime, while the unstable ones refers to the intermittent regime. The Ince-Strutt diagram representing a stability chart for the Mathieu equation defines the boundaries of parametric instability of equation 5.9. Based on the expression developed by Kovacic et al. [161] for the boundary of the Ince-Strutt diagram in the case with linear damping ($\eta_{crit} = \frac{1}{2}\sqrt{1 + 4\lambda^2}$), we can estimate the critical amplitude corresponding to the transition from the oscillatory to the intermittent regime, i.e,

$$Y_{0_{crit}} = \hat{r} \sqrt{\frac{1}{4} + 4\zeta_\theta^2}, \tag{5.14}$$

where ζ_θ is the ball damping for small oscillations at low angular speed, $= c/2m_b r^2 \, \omega$.

5.4.2 Power flow analysis

Numerical results exhibited four different responses for the NES depending on the excitation level. Tracking the energy transfer by the fundamental principles of power flow can explain some critical dynamics for the prism-NES integrated system. We define the non-dimensional power terms of the external and the internal forces affecting our system as the scalar product of the velocity with a given force component : the fluid load power P_{Fy}, the power of the

damping force of the support P_d, and the power P_{tr} transferred by the NES track reaction on the ball. Besides, terms representing the change in the prism potential energy $\Delta\bar{E}_p$ as well as the kinetic energy change due to translation $\Delta\bar{E}_{k_{tran}}$ and rotation $\Delta\bar{E}_{k_{rot}}$ are presented. We multiply Eqs. 5.9 and 5.10 by $\dot{Y}$ and $\dot{\theta}$ respectively and integrate over a period T to find

$$\begin{aligned}\underbrace{\frac{1}{T}\int_0^T \frac{\mathrm{d}}{\mathrm{d}\tau}\left[\frac{1}{2}\dot{Y}^2\right]\mathrm{d}\tau}_{\Delta\bar{E}_{k_{tran}}} + \underbrace{\frac{1}{T}\int_0^T \frac{\mathrm{d}}{\mathrm{d}\tau}\left[\frac{1}{2}Y^2\right]\mathrm{d}\tau}_{\Delta\bar{E}_p} \\ = \underbrace{\frac{1}{T}\int_0^T \frac{U_r^2}{2m^*}C_y\,\dot{Y}\,d\tau}_{\bar{P}_{Fy}} - \underbrace{\frac{1}{T}\int_0^T 2\zeta_y\dot{Y}^2\,d\tau}_{\bar{P}_d} - \underbrace{\frac{1}{T}\int_0^T \hat{r}\,\hat{m}\left(\ddot{\theta}\sin\theta+\dot{\theta}^2\cos\theta\right)\dot{Y}d\tau}_{\bar{P}_{tr}},\end{aligned} \tag{5.15}$$

$$\frac{1}{T}\int_0^T \hat{m}\hat{r}^2\ddot{\theta}\dot{\theta}d\tau = \frac{1}{T}\int_0^T -2\,\hat{m}\,\hat{r}\,\zeta_\theta\,\dot{\theta}^2\,d\tau - \frac{1}{T}\int_0^T \hat{m}\,\hat{r}\,\ddot{Y}\,\sin\theta\,\dot{\theta}d\tau, \tag{5.16}$$

We integrate by part the last term of Eq. 5.16 and rearrange to get

$$\begin{aligned}\underbrace{\frac{1}{T}\int_0^T d\left(\frac{1}{2}\hat{m}\hat{r}^2\dot{\theta}^2\right) + \frac{1}{T}\left[\hat{m}\hat{r}\dot{Y}\sin\theta\dot{\theta}\right]_0^T}_{\Delta\bar{E}_{k_{rot}}} \\ = -\underbrace{\frac{1}{T}\int_0^T 2\hat{m}\hat{r}^2\zeta_\theta\dot{\theta}^2 d\tau}_{\bar{P}_{dis}} + \underbrace{\frac{1}{T}\int_0^T \hat{m}\hat{r}\left(\ddot{\theta}\sin\theta+\dot{\theta}^2\cos\theta\right)\dot{Y}d\tau}_{\bar{P}_{tr}}.\end{aligned} \tag{5.17}$$

The input power into the prism-NES integrated system P_{in} and the power transferred to the NES P_{tr} are important parameters informing about the NES effectiveness. The initial stage of the prism response without the NES damping effect represents the NES excitation form. By describing the prism displacement in a sinusoidal form (Eq. 5.11), we estimate $\bar{P_{in}}$ as follow.

$$\begin{aligned}\bar{P}_{in} = \bar{P}_{Fy} + \bar{P}_d \\ = \frac{U_r^3}{4m^*}\left[A_1\left(\frac{Y_0}{U_r}\right)^2 + \frac{3}{4}A_2\left(\frac{Y_0}{U_r}\right)^4 + \frac{5}{8}A_3\left(\frac{Y_0}{U_r}\right)^6 + \frac{35}{64}A_4\left(\frac{Y_0}{U_r}\right)^8\right] - Y_0^2\,\zeta_y,\end{aligned} \tag{5.18}$$

where $A_1,\ A_2,\ A_3$ and A_4 are the constants of the C_y polynomial fitting presented in Eq. 5.3. To assess the NES effective range, we compare the averaged value of the input power $\bar{P_{in}}$ with the NES power capacity. Since the rotational mode represents the most efficient regime in terms of power absorption, at which the ball exhibits a 1:1 resonance capture with the vibrating prism, we estimate the NES maximum power capacity at the rotational regime $\bar{P}_{rot}$ assuming $\dot{\theta}_{rot} = 1$ and $\theta_{rot} = \tau + \phi$, where ϕ is the phase difference that achieves the

maximum transfer rate of energy, which we solved numerically as 0. By substituting Eq. 5.11 in the transferred power term presented in Eq.5.17, $\bar{P}_{rot}$ can be expressed as

$$\bar{P}_{rot} = \frac{1}{2\pi}\int_0^{2\pi} \hat{m}\hat{r}\left(\ddot{\theta}\sin\theta + \dot{\theta}^2\cos\theta\right)\dot{Y}d\tau = \frac{1}{2}\hat{m}\hat{r}Y_0. \tag{5.19}$$

Comparing the NES maximum power capacity $\bar{P}_{rot}$ with the input power $\bar{P}_{in}$ at various flow speeds provides an estimation for the critical reduced flow velocity, at which the NES is no longer effective in absorbing the energy of the galloping prism. Figure 5.10 presents the input power at reduced flow velocities U_r = 23, 24, 24.5, and 25 with the NES maximum power capacity. Since a higher flow speed pumps more energy into the prism-NES system, the input power curve approaches that of the NES capacity by increasing U_r. The intersection between the $\bar{P}_{in}$ and $\bar{P}_{rot}$ curves, observed at $U_r = 24.5$, indicates that the NES can absorb the input power when it works with its maximum capacity. This defines the critical speed U_{crit} representing the limit of the NES working range, beyond which the input power will exceed the NES maximum capacity as occurs at $U_r = 25$. Gathering the intersection points of $\bar{P}_{rot}$ curve with $\bar{P}_{in}$ curves at various flow velocities leads to the predicted limit of successful energy transfer presented in Figure 5.10b.

In the perspective of the NES, the transferred power $\bar{P}_{tr}$ is the power gained by the NES, and the power dissipated by ball friction $\bar{P}_{dis}$ is the power consumed. Consequently, comparing these two values during the ball rotational response ($\dot{\theta}_{rot} = 1$, $\theta_{rot} = \tau$) can explain the ball behaviour, i.e.,

$$\bar{P}_{tr} = \bar{P}_{rot} = \frac{1}{2}\hat{m}\hat{r}Y_0, \tag{5.20}$$

$$\bar{P}_{dis} = \frac{1}{2\pi}\int_0^{2\pi} 2\hat{m}\hat{r}^2\zeta_\theta\dot{\theta}^2 d\tau = 2\hat{m}\hat{r}^2\zeta_\theta. \tag{5.21}$$

As long as $\bar{P}_{tr} \geq \bar{P}_{dis}$, the ball can sustain its rotation to dissipate power until $\bar{P}_{dis}$ reaches the value of the power in the NES $\bar{P}_{tr}$. When $\bar{P}_{dis}$ exceeds $\bar{P}_{tr}$, the ball stops rotating. From this comparison, we can get an inequation giving us a minimal limit on the prism amplitude that can sustain the ball :

$$Y_0 \geq 4\hat{r}\zeta_\theta. \tag{5.22}$$

For a NES of $\hat{m} = 0.08$ and $\hat{r} = 0.6$ as considered here, $4\hat{r}\zeta_\theta = 0.147$. Figure 5.11 presents the amplitude limit $\hat{A}_{min}$ below which the ball rotational response is impossible. We defined $\hat{A}_{min}$ as the minimum prism amplitude observed in each of the periodic cycles of the rotational regime, presented by blue and black points in Figure 5.11a. Estimated values of $\hat{A}_{min}$ obtained from simulations at different flow speeds are almost all below the amplitude limit $\hat{A}_{min} = 0.147$ derived analytically (Figure 5.11b). The rotational regime is a competition between

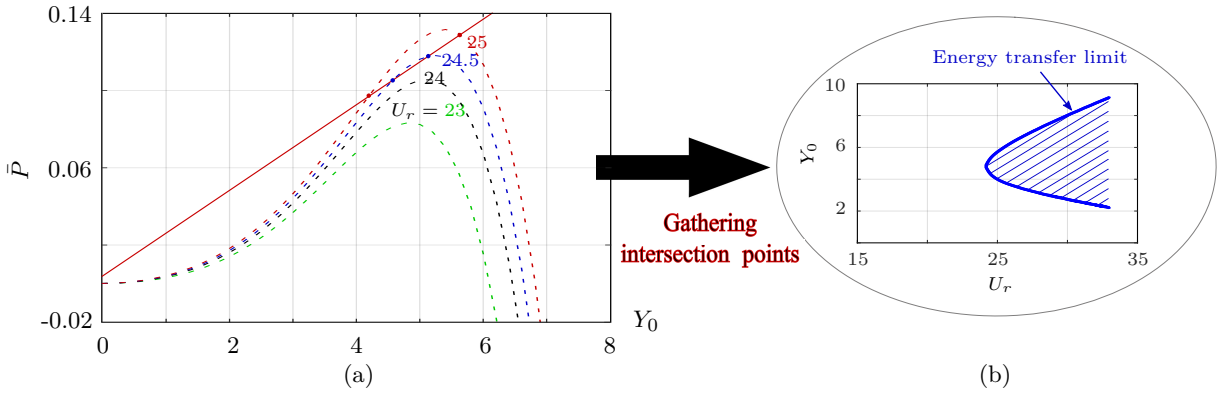

Figure 5.10 The limit of successful energy transfer obtained by (a) comparing the NES maximum power capacity at the rotational regime $\bar{P}_{rot}$ (—) with the input power $\bar{P}_{in}$ at various reduced flow velocities : $U_r = 23$ (- - -), $U_r = 24$ (- - -), $U_r = 24.5$ (- - -), $U_r = 25$ (- - -). All the averaged-power terms are plotted *versus* the assumed prism amplitude Y_0. (b) Energy transfer limit obtained from the intersection of $\bar{P}_{rot}$ and $\bar{P}_{in}$ *versus* U_r.

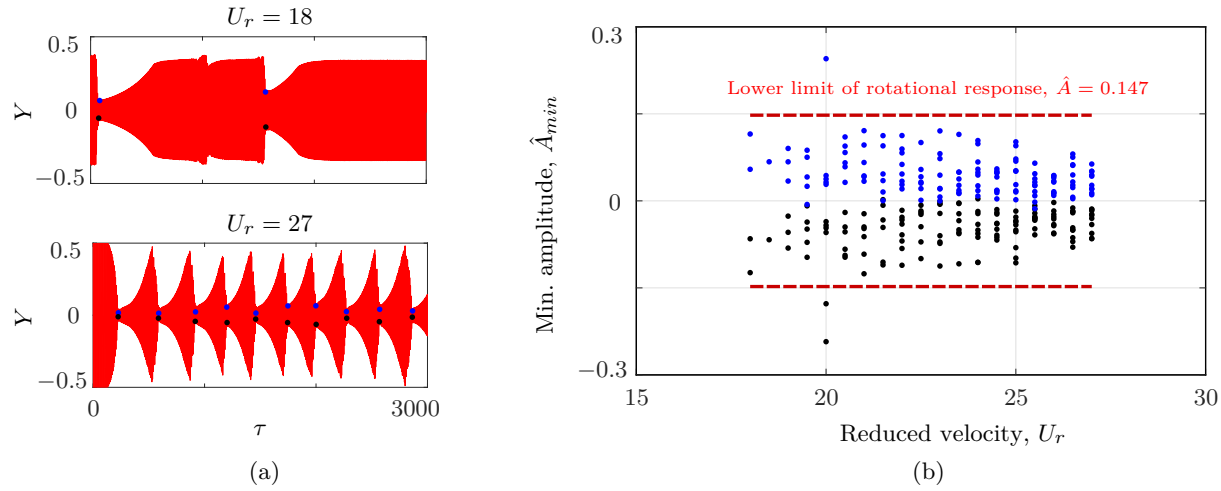

Figure 5.11 The limit of the ball rotational response : (a) time histories of the prism non-dimensional displacements $Y(\tau)$ at the beginning ($U_r = 18$) and the end ($U_r = 27$) of the NES rotational regime presenting the minimum amplitudes $\hat{A}_{min}$ in the $+y$ (•) and $-y$ (•) directions. (b) comparing $\hat{A}_{min}$ estimated by simulations at different flow velocities U_r with the analytical limit $\hat{A}_{min} = 0.147$ provided by Eq. 5.21 (---).

the ability of the system to transmit energy from the prism to the ball, and the capacity of the ball to dissipate energy. The prism accumulates energy from the wind over multiple cycles until the ball is excited, at which point it spins and dissipates energy until the prism amplitude is too small to sustain the motion. This gives rise to the modulated response of the rotating regime (Figure 5.9e).

5.4.3 Regime Boundaries

Figure 5.12 presents analytical estimations of the boundaries between the NES regimes. Considering the ball in the NES as a parametric excitation problem allows predicting the maximum amplitude below which the oscillatory regime is possible, Eq. 5.14. This limit is traced as a horizontal red line in Figure 5.12. It accurately separates observations of the oscillatory and intermittent regimes, be they experimental or numerical. We can interpret that above a certain amplitude of motion of the prism, the ball undergoes a form of parametric instability and oscillates with great amplitude.

From the power analysis, we can compare the power that can be extracted from the flow by the prism (minus its structural damping) with the maximum energy the ball could dissipate in ideal 1:1 resonance capture where it rotates with a practically constant angular velocity $\dot{\theta} = 1$. From this reasoning, we obtain the energy transfer limit curve in blue in Figure 5.12. This forms a theoretical limit to the region of effectiveness of the NES. Any imperfection in the functioning of the NES would move this curve to the left as well as make it expand faster. This simple analytical expression found where Eqs.5.18-5.19 intersect provides a reasonable limit and sheds light on the functioning of the ball-in-track NES for mitigating galloping.

5.5 Conclusion

The ball-in-track (BIT) NES presented in the literature is a purely rotative NES designed to mitigate the galloping of a square prism in wind tunnel tests. Nevertheless, the limitation in the maximum amplitude of the setup restricted the experiments to a definite range of flow speeds.

The current research proposes a numerical model employing experimental data of the galloping force C_y and the ball damping c_θ coefficients as inputs for simulating the dynamics of the prism-NES system. Static experiments provided a fitting for the galloping force coefficient C_y as a function of the square prism angle of attack α after eliminating systematic errors using the KolmogorovSmirnov (K-S) test. We developed a new method to estimate the ball damping coefficient c_θ through free rotation tests. The experiments provide a critical

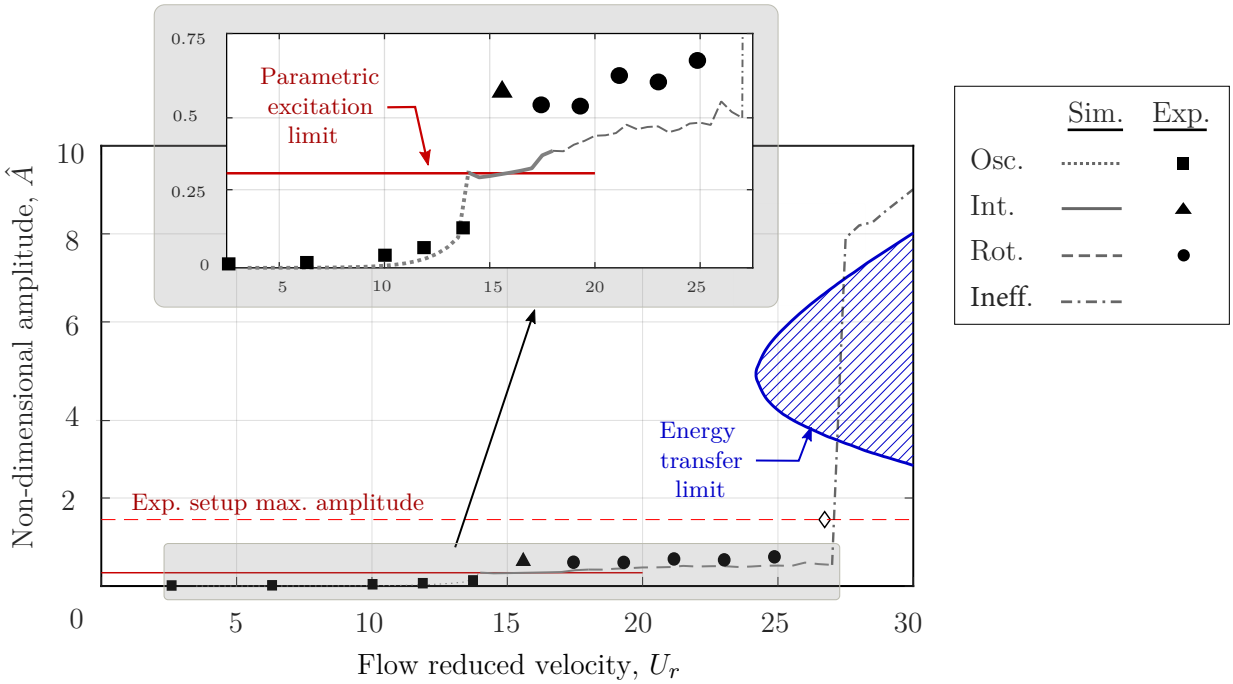

Figure 5.12 Physical interruption of our simulation for the prism response with a NES of $\hat{m} = 0.08$ and $\hat{r} = 0.6$, with experimental results [158] and analytical estimations (— parametric excitation limit coinciding with the transition between the oscillatory and the intermittent regimes, — the limit of successful energy transfer). The amplitude limitation of the setup is presented by $\diamond$.

angular speed, beyond which the ball damping automatically grows due to its contact with both the NES track sidewall and floor. The damping variation is a particular advantage of the BIT-NES; small damping at low angular speeds facilitates the ball's rotation, while relatively large damping allows the ball to absorb more energy at high angular velocities. The simulations exhibit four different responses for the NES ball; oscillatory, intermittent, rotational and ineffective. The oscillatory response of the ball appears at low flow speeds $U_r < 14$. Within a small range of reduced flow velocities $14 < U_r < 18$, we observe the intermittent regime at which the ball completes a few revolutions with low angular speeds $\dot{\theta} < 0.8$. The rotational response seen at higher flow speeds $18 < U_r < 27.5$ is the most efficient regime in terms of energy absorption. In this regime, the NES ball rotates continuously for more than five revolutions, during which it engages with the prism dynamics showing 1:1 resonance capture. Above a critical flow speed $U_r > 27.5$, the ball experiences an ineffective response with varying speed, and the NES becomes ineffective in reducing galloping amplitudes.

Under a large perturbation or highly energetic initial conditions, the NES can be ineffective in mitigating galloping as the prism vibrates on the upper branch limit cycle. Moreover,

the current study provides analytical estimations of the boundaries between NES regimes. Considering the prism mass as a parametric excitation for the NES ball predicts the prism maximum amplitude coinciding with the limit boundary of the oscillatory regime. The proposed power flow analysis across the integrated system of a prism with a BIT-NES of $\hat{m} = 0.08$ and $\hat{r} = 0.6$ leads to an analytical prediction for the limit of the NES effective range as $U_r = 24.5$. Power flow analysis in the perspective of the BIT-NES explains the ball dynamics at the rotational regime, pointing out a value of prism amplitude $\hat{A}_{min} \geq 4\hat{r}\zeta_\theta$ below which the ball rotation stops.

The realistic simulation of the prism-NES dynamics at high flow speeds with the analytical predictions of the NES effective range can help in optimizing the BIT-NES design according to the given parameters of a primary system. That also may extend the practical implementation of such NESs to mitigate vibrations of high rising engineering structures.

CHAPTER 6 ARTICLE 3: MULTIPLE BALLS ROTATING IN A CIRCULAR TRACK EXPERIMENTALLY MITIGATE THE GALLOPING OF A SQUARE PRISM

Michael M.Selwanis, Guilherme R.Franzini, Cédric Béguin, and Frédérick P.Gosselin

This chapter represents the third article, submitted to "Journal of sound and vibration" in November 2021.

Abstract

Galloping is a destructive type of flow-induced vibration (FIV) affecting engineering structures subjected to wind. In this paper, we introduce a simple, low-cost device able to passively absorb the energy of vibrating structures and reduce the galloping amplitudes. This purely nonlinear energy sink (NES) consists of multiple balls rotating freely in a circular track without direct mechanical coupling with the primary system. We assess the benefit of the proposed NES in mitigating the galloping of a square prism through wind tunnel tests and explain the main factors affecting its behaviour. The NES balls rotate due to dynamic interaction with the prism exhibiting a way of nonlinear energy absorption, which is enhanced by ball collisions. We test different NES configurations varying the number of NES balls to highlight the number of balls' effect on shifting the mass centre and changing the dynamics of the NES. Whereas a single ball NES with a mass 8% that of the prism can delay the critical reduced velocity by 68%, a 2 or 3-ball NES of equivalent mass delays this speed by 87%.

Keywords : Non-linear energy sink (NES), Multi-ball NES, Vibration suppression, Square prism, Galloping, Energy transfer, and Wind tunnel tests.

6.1 Introduction

Transverse galloping generated during heavy winds can lead to natural disasters putting bridges and skyscrapers at risk. A linear tuned mass damper (TMD) is a simple solution for damping the vibration of high buildings. However, it works only in a narrow frequency band and changes the characteristics of the primary system, adding new frequencies. Under the class of nonlinear stiffness absorbers, nonlinear energy sinks (NES) overcome the drawbacks of the TMD. A typical NES consists of an auxiliary mass coupled to the primary system through

inertia or by a spring element of non-linearizable stiffness and proper damping properties. The absence of linear stiffness enables such absorbers to engage with the dynamics of the primary structure, mitigating its vibration amplitudes over a wide band of frequencies [162].

Several NES designs have been proposed. The first one is the translative NES that only makes a translational motion and comes in many configurations; the grounded configuration with an auxiliary mass that is linked by springs to the primary structure and stationary ground, the ungrounded configuration, the NES with limited amplitude [16], the bistable NES [94], and the multi-DOF NES that consists of several masses. The second type is the rotative NES, where a rigid arm attaches a tip mass free to rotate [19] ; and which can also combine radial motion in the elastic rotative NES [145]. Another type with no spring elements known as the track NES [115] is based on a racetrack to restrict the motion of the auxillary mass for the indirect coupling with the primary structure. The track shape defines smooth impact-free restoring force.

NESs rely on different mechanisms to absorb energy from a vibrating primary structure. The combination of more than one of these mechanisms in a NES increases its suppression efficiency. The Vibro-impact NES, for example, combines the advantages of both a typical NES and an impact damper [21]. The momentum transfer due to the impacts of the auxiliary mass with a rigid wall in such a NES enhances its suppression effect compared to a traditional NES. Recently, a Vibro-impact track NES [24] was proposed as a modified version of a track NES with a rigid wall on one side to limit the motion of the NES mass, using the impacts to improve the energy transfer. A bistable track NES [25] combines the advantages of both the bistable NES and the track NES representing an efficient and practical NES of two stable equilibrium points.

A purely rotative NES, composed of a ball free to rotate in a circular track without any direct link with the primary structure, was a considerable simplification in the NES design [158]. Instead of that, this work combines the advantages of rotative and impact NESs. Here, we introduce a multi-ball NES as a novel contribution relying on inertial coupling with enhanced suppression efficiency due to the impact between balls. The current study is an experimental evaluation of the multi-ball NES capability to mitigate the galloping of a square prism. As presented in Figure 5.1, we propose a purely rotative NES composed of multiple balls free to rotate in a circular track without direct coupling to the prism. The paper is organised into four sections. Following the introduction, section 6.2 presents the experimental setup and the construction of the proposed NES. In section 6.3, We explain the concept of the multi-ball NES, highlighting the main parameters that affect on its behaviour. Section 6.4 demonstrates the results comparing the suppression efficiency of different configurations of

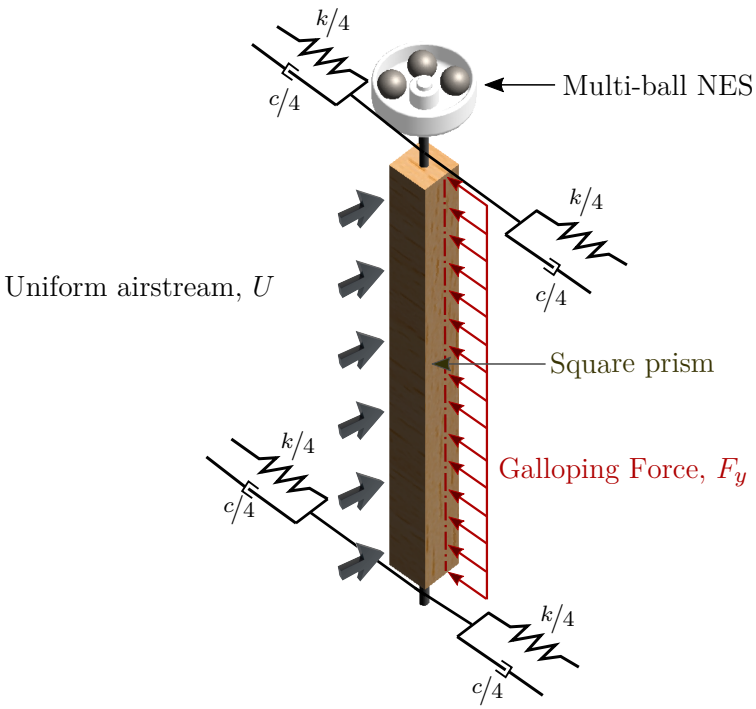

Figure 6.1 Three-dimensional drawing of the proposed NES coupled with a square prism model.

the multi-ball NES. Conclusions are brought in section 6.5.

6.2 Methodology

We follow a similar methodology used for testing the single ball-in-track NES of Ref. [158], performing the experiments in the closed-loop wind tunnel (Model 407-B, ELD, Lake City, MN, USA) of the mechanical engineering department of Polytechnique Montréal. The schematic of our model (Figure 4.2) presents a square prism of side length D vibrating with a single solid-body degree of freedom of displacement y transverse to a free stream of velocity U. The prism is spring mounted with an equivalent stiffness k, and a damping coefficient c. The balls in the NES are free to rotate in a circular track of mean radius r. The ball angular displacement θ_i is positive counter-clockwise, where the NES balls are numbered 1, 2, ... i ... N. The friction of each ball rotating in the track is modeled with a damping coefficient c_θ. For easier generalization, we define the following dimensionless parameters : the non-dimensional vibration displacement $\hat{Y} = y/D$ and amplitude $\hat{A} = A/D$; the damping ratio $\zeta_y = c/2m_t\omega$; the NES mass ratio $\hat{m} = \sum m_i/M$ and radius ratio $\hat{r} = r/D$; and the reduced flow velocity

$U_r = U/\omega D$, where m_t is the summation of the vibrating mass (M) and the balls' mass ($\sum m_i$), and ω is the angular natural frequency of the primary system.

Figure 6.3 (a) presents the experimental set up in detail : a lightweight model of a square prism of 5 cm side length and 58 cm height is mounted on two identical elastic supports, located above and under the wind tunnel test section. We installed a pair of plates at the two ends of the square prism to prevent the escape of airflow from the wind tunnel test section. Two smaller plates were installed 8 cm away from each end to help approach two-dimensional flow conditions. Our experimental setup allows a maximum amplitude A of 7.5 cm ($\hat{A} = 1.5$). The proposed multi-ball NES, shown in Figure 6.3 (b), consists of the main body (1), various size bushings (2), and steel balls (3). We printed the main body and the bushings using a 3D printer with white Poly-Lactic Acid (PLA) plastic. Swapping some parts allows to easily change the dimension of the NES track to accommodate different ball sizes. To assess the effect of the ball number variation on the NES behaviour, we tested several configurations of multi-ball NES of an equivalent mass.

A high-speed Camera (Motion BLITZ Cube 4, MIKROTRON) recorded the motion of the vibrating prism as well as the balls' positions with a resolution of 0.085 mm. A MATLAB code, developed for image analysis, traces the time histories of the prism vibration displacement y. We repeated the measurement at various flow speeds to capture the prism response by plotting the maximum amplitude A *versus* flow speed U.

6.3 The concept and the main parameters of the multi-ball NES

The mass distribution of balls and the collisions between them significantly affect the behaviour of the multi-ball NES. Thus, we highlight two leading parameters in the design of the multi-ball NES : the theoretical maximum radius of the NES mass centre $\rho_{c.max}$ and the NES track crowdedness ratio γ_t, which indicates the track portion filled with balls. The maximum

Table 6.1 Parameters of the experimental model.

Cross-section side length, D	5 cm
Prism length, L	58 cm
Limitation of the experimental setup	7.5 cm
Equivalent stiffness, k	360 N/m
Structural damping ratio, ζ_y	0.01
Mass ratio with reference to air-flow, $m^* = {m_t}/{\rho L D^2}$	859
NES mass ratio, $\hat{m} = \sum m_i/M$	0.079 ± 0.002
NES radius ratio, $\hat{r} = {r}/{D}$	0.5 ± 0.001

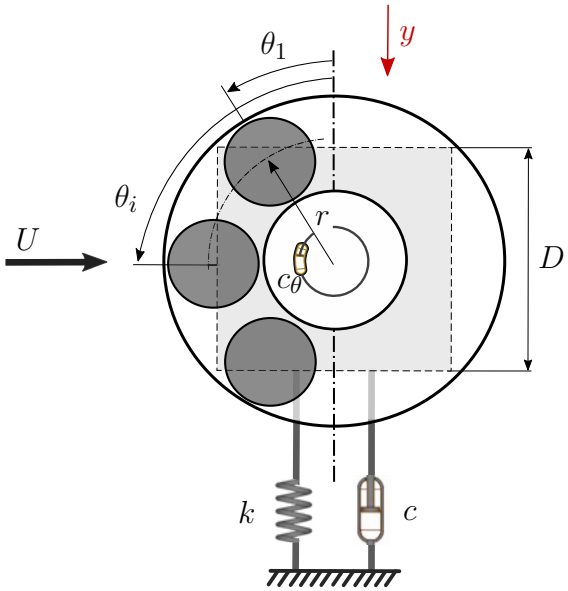

Figure 6.2 Schematic drawing of the square prism with the multi-ball NES.

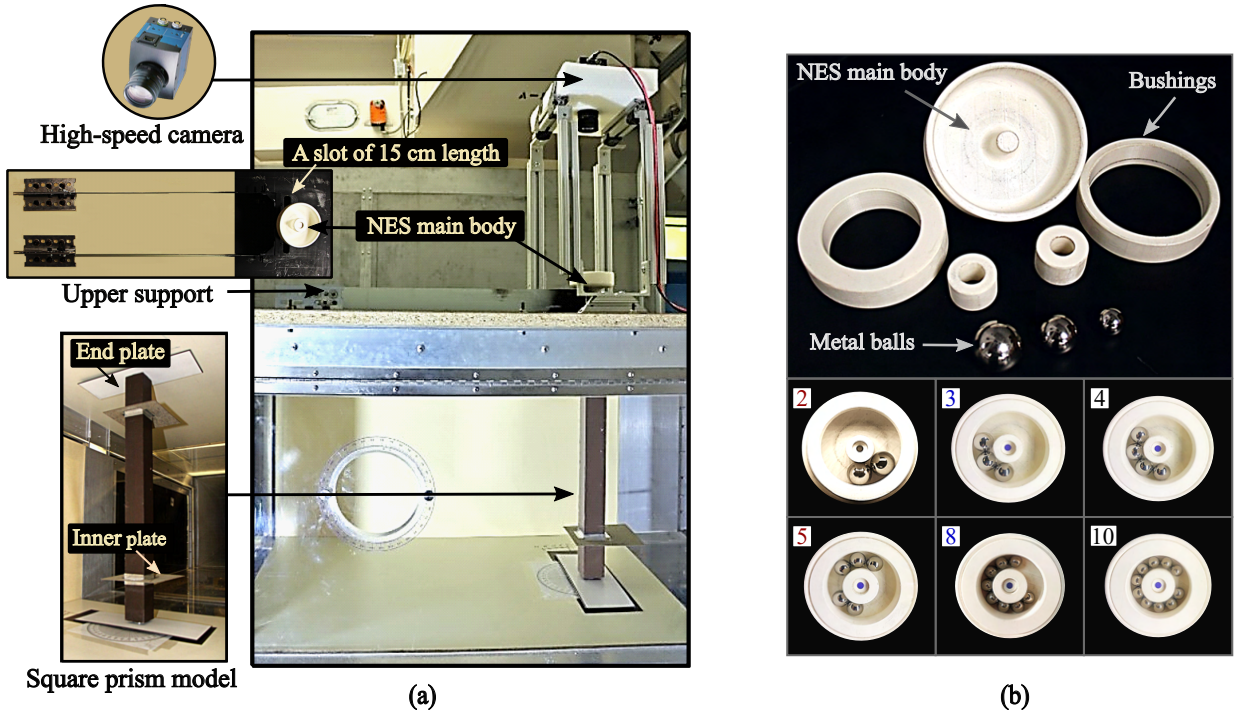

Figure 6.3 (a) Experimental setup. (b) Exploded view for NES parts and different configurations of the multi-ball NES of equivalent mass.

radius of the NES mass centre $\rho_{c.max}$ is estimated considering all the balls touching each other. This forms a theoretical maximum limit as any spacing between the balls decreases the radial position of the NES mass centre. We define the arc angle between the two tangents of a ball passing by the NES centre as φ (Figure 6.4 a), where

$$\frac{\varphi}{2} = tan^{-1}(\frac{r_b}{r}). \tag{6.1}$$

The arc angle leads to analytical estimates of the maximum radius of the NES mass centre $\rho_{c.max}$ and the NES track crowdedness ratio γ_t (Figure 6.4).

$$\rho_{c.max} = \frac{\sum_n^{i=1} \rho_i}{n}, \qquad \gamma_t = \frac{n\varphi}{360}, \tag{6.2}$$

where for an odd number of balls

$$\rho_1 = r, \quad \rho_{2,3} = r\cos\varphi, \quad \rho_{4,5} = r\cos 2\varphi, \quad \rho_{6,7} = r\cos 3\varphi, ... \tag{6.3}$$

And for an even number of balls

$$\rho_{1,2} = r\cos\frac{\varphi}{2}, \quad \rho_{3,4} = r\cos\frac{3\varphi}{2}, \quad \rho_{5,6} = r\cos\frac{5\varphi}{2}, \quad \rho_{7,8} = r\cos\frac{7\varphi}{2}, \quad \rho_{9,10} = r\cos\frac{9\varphi}{2}, ... \tag{6.4}$$

Table 6.2 presents the ball radius r_b, the arc angle φ, the maximum radius of the NES mass centre $\rho_{c.max}$ and the NES track crowdedness ratio γ_t for tested configurations of the multi-ball NES. Increasing the number of balls decreases $\rho_{c.max}$ and increases γ. Since the decrease in the radius ratio $\hat{r}$ of the 1-ball NES from 0.7 to 0.4 improved its suppression efficiency [158], we expect that decreasing $\rho_{c.max}$ in the multi-ball NES is favourable unless it is too small to sustain the dynamical coupling between the prism and the NES. Regarding the NES track crowdedness, more collisions occur for a higher number of balls, but they are

Table 6.2 Multi-ball NES tested configurations of equivalent $\hat{m} = 0.08$ and $\hat{r} = 0.5$.

ball no.	r_b [mm]	φ [°]	$\rho_{c.max}$	γ_t
10	5.00	31.28	3.71	0.87
8	4.00	33.40	7.88	0.74
5	2.50	38.50	15.07	0.53
4	2.00	41.71	17.44	0.46
3	1.50	44.86	20.15	0.37
2	1.00	51.28	22.54	0.28
1	0.50	62.20	25.00	0.17

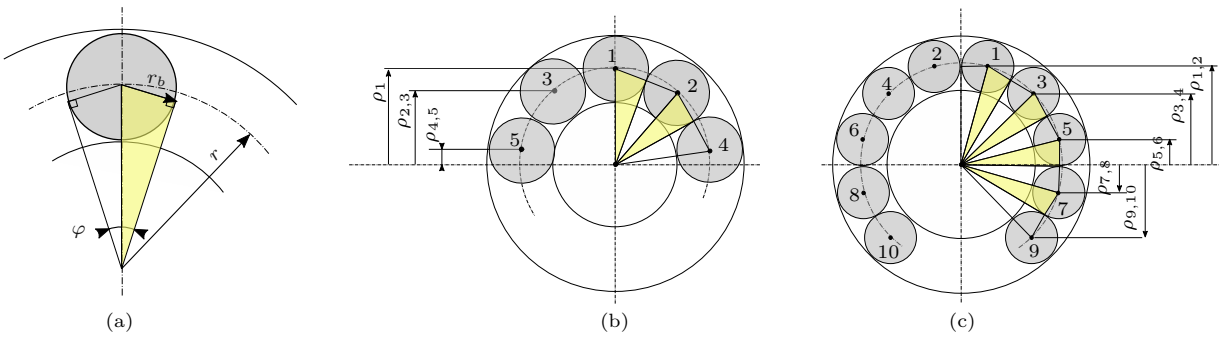

Figure 6.4 Estimating the main parameters of the multi-ball NES : (a) the arc angle φ, (b, c) the mass centre radius of odd and even numbers of balls.

less effective due to the increased γ_t that limits the mean free path of each ball. The energy consumed due to ball impacts is the summation of the kinetic energy loss of each collision. Thus, we can expect that there exists an optimal γ_t that lead to the maximum benefit of ball impacts.

6.4 Experimental results

Theăfindings of the current study are divided into two parts : assessing the effect of various multi-ball NES configurations on the prism galloping response, and understanding the dynamics of the multi-ball NES.

6.4.1 NES damping effect on galloping response

The NES can reduce the vibration amplitude of the prism in a range of flow speeds termed as the NES working range. Figure 6.5 a compares the responses of the prism without a NES, with 1 ball, 2 balls, 3 balls and 4 balls at different flow speeds. All tested NES configurations are successful in delaying the occurrence of large amplitude galloping to higher reduced velocities and maintaining vibration amplitudes below 0.5. Using two balls instead of one significantly reduces the prism vibration amplitude and eliminates the amplitude jump which appears between reduced velocities of 15 and 16. The working range of the 2-ball NES increases to $U_r = 30.2$ as compared to 26.7 for the 1-ball NES. Increasing the number of balls to three then four, reduces the vibration amplitudes of the prism at $U_r \geq 21.1$ with no effect on the NES working range. However, the prism amplitude with the 2-ball NES is smaller than that with the 3-ball or the 4-ball NESs at $U_r = 19.3$. At U_r between 13.8 and 15.6, we can observe

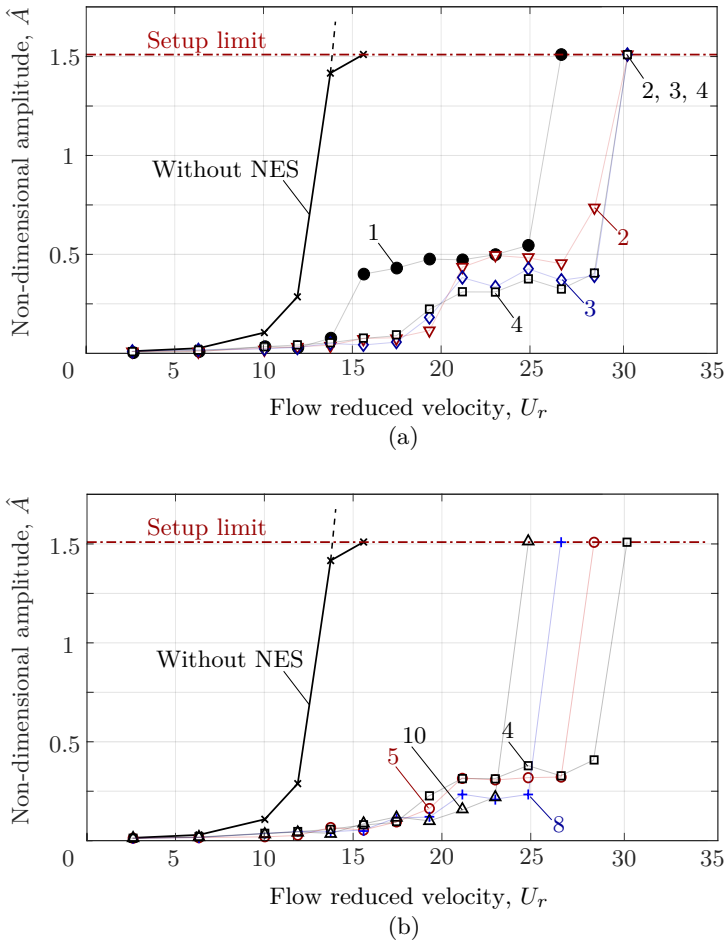

Figure 6.5 Amplitude response of : (a) the prism without NES ⊸⊷, with 1-ball NES •, with 2-ball NES ▽, with 3-ball NES ◇, and with 4-ball NES ▫; (b) the prism without NES ⊸⊷, with 4-ball NES ▫, with 5-ball NES ○, with 8-ball NES +, and with 10-ball NES △. NES mass ratio $\hat{m} = 0.079 \pm 0.002$ and radius ratio $\hat{r} = 0.5 \pm 0.001$ for all the tested configurations.

a jump in the amplitude of the prism with the 1-ball NES. Increasing the number of balls mitigates and delays this jump changing it instead into a gradual increase in the case of the 4-ball NES. Figure 6.5 b presents the responses of the prism with 4-balls, 5-balls, 8-balls and 10-balls. At low flow speeds $U_r < 17.4$, no considerable change appears in the behavior of the prism with the different NESs. For higher flow speeds, increasing the number of balls above four reduces the vibration amplitudes of the prism. Additionally, it limits the NES working range to reduced flow velocities 24.8, 23 and 21.1 for the 5-ball, 8-ball, and 10-ball NESs.

6.4.2 Dynamics of different NES configurations

We compare the dynamics of the 4-ball NES, an example of a multi-ball NES, with that of the single ball NES and discuss their effects on the prism displacement. A developed MATLAB code, using the wind-rose toolbox [163], plots the probability distributions of the NES mass centre location in terms of direction (represented by the length of the radial columns) and radius ρ_c (represented by various colours). A total of 36 bins, each of 10° size, are used around the cycle. Due to the high-speed camera storage limitation of $\sim$ 37 seconds at the resolution used, the sampling size does not capture the full distribution of the ball positions. This fact explains the lack of symmetry in the distributions.

Figure 6.6 depicts the location of the mass centre of the tested 1-ball and 4-ball NESs, traced at different reduced flow velocities U_r =: 17.4, 21.1, 24.8, and 28.5. For the 1-ball NES (Figure 6.6 a, b, c), the radius of the mass centre ρ_c is constant and equals 25mm, the racetrack radius. We observe the ball to be located around 0° for 20% of the time at $U_r = 17.4$ (Figure 6.6 a). That percentage increases to 30% and 38% in Figure 6.6 b, c for $U_r = 21.1$ and 24.8, respectively. While the radial position of the four balls' mass centre ρ_c varies between 0 and the theoretical maximum of $\rho_{c.max} = 17.44$ mm depending on the flow speed (Figure 6.6 d, e, f, g). At $U_r = 17.4$, ρ_c of the 4 balls ranges from 10 to $\rho_{c.max} = 17.44$ mm and oscillates between 280° and 300° (Figure 6.6 d). As U_r increases to 21.1 and 24.8, the range of most probable directions of the mass centre becomes wider, it varies between 260° and 330° for 5% of the time at $U_r = 21.1$. Whereas, ρ_c changes between 0 and 15 mm. In Figure 6.6 *d*, the balls oscillate with little amplitude all close together. While in Figure 6.6 e, f, they move around, increasing the ball spacing, which is reflected in the many colours. The appearance of several colours in Figure 6.6 e, f indicates the wide fluctuation range of ρ_c, which we point out as a leading parameter to characterise the multi-ball NES response. At $U_r = 28.5$ (Figure 6.6 g), the mass centre is likely located around 0°, while ρ_c decreases and mostly ranges between $0 - 10$ mm.

The oscillatory, intermittent and rotational response modes of the 1-ball NES were previously observed experimentally [158] and explained [164]. The ball experiences small oscillations in the oscillatory regime. While, in the rotational regime, the ball rotates for complete revolutions to kill the galloping, then stops until the prism amplitude reaches a critical threshold and repeats this cycle periodically. The intermittent regime is a transition between the oscillatory and the rotational ones. Here, the ball is observed to stay fixed at 0° and oscillate completing a few revolutions at $U_r = 17.4$ (Figure 6.6 a), as characterised by the intermittent regime. For higher flow speeds, the ball behaviour follows the rotational response, which increases the probability of finding the ball stopping around 0°.

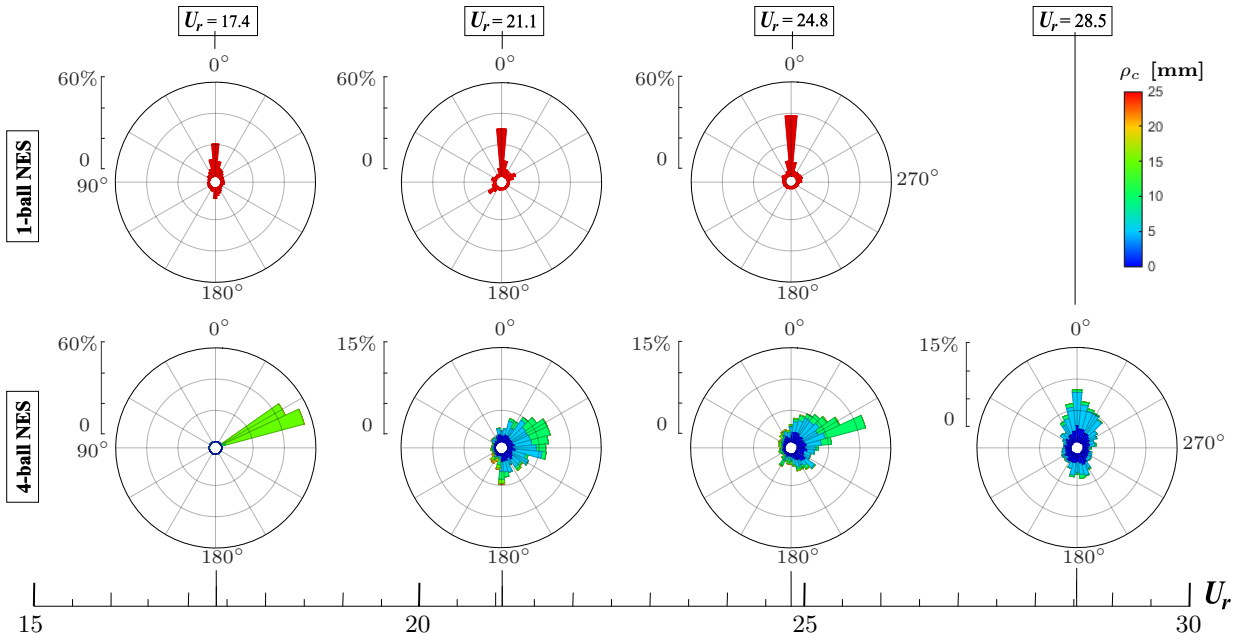

Figure 6.6 The probability distribution of the mass centre location of the 1-ball, and 4-ball NESs traced at different reduced flow velocities U_r = : (a, d) 17.4; (b, e) 21.1; (c, f) 24.8; and (g) 28.5, using a bin size of 10°. Notice that two different probability scales are used.

Using multiple balls in the same track certainly changes the NES dynamics compared to one ball. In a multi-ball NES, besides the effect of ball collisions in absorbing energy, the presence of multiple balls interrupts their rotational response. The 4-ball NES exhibits weak and strong response modes, which we characterise depending on the fluctuation range of the NES mass centre ρ_c. In the weak response, ρ_c variation is minimal as the balls stay together during small oscillations that are important enough to absorb the energy of the prism at $U_r = 17.4$. Increasing flow speed to $U_r = 21.1$ and 24.8 represents a higher excitation level and leads to the strong response mode where the balls oscillate expanding the fluctuation range of ρ_c to $0 - 17.44$ mm. At $U_r = 21.1$, the ball oscillations increase to the maximum, thus decreasing ρ_c below 5 mm most of the time. Above this speed, ρ_c is too small to sustain the dynamical coupling with the prism and the 4-ball NES is ineffective in mitigating the galloping amplitudes.

To assess the influence of the NES dynamics on the prism response, Figure 4.7 presents the displacement time histories of the prism equipped with each of the 1-ball and the 4-ball NES, focusing on the NES effective range $15 < U_r < 29$. At $U_r = 17.4$ (Figure 4.7 a), the 4-ball NES kills the prism galloping to an amplitude smaller than 0.15, whereas the 1-ball NES reduces its non-dimensional amplitudes below 0.35 resulting in a nearly steady vibration of

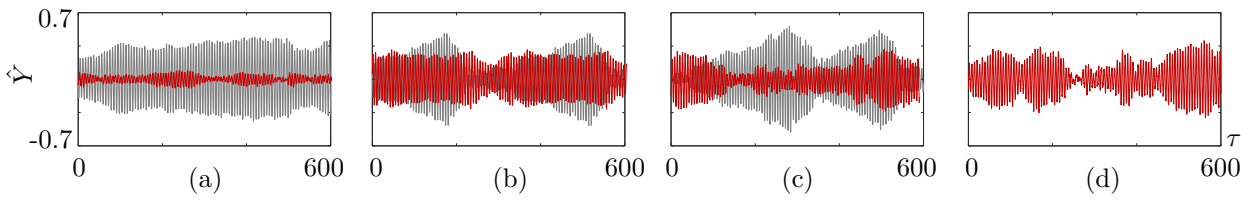

Figure 6.7 Time histories $\hat{Y}$ of the prism displacement equipped with a 4-ball NES (red curve) measured at different reduced flow velocities $U_r =$: (a) 17.4 ; (b) 21.1 ; (c) 24.8 ; and (d) 28.5. Dynamics of the prism equipped with a 1-ball NES (grey curve) is shown in (a)-(c). At the larger reduced velocities (d), the 1-ball NES system could not be studied as vibration amplitudes were too large.

the prism. At flow speeds $U_r = 21.1$ and 24.8, the 1-ball NES mitigates the prism galloping response. However, its dynamics in the rotational regime lead to periodic cycles of growing and attenuation of the prism amplitudes (Figure 4.7 b, c). The prism non-dimensional amplitude $\hat{A}$ with the 4-ball NES varies at these flow speeds, not exceeding 0.3. The prism with the 1-ball NES reaches the limit of the experiments at $U_r = 26.7$ (Figure 6.5 a) whereas, the 4-ball NES is still effective until $U_r = 28.5$, at which point the prism amplitude is reduced nearly to 0.35 as presented in Figure 4.7 d.

The dynamics of the 1-ball NES directly affects the prism response ; in the intermittent regime, the prism exhibits almost steady vibration, whereas it shows a strongly modulated response of periodic cycles rising and decreasing its amplitude in the rotational regime. In each cycle, the ball rotates continuously to mitigate the prism amplitudes then stops at an equilibrium position for a time, during which the prism amplitude grows again to a critical value that breaks the ball equilibrium and cause its rotation. Multiple balls in the same track cannot hit the equilibrium position ($\theta = 0^\circ$ or 180°) simultaneously. As a result, we can not observe the rotational regime experienced by a single ball. The balls oscillate in the multi-ball NES instead of stopping, preventing the prism vibration from reaching the amplitude threshold reached by the prism coupled with the 1-ball NES. Multiple balls do not experience the regular periodic cycles observed in the rotational regime of the 1-ball NES. Thus, the 4-ball NES can mitigate the prism galloping without periodic sudden decreases in the prism displacements that cause a fatigue risk to the system coupled with a 1-ball NES.

6.5 Conclusion

The single ball NES presented in the literature is a simple, low-cost way for damping flow-induced vibration. In this paper, we propose a multi-ball NES of equivalent mass that is more effective as it absorbs energy in two ways; the presence of multiple balls disrupts the motion of one another, and the dissipation of their collisions. We highlight the radial location of the balls' mass centre and the track crowdedness as two important factors affecting the behaviour of the multi-ball NES. The increase in ball numbers decreases the maximum radius of the NES mass centre $\rho_{c.max}$, which can improve the NES suppression efficiency within a certain range unless the radius is too small to sustain the dynamic coupling of the prism and the balls. Although a high number of balls in the same track leads to more collisions, these collisions can be less effective due to the limited free paths for each ball. Accordingly, an optimal NES track crowdedness ratio γ_t probably exists which would lead to the maximum benefit of ball impacts. The optimization of $\rho_{c.max}$ and γ_t can be a question for future work, notably through numerical modelling. Testing various configurations of equivalent mass NESs showed that the vibration amplitude of the prism decreases by increasing the number of balls throughout all experiments involving one to ten balls. Two conflicting trends were observed regarding the NES working range; it expands by using two balls instead of a large one of equivalent mass and remains the same for three and four balls. Any further increase in the number of balls overcrowds the NES track, limiting the motion of the balls and resulting in less effective impacts, which reduces the working range of the 5-ball, 8-ball, and 10-ball NESs. For a NES of mass ratio $\hat{r} = 0.08$ and radius ratio $\hat{r} = 0.5$, four balls is the best configuration that increases the reduced velocity of large-amplitude galloping by 10% compared to a single ball of equivalent mass. Moreover, using multiple balls reduces the fatigue risk as its dynamic coupling with the prism does not lead to the strongly modulated response experienced by a prism coupled with a 1-ball NES.

The prism galloping in our tests was limited to a non-dimensional amplitude of 1.5. Therefore, a numerical model will be a future challenge to simulate the effect of impact between NES balls and consider the dynamics of the prism coupled with multi-ball NES at large galloping amplitudes.

CHAPTER 7 GENERAL DISCUSSION

We considered the design simplicity and the low fabrication cost of a vibration absorber as important parameters for extending its practical implementation to many systems. The literature reviewed different kinds of passive vibration absorbers and highlighted our interest in the class of nonlinear energy sinks. The typical form of a rotative NES presented in the literature consists of a tip mass coupled to a primary structure by a rigid bar of fixed length. The originality of this work is to introduce a purely rotative NES using a free metal ball moving in a circular track without direct coupling to the primary system. The proposed NES, which we named ball-in-track (BIT) NES, is a simple, low-cost and robust passive vibration absorber able to mitigate the galloping of a square prism.

Chapter 4 presented the galloping experiments that validated the BIT-NES effectiveness in delaying the galloping of a square prism [158]. Wind tunnel tests of the BIT-NES exhibited three different response modes ; oscillatory, intermittent and rotational, and provided the boundaries of each regime and the critical flow speed, beyond which the NES was no longer able to mitigate galloping amplitudes. The ball response changes from one mode to another depending on the excitation level of the primary system vibration. In the oscillatory regime, the kinetic energy consumed by the NES ball during its small oscillations is enough to absorb the energy extracted from the flow by the prism at low flow speeds and delay the galloping occurrence. When the energy of the prism increases at higher flow speeds, the ball rotates fast and faster in the intermittent and rotational regimes to absorb the prism energy. According to the concept of targeted energy transfer across the integrated prism-NES system, the rotational regime is the most efficient. The NES ball engages with the prism dynamics and rotates with the prism natural frequency experiencing 1:1 resonance capture. This results in a strongly modulated response of the prism illustrating the energy transfer between the galloping prism and the NES. At higher flow velocities, a ball rotating with the prism frequency cannot absorb the energy of the prism. Thus, the ball motion becomes out of sync with the prism vibration and ineffective in mitigating the galloping amplitudes. The experimental setup limitation in the maximum amplitude did not allow for testing the system dynamics at high reduced flow velocities. The experiments [158] demonstrated the NES effect in delaying the galloping upon speeding up the flow without tackling the problem in the case of slowing down the flow.

In chapter 5, we developed a model employing measured data of the galloping and the ball damping coefficients to realistically simulate the dynamics of the prism-NES system

in a parameter range, difficultly accessible by experiments. The simulations investigated the NES effect considering both increasing and decreasing flow speeds. Galloping of the square prism considered here involved a hysteresis phenomenon over a range of flow speeds $14.5 < U_r < 17.5$, at which the prism response depends on the initial conditions. With increasing flow speed, the NES delayed the galloping occurrence to much higher flow speeds, and the prism follows the lower limit cycle branch. While in decreasing flow speed, the prism amplitude reached the upper limit cycle due to the relatively large initial displacement of the prism. Since the NES behaviour depends on the excitation level, the NES was efficient in delaying the occurrence of galloping but less effective in stabilizing a prism experiencing a high excitation level due to very large amplitude galloping.

Upon increasing the flow speed, the simulations demonstrated the oscillatory, intermittent and rotational regimes observed in experiments and predicted an ineffective response mode characterised with high-amplitude galloping. It was hard to experimentally define exact boundaries for the intermittent response mode because it is a transition regime between the oscillatory and rotational responses. In the numerical analysis, considering the angular speed of the ball was useful to accurately specify the limit of the intermittent regime coinciding with $\dot{\theta} < 0.8$ times the angular natural frequency of the prism. The NES ball interacted with the system dynamics in the rotational regime and adapted its behaviour with increasing flow speeds to mitigate galloping amplitudes over a wide range of flow speeds. Above a critical flow speed U_{crit}, the simulations demonstrated an ineffective regime in which the ball cannot engage with the system frequency. The ball rotated with high angular speeds, approximately 4 times the prism natural angular frequency in an irregular manner, often changing direction. The ball's fast revolutions in this regime were insufficient to suppress the prism vibration. Therefore, the NES was no longer beneficial in absorbing the high-amplitude galloping as the energy extracted by the vibrating prism from the airflow exceeds the energy dissipation rate of the NES. Upon slowing down the flow from $U_r = 30$, we observed the ineffective NES regime at high flow speeds. Then the ball behaviour changed to random rotations at $U_r = 25$ and large oscillations at 17.5 with ineffective damping effect on the prism amplitudes. It was hard for the ball to interact with the dynamics of the prism at large-amplitude galloping, which led to the absence of the NES rotational response and reduced the NES effective range compared to the first case. At lower flow velocities, the intermittent response appears in a narrow range of reduced flow speeds. While, the oscillatory regime was observed at the same flow speed range $U_r < 14$, comparing to the case of accelerating flow.

The analytical analysis, presented in chapter 5, estimated boundaries between NES regimes. Considering the prism mass as an excitation source of the NES provided a value for the prism amplitude ($Y_{0_{crit}} = \hat{r}\sqrt{\frac{1}{4} + 4\zeta_{\theta}^2}$) above which the oscillatory regime is impossible.

This amplitude boundary defined the transition between the oscillatory and the intermittent regime. Additionally, the proposed power flow analysis of the integrated prism-NES system came out with an analytical estimation for the limit of the NES effective range and explained the behaviour of the ball in the rotational regime. Figure 7.1 presents the mechanism of energy transfer in the prism-NES system, illustrating the power terms of the aerodynamic load $\bar{P}_{Fy}$, the damping forces of the support $\bar{P}_d$, the power P_{tr} transferred to the NES and the power dissipated due to the ball friction P_{dis}. We compared the power extracted from the flow by the prism P_{F_y} (minus its structural damping P_d) with the maximum energy the ball could dissipate in ideal 1:1 resonance capture, where it rotates with a practically constant angular velocity equals to that of the prism, to obtain the limit of successful energy transfer. This limit defines the critical flow speed $U_{crit} = 24.5$, above which the NES of $\hat{m} = 0.08$ and $\hat{r} = 0.6$ is ineffective. In the perspective of the NES, comparing the transferred power $\bar{P}_{tr}$, gained by the NES, and the power dissipated $\bar{P}_{dis}$ by ball friction in the rotational response provided a minimum value of the prism amplitude that sustains ball rotation ($A_{min} \geq 4\hat{r}\zeta_\theta$). We explained the rotational regime as a competition between the ability of the system to transfer energy from the vibrating prism to the NES, and the capacity of the NES to dissipate energy. The prism accumulates energy from the flow over multiple cycles until the ball is excited, at which point it spins and dissipates energy until the prism amplitude is too small to sustain the motion. Repetition of this cycle leads to the strongly modulated response of the prism, observed in the rotational regime.

Figure 7.2 compares the NES regime boundaries obtained from the numerical simulations with both the analytical estimations and the previous experiments. We could define the boundaries between the oscillatory, intermittent and rotational regimes as $U_{osc/int}$, and $U_{int/rot}$ and the limit of the NES effective range U_{crit}. The numerical simulations estimated $U_{osc/int}$, and

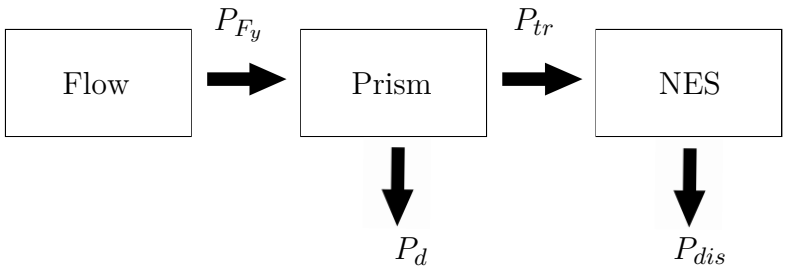

Figure 7.1 The energy transfer mechanism in the prism-NES integrated system, illustrating the power terms of the aerodynamic load $\bar{P}_{Fy}$, the damping forces of the support $\bar{P}_d$, the power P_{tr} transferred to the NES and the power dissipated due to the ball friction P_{dis}.

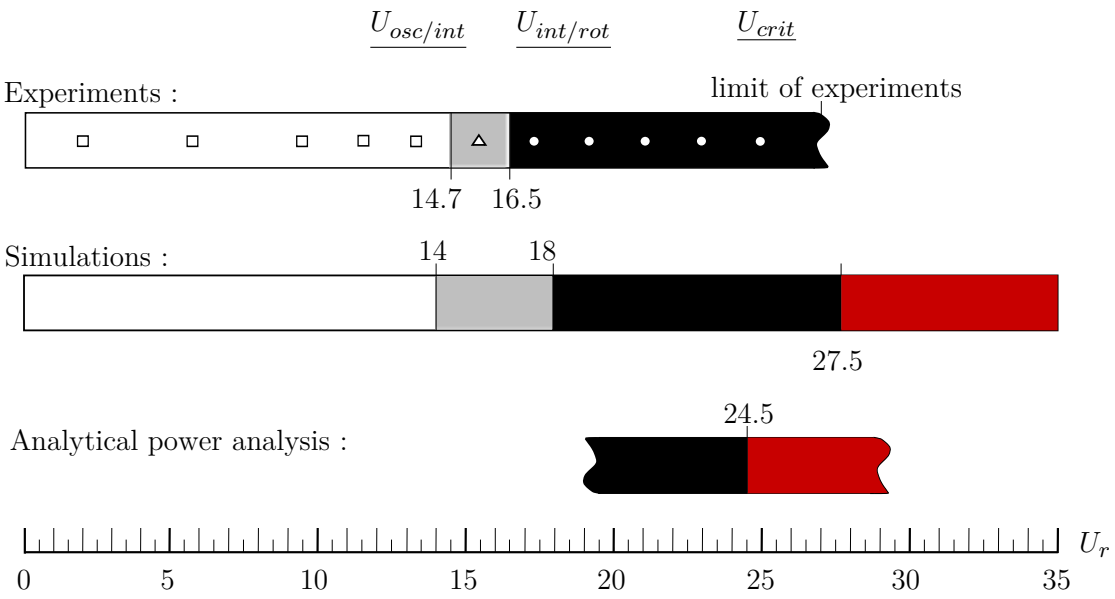

Figure 7.2 Comparing NES regime boundaries obtained from our simulation considering a NES of $\hat{m} = 0.08$ and $\hat{r} = 0.6$, with experimental results (oscillatory ◻, Intermittent △, and Rotational ○ regimes, and analytical estimations. The flow speed range is shaded by different colours for NES regimes : oscillatoy (white), intermittent (gray), rotational (black), and the ineffective (red).

$U_{int/rot}$ as 14 and 18, respectively. Comparing with the boundaries defined experimentally, 14.7 and 16.5, we evaluated a relative error of 0.05 and 0.1. The experiments provided a range for the critical reduced flow velocity $25 < U_{crit} \leq 27$, which was defined numerically as 27.5, where the proposed power flow analysis evaluated this critical value as 24.5.

As presented in chapter 6, we used multiple balls to take advantage from the collisions between them in improving the NES suppression efficiency. Testing various configurations of multi-ball NES demonstrated its higher suppression efficiency compared to a single-ball NES of equivalent mass. In a multi-ball NES, besides the effect of ball collisions in absorbing energy, they also interrupt the rotation of balls. As a result, multiple balls do not experience the periodic cycles of rotating and stopping observed in the rotational regime of the 1-ball NES. Multiple balls in the same track cannot hit the equilibrium position ($\theta = 0°$ or $180°$) simultaneously. Thus, they oscillate instead of stopping, preventing the prism vibration from reaching the amplitude threshold reached by the prism coupled with 1-ball NES. Additionally, the change of the mass distribution in the multi-ball NES, that occurs due to ball motion, affect the dynamic coupling with the galloping prism. These explanations revealed the reason for the outperformance of the multi-ball NES compared to the single-ball NES.

The experiments showed that increasing the ball number reduces the vibration amplitude of the prism through all testing involving one to ten balls. Regarding the NES effective range, two opposing trends were observed. Using twoăballs instead of a large one of equivalent mass expanded the NES working range, which remained the same for the 3-ball and 4-ball NESs. Further increasing the ball number above four overcrowded the NES track and limited the balls' motion, resulting in less effective impacts between them. Thus, the working ranges of the 5-ball, 8-ball, and 10-ball NESs were reduced compared to the 4-ball NES.

The current research introduced the ball-in-track (BIT) NES as a purely rotative NES able to absorb the galloping of a square prism. The experiments and the realistic simulations investigated the efficiency of the proposed NES in mitigating the galloping of a square prism. Besides, analytical analysis for the power flow across the prism-NES integrated system explained the behaviour of the BIT-NES. This research also advanced a new technique for measuring the damping of a rotating ball through free rotation tests. The simple structure of the BIT-NES and the deep understanding of its behaviour may extend its usage to many applications. In particular, it can damp wind-induced galloping on power lines, high-mounted signboards, long slender structures, and skyscrapers.

CHAPTER 8 CONCLUSION AND FUTURE WORK

8.1 Conclusion

The nonlinear energy sink (NES) was recommended in the literature review over other types of linear absorbers due to its ability to mitigate the vibration of the primary structure, coupled to it, without introducing new frequencies to the system. The rotative NES is a type of such absorbers, typically consisting of a tip mass linked to the primary structure by a rigid bar of fixed length. We emphasized that the design simplicity and the low fabrication cost of a vibration absorber are important factors that extend its practical implementation to various systems. Accordingly, the main contributions of our research are:

- Introducing a purely rotative NES composed of a free metal ball moving in a circular track without direct coupling to the primary system. Wind tunnel tests demonstrated the advantage of the proposed NES in mitigating the galloping of a square prism model without changing the prism characteristics.
- Experimental investigation of the dynamics of the prism-NES system. The proposed NES exhibited three different regimes: oscillatory, intermittent, and rotational, which we named based on the response of the NES ball. The oscillatory regime is observed at low flow speeds and characterized by small oscillations for both the prism and the NES ball. Although the ball's angular displacement did not exceed 70 degrees, it delays the galloping occurrence. The intermittent regime appears at higher flow speeds within a narrow range, in which the ball oscillates with low angular velocities leading to almost steady vibration of the prism with a maximum amplitude below 30 mm. The more powerful excitation at higher flow speeds results in more stable rotations of the NES ball in the rotational regime. The NES ball rotates with high angular velocities to kill the galloping amplitudes. Then, it stops until the prism amplitude reaches a critical threshold. The repetition of that cycle leads to a strongly modulated response (SMR) of the prism, showing periodic cycles of attenuation and rising in the prism vibration displacement.
- Quantifying the impact of the main NES parameters on its behaviour. The simple design of the NES allowed to easily change the dimensions of its track to accommodate various size balls. The increase of the mass ratio expands the NES working range. Regarding the NES regime mapping, we observed the intermittent regime with the NES of higher mass only coinciding with a small jump in the prism amplitude response. While increasing the radius ratio increases the prism vibration amplitudes and reduces both the NES effective

range and the range of the intermittent regime. The effective range of the lubricated NES of less friction is greater than that of the dry one. Reduced friction in the lubricated NES also reduces the intermittent regime range eliminating the small jump in prism amplitude, which occurs at the beginning of the intermittent regime. The radial clearance between the NES track walls and the rotating ball is an important parameter, its increase significantly decreases the prism vibration amplitudes. The most effective NES has the largest mass ratio, the lowest radius ratio and the greatest radial clearance within the range of NES parameter values tested in our experiments.

- Providing a precise fitting for the galloping force coefficient C_y as a function of the square prism angle of attack α. Through static wind tunnel experiments, we measured C_y at different angles of attack α. Then Kolmogorov-Smirnov (K-S) test was applied to eliminate systematic errors in measuring the angle of attack.
- Developing a new approach to estimate the ball damping coefficient c_θ through free rotation tests. The experiments provided a certain angular speed, over which the ball contact with the track sidewalls becomes significant and increases the friction of the NES rotating ball. The damping variation is a unique advantage of the Ball-in-track NES ; small damping at low angular speeds allows the ball to rotate easily, while relatively large damping at high angular velocities dissipates more energy.
- Simulating the dynamics of the prism-NES integrated system with employing experimental data of the galloping force C_y and the ball damping C_θ coefficients for the numerical model. The simulations exhibited the oscillatory, intermittent, and rotational response modes observed in the experiments. Moreover, it expected an ineffective regime at high flow speeds that we could not examine experimentally. In this fourth regime, the NES is ineffective in mitigating the galloping amplitudes.
- Analytical estimations for the oscillatory regime boundary and the limit of the NES effective range. Considering the mass of the prism as a parametric excitation source for the NES ball provided an analytical expression for the amplitude, below which the ball's stable oscillations are impossible $Y_{0_{crit}} = \hat{r}\sqrt{\frac{1}{4} + 4\zeta_\theta^2}$. Additionally, a power flow analysis across the prism-NES integrated system predicted the critical flow speed, at which the NES of mass ratio $\hat{m} = 0.08$ and radius ratio $\hat{r} = 0.6$, is ineffective as $U_r = 24.5$, with a relative error 0.07 compared to the experiments. Looking at the power flow in perspective to the NES explained the ball behaviour in the rotational regime. The ball stops rotating when the transferred power to the NES power balances out the power dissipated by ball friction. The proposed analysis provided the minimum prism amplitude sustaining the ball rotational response $A_{min} = 4\hat{r}\zeta_\theta$.

- Developing a multi-ball NES composed of many balls moving in the same circular track. Experimental testing revealed the high suppression efficiency of the multi-ball NES compared to a single-ball NES of equivalent mass. The single ball rotates continuously to kill the galloping, then stops until the prism vibrations reach a threshold amplitude. This cycle is repeated, leading to a rotational regime. In the multi-ball NES, besides ball collisions absorbing energy, they also interrupt the rotation of balls. As a result, multiple balls do not experience the regular periodic cycles observed in the rotational regime of the 1-ball NES. Many balls in the same track cannot hit the equilibrium position ($\theta = 0^\circ$ or 180°) simultaneously. Thus, they oscillate instead of stopping, preventing the prism vibration from reaching the amplitude threshold reached by the prism coupled with 1-ball NES.
- Demonstrating the influence of the ball number on the behaviour of the multi-ball NES experimentally. Testing various configurations of equivalent mass NESs showed that the vibration amplitude of the prism decreases by increasing the ball number throughout all experiments involving one to ten balls. Two conflicting trends were observed regarding the NES working range ; it expands by using two balls instead of a large one of equivalent mass and remains the same for the 3-ball and 4-ball NESs. Any further increase in the number of balls overcrowds the NES track, which reduces the working range of the 5-ball, 8-ball, and 10-ball NESs. For a NES of mass ratio $\hat{r} = 0.08$ and radius ratio $\hat{r} = 0.5$, the 4-ball NES is the most efficient multi-ball NES that increases the reduced velocity of large-amplitude galloping by 10% compared to the 1-ball NES of equivalent mass.
- Identifying the key parameters controlling the behaviour of the multi-ball NES. The mass distribution of balls and the collisions between them significantly affect the behaviour of the multi-ball NES. Thus, we highlighted two leading parameters in the design of the multi-ball NES: the maximum radius of the NES mass centre ρ_c and the NES track crowdedness ratio γ_t, which indicates the track portion filled with balls. Increasing the number of balls reduces the maximum radius of the NES mass centre ρ_c and increases the NES track crowdedness ratio γ_t. High track crowdedness ratios limit the motion of the balls, resulting in less effective collisions

8.2 Limitations

The experimental setup, used for the galloping experiments, limited the maximum amplitude of the prism in galloping experiments to 75mm, which equals 1.5 times the square prism side length. As a result, it restricted the testing of large amplitude galloping at high flow speeds.

Regarding the square prism model, we developed a lightweight prism spanning almost the entire height of the wind tunnel test section without too much blockage effect. We only tested this model whose mass ratio with reference to air-flow $m^* = {}^{M}/_{\rho L D^2} = 750$ and cannot infer about other mass ratios. In the Quasi-static experiments, We neglected the variation of the galloping force coefficient (C_y) with Reynolds number (Re). The wind tunnel static experiments provided C_y as a function of the square prism angle of attack (α), at a constant flow speed of $U = 30\,\mathrm{m/s}$, which is equivalent to $Re = 101 \times 10^3$. The numerical model employed the obtained fitting in simulating the prism galloping response, ignoring its variation with flow speed.

8.3 Future work and recommendations

The simple-structured NES that we introduced is applicable to many systems. It could mitigate wind-induced vibrations on various structures such as power lines, high-rise structures and skyscrapers. The proposed model and the analytical investigations predict the dynamics of the integrated prism-NES system at high vibration amplitudes, covering the limitation of experiments. This can extend the practical implementation of such NESs and help in optimizing the NES design based on the characteristics of a primary system. Accordingly, we recommend testing the proposed NES with square prism models of various mass ratios with reference to air flow (may be extended to rectangular prisms of different aspect ratios) to illustrate the influence of the primary system characteristics on the NES behaviour. Employing various NES track shapes, even inclined ones, can detect their effect on the ball behaviour and the NES suppression efficiency. Regarding the multi-ball NES, the experimental characterisation of the impact between balls will assess its role in improving the energy absorption capability of the multi-ball NES. Considering this effect in simulating the prism galloping response with multi-ball NES will help in a deep understanding of the multi-ball NES complicated dynamics. Finally, we recommend the examination of the ball-in-track NESeffectiveness in mitigating other types of FIV such as wing instabilities, vibrations of fluid-conveying pipes, and the VIV of cylinders.

8.4 Research Outcomes

Journal articles

1. "Wind tunnel demonstration of galloping mitigation with a purely nonlinear energy sink". Journal of Fluids and Structures (2021). **- Published: January 2021 -**
   DOI : http://dx.doi.org/10.1016/j.jfluidstructs.2020.103169

2. "How a ball free to orbit in a circular track mitigates the galloping of a square prism". Nonlinear Dynamics. **- Submitted: October 2021 -**
   Preprint DOI : https://doi.org/10.21203/rs.3.rs-973095/v1

3. "Multiple balls rotating in a circular track experimentally mitigates the galloping of a square prism". Journal of Sound and Vibration. **- Submitted: November 2021 -**

Conferences

1. "Going in circles to mitigate flow-induced vibrations" Virtual Technical Meeting of the Society of Engineering Science (SES). September, 2020.

2. "Multi balls rotating in a circular track efficiently mitigates flow-induced vibrations" 25th International Congress of Theoretical and Applied Mechanics (ICTAM 2021), Milan, Italy.
   - Awarded the Bureau Prize for the best seminar presentation out of 388 participants -

REFERENCES

[1] Nagarajaiah Satish and Sonmez Ertan, "Structures with semiactive variable stiffness single/multiple tuned mass dampers," Journal of Structural Engineering, vol. 133, pp. 67–77, 2007.

[2] R. Blevins, Flow induced vibration. Krieger, 2001.

[3] M. Paidoussis, S. Price, and E. de Langre, Fluid-Structure Interactions : Cross-Flow-Induced Instabilities. Cambridge University Press, 2010.

[4] M. Levy and M. Salvadori, Why Buildings Fall Down : How Structures Fail. W.W. Norton, 2002.

[5] H. Frahm, "Device for damping vibrations of bodies," German Patent 989 958, 1911.

[6] Housner G. W., Bergman L. A., Caughey T. K., Chassiakos A. G., Claus R. O., Masri S. F., Skelton R. E., Soong T. T., Spencer B. F., and Yao J. T. P., "Structural control : Past, present, and future," Journal of Engineering Mechanics, vol. 123, no. 9, pp. 897–971, 1997.

[7] H. Yamaguchi and N. Harnpornchai, "Fundamental characteristics of multiple tuned mass dampers for suppressing harmonically forced oscillations," Earthquake Engineering & Structural Dynamics, vol. 22, no. 1, pp. 51–62, 1993.

[8] F. Weber, "Optimal semi-active vibration absorber for harmonic excitation based on controlled semi-active damper," Smart Materials and Structures, vol. 23, 2014.

[9] ——, "Semi-active vibration absorber based on real-time controlled MR damper," Mechanical Systems and Signal Processing, vol. 46, pp. 272–288, 2014.

[10] Patten W. N., Mo C., Kuehn J., and Lee J., "A primer on design of semi active vibration absorbers (SAVA)," Journal of Engineering Mechanics, vol. 124, pp. 61–68, 1998.

[11] S. Nagarajaiah and N. Varadarajan, "Smart variable stiffness control systems," in Proceedings of Smart Structures and Materials 2001 : Smart Systems for Bridges, Structures, and Highways, vol. 4330. International Society for Optics and Photonics, 2001, pp. 345–353.

[12] S. F. Masri, "Analytical and experimental studies of multipleunit impact dampers," The Journal of the Acoustical Society of America, vol. 45, no. 5, pp. 1111–1117, 1969.

[13] Y. S. Lee, A. F. Vakakis, L. A. Bergman, D. M. McFarland, G. Kerschen, F. Nucera, S. Tsakirtzis, and P. N. Panagopoulos, "Passive non-linear targeted energy transfer and its applications to vibration absorption : A review," Proceedings of the Institution of

Mechanical Engineers, Part K : Journal of Multi-body Dynamics, vol. 222, pp. 77–134, 2008.

[14] A. F. Vakakis and R. H. Rand, "Non-linear dynamics of a system of coupled oscillators with essential stiffness non-linearities," International Journal of Non-Linear Mechanics, vol. 39, no. 7, pp. 1079–1091, 2004.

[15] G. Kerschen, Y. S. Lee, A. F. Vakakis, D. M. McFarland, and L. A. Bergman, "Irreversible passive energy transfer in coupled oscillators with essential nonlinearity," SIAM Journal on Applied Mathematics, no. 2, pp. 648–679, 2006.

[16] X.-F. Geng, H. Ding, X.-Y. Mao, and L.-Q. Chen, "Nonlinear energy sink with limited vibration amplitude," Mechanical Systems and Signal Processing, vol. 156, p. 107625, 2021.

[17] M. A. AL-Shudeifat, "Highly efficient nonlinear energy sink," Nonlinear Dynamics, vol. 76, no. 4, pp. 1905–1920, 2014.

[18] N. E. Wierschem, D. D. Quinn, S. A. Hubbard, M. A. Al-Shudeifat, D. M. McFarland, J. Luo, L. A. Fahnestock, B. F. Spencer, A. F. Vakakis, and L. A. Bergman, "Passive damping enhancement of a two-degree-of-freedom system through a strongly nonlinear two-degree-of-freedom attachment," Journal of Sound and Vibration, vol. 331, pp. 5393–5407, 2012.

[19] A. Blanchard, L. A. Bergman, and A. F. Vakakis, "Vortex-induced vibration of a linearly sprung cylinder with an internal rotational nonlinear energy sink in turbulent flow," Nonlinear Dynamics, 2019.

[20] A. S. Saeed, M. A. AL-Shudeifat, and A. F. Vakakis, "Rotary-oscillatory nonlinear energy sink of robust performance," International Journal of Non-Linear Mechanics, vol. 117, p. 103249, 2019.

[21] E. Gourc, G. Michon, S. Seguy, and A. Berlioz, "Targeted energy transfer under harmonic forcing with a vibro-impact nonlinear energy sink : Analytical and experimental developments," Journal of Vibration and Acoustics, vol. 137, no. 3, 2015.

[22] O. V. Gendelman and A. Alloni, "Dynamics of forced system with vibro-impact energy sink," Journal of Sound and Vibration, vol. 358, pp. 301–314, 2015.

[23] J. Wang, N. E. Wierschem, B. F. Spencer Jr, and X. Lu, "Track nonlinear energy sink for rapid response reduction in building structures," Journal of Engineering Mechanics, vol. 141, no. 1, p. 04014104, 2015.

[24] J. Wang, N. E. Wierschem, B. Wang, and B. F. Spencer Jr, "Multi-objective design and performance investigation of a high-rise building with track nonlinear energy sinks," The Structural Design of Tall and Special Buildings, vol. 29, no. 2, p. e1692, 2020.

[25] J. Wang, C. Zhang, H. Li, and Z. Liu, "Experimental and numerical studies of a novel track bistable nonlinear energy sink with improved energy robustness for structural response mitigation," Engineering Structures, vol. 237, p. 112184, 2021.

[26] A. Vakakis, "Inducing passive nonlinear energy sinks in vibrating systems," J. Vib. Acoust., vol. 123, no. 3, pp. 324–332, 2001.

[27] Y.-Y. Chen, Z.-C. Qian, W. Zhao, and C.-M. Chang, "A magnetic bi-stable nonlinear energy sink for structural seismic control," Journal of Sound and Vibration, vol. 473, p. 115233, 2020.

[28] N. Menga, F. Bottiglione, and G. Carbone, "Nonlinear viscoelastic isolation for seismic vibration mitigation," Mechanical Systems and Signal Processing, 2021.

[29] F. Gomez, G. A. Fermandois, and B. F. Spencer Jr, "Optimal design of nonlinear energy sinks for mitigation of seismic response on structural systems," Engineering Structures, vol. 232, p. 111756, 2021.

[30] Y.-W. Zhang, S. Hou, Z. Zhang, J. Zang, Z.-Y. Ni, Y.-Y. Teng, and L.-Q. Chen, "Nonlinear vibration absorption of laminated composite beams in complex environment," Nonlinear Dynamics, pp. 1–18, 2020.

[31] J. Chen, W. Zhang, M. Yao, J. Liu, and M. Sun, "Vibration reduction in truss core sandwich plate with internal nonlinear energy sink," Composite Structures, vol. 193, pp. 180–188, 2018.

[32] Y.-H. Sun, Y.-W. Zhang, H. Ding, and L.-Q. Chen, "Nonlinear energy sink for a flywheel system vibration reduction," Journal of Sound and Vibration, vol. 429, pp. 305–324, 2018.

[33] A. Haris, P. Alevras, M. Mohammadpour, S. Theodossiades, and M. OMahony, "Design and validation of a nonlinear vibration absorber to attenuate torsional oscillations of propulsion systems," Nonlinear Dynamics, pp. 1–17, 2020.

[34] C. Snoun, B. Bergeot, and S. Berger, "Prediction of the dynamic behavior of an uncertain friction system coupled to nonlinear energy sinks using a multi-element generalized polynomial chaos approach," European Journal of Mechanics-A/Solids, vol. 80, p. 103917, 2020.

[35] B. Bergeot, S. Bellizzi, and B. Cochelin, "Analysis of steady-state response regimes of a helicopter ground resonance model including a non-linear energy sink attachment," International Journal of Non-Linear Mechanics, vol. 78, pp. 72–89, 2016.

[36] Y. Jin, S. Hou, and T. Yang, "Cascaded essential nonlinearities for enhanced vibration suppression and energy harvesting," Nonlinear Dynamics, pp. 1–12, 2021.

[37] P. R. Raj and B. Santhosh, "Parametric study and optimization of linear and nonlinear vibration absorbers combined with piezoelectric energy harvester," International Journal of Mechanical Sciences, vol. 152, pp. 268–279, 2019.

[38] W. Tian, Y. Li, P. Li, Z. Yang, and T. Zhao, "Passive control of nonlinear aeroelasticity in hypersonic 3-d wing with a nonlinear energy sink," Journal of Sound and Vibration, vol. 462, p. 114942, 2019.

[39] C. Fernandez-Escudero, M. Gagnon, E. Laurendeau, S. Prothin, A. Ross, and G. Michon, "Experimental and numerical aeroelastic analysis of airfoil-aileron system with nonlinear energy sink," in Nonlinear Structures and Systems, Volume 1. Springer, 2020, pp. 133–135.

[40] M. Khazaee, S. Khadem, A. Moslemi, and A. Abdollahi, "A comparative study on optimization of multiple essentially nonlinear isolators attached to a pipe conveying fluid," Mechanical Systems and Signal Processing, vol. 141, p. 106442, 2020.

[41] R. K. R. Tumkur, E. Domany, O. V. Gendelman, A. Masud, L. A. Bergman, and A. F. Vakakis, "Reduced-order model for laminar vortex-induced vibration of a rigid circular cylinder with an internal nonlinear absorber," Communications in Nonlinear Science and Numerical Simulation, vol. 18, pp. 1916–1930, 2013.

[42] A. Mehmood, A. H. Nayfeh, and M. R. Hajj, "Effects of a non-linear energy sink (NES) on vortex-induced vibrations of a circular cylinder," Nonlinear Dynamics, vol. 77, pp. 667–680, 2014.

[43] H. L. Dai, A. Abdelkefi, and L. Wang, "Vortex-induced vibrations mitigation through a nonlinear energy sink," Communications in Nonlinear Science and Numerical Simulation, vol. 42, pp. 22–36, 2017.

[44] A. Blanchard, L. A. Bergman, and A. F. Vakakis, "Vortex-induced vibration of a linearly sprung cylinder with an internal rotational nonlinear energy sink in turbulent flow," Nonlinear Dynamics, vol. 99, no. 1, pp. 593–609, 2020.

[45] T. Ueno and G. R. Franzini, "Numerical studies on passive suppression of one and two degrees-of-freedom vortex-induced vibrations using a rotative non-linear vibration absorber," International Journal of Non-Linear Mechanics, vol. 116, pp. 230–249, 2019.

[46] H. L. Dai, A. Abdelkefi, and L. Wang, "Usefulness of passive non-linear energy sinks in controlling galloping vibrations," International Journal of Non-Linear Mechanics, vol. 81, pp. 83–94, 2016.

[47] B. Teixeira, G. R. Franzini, and F. Gosselin, "Passive suppression of transverse galloping using a nonlinear energy sink," Proceeding of the 9^{th} International Symposium

on Fluid-Structure Interactions, Flow-Sound Interactions, Flow-Induced Vibration and Noise, 2018.

[48] N. E. Wierschem, S. A. Hubbard, J. Luo, L. A. Fahnestock, B. F. Spencer, D. M. McFarland, D. D. Quinn, A. F. Vakakis, and L. A. Bergman, "Response attenuation in a large-scale structure subjected to blast excitation utilizing a system of essentially nonlinear vibration absorbers," Journal of Sound and Vibration, vol. 389, pp. 52–72, 2017.

[49] C. Dongyang, L. K. Abbas, W. Guoping, R. Xiaoting, and P. Marzocca, "Numerical study of flow-induced vibrations of cylinders under the action of nonlinear energy sinks (NESs)," Nonlinear Dynamics, vol. 94, pp. 925–957, 2018.

[50] T. Majewski, D. Szwedowicz, and M. A. M. Melo, "Self-balancing system of the disk on an elastic shaft," Journal of Sound and Vibration, vol. 359, pp. 2–20, 2015.

[51] F. W. Lanchester, Aerodynamics : constituting the first volume of a complete work on aerial flight. A. Constable & co., ltd., 1907.

[52] G. V. Parkinson, M. J. Lighthill, and A. Silverleaf, "Wind-induced instability of structures," Philosophical Transactions of the Royal Society of London. Series A, Mathematical and Physical Sciences, vol. 269, no. 1199, pp. 395–413, 1971.

[53] E. Naudascher and Y. Wang, "Flow-induced vibrations of prismatic bodies and grids of prisms," Journal of Fluids and Structures, vol. 7, no. 4, pp. 341–373, 1993.

[54] G. V. Parkinson and J. D. Smith, "The square prism as an aeroelastic non linear oscillator," The Quarterly Journal of Mechanics and Applied Mathematics, vol. 17, pp. 225–239, 1964.

[55] G. Parkinson, "Phenomena and modelling of flow-induced vibrations of bluff bodies," Progress in Aerospace Sciences, vol. 26, no. 2, pp. 169–224, 1989.

[56] P. Bearman, I. Gartshore, D. Maull, and G. V. PARKINSON, "Experiments on flow-induced vibration of a square-section cylinder," Journal of Fluids and Structures, vol. 1, 1987.

[57] E. Naudascher, J. Weske, and B. Fey, "Exploratory study on damping of galloping vibrations," Journal of Wind Engineering and Industrial Aerodynamics, vol. 8, pp. 211–222, 1981.

[58] M. A. Wawzonek, "Aeroelastic behavior of square section prisms in uniform flow," Ph.D. dissertation, University of British Columbia, 1979.

[59] L. Zuo and S. A. Nayfeh, "The two-degree-of-freedom tuned-mass damper for suppression of single-mode vibration under random and harmonic excitation," Journal of Vibration and Acoustics, vol. 128, pp. 56–65, 2006.

[60] S. Krenk, "Frequency analysis of the tuned mass damper," Journal of Applied Mechanics, vol. 72, pp. 936–942, 2005.

[61] R. A. Ibrahim, "Recent advances in nonlinear passive vibration isolators," Journal of Sound and Vibration, vol. 314, no. 3, pp. 371–452, 2008.

[62] A. Carrella, M. J. Brennan, and T. P. Waters, "Static analysis of a passive vibration isolator with quasi-zero-stiffness characteristic," Journal of Sound and Vibration, vol. 301, no. 3, pp. 678–689, 2007.

[63] I. Kovacic, M. J. Brennan, and T. P. Waters, "A study of a nonlinear vibration isolator with a quasi-zero stiffness characteristic," Journal of Sound and Vibration, vol. 315, no. 3, pp. 700–711, 2008.

[64] A. Carrella, M. J. Brennan, I. Kovacic, and T. P. Waters, "On the force transmissibility of a vibration isolator with quasi-zero-stiffness," Journal of Sound and Vibration, vol. 322, no. 4, pp. 707–717, 2009.

[65] R. Vinayaravi, D. Kumaresan, K. Jayaraj, A. K. Asraff, and R. Muthukumar, "Experimental investigation and theoretical modelling of an impact damper," Journal of Sound and Vibration, vol. 332, no. 5, pp. 1324–1334, 2013.

[66] M. Gharib and S. Ghani, "Free vibration analysis of linear particle chain impact damper," Journal of Sound and Vibration, vol. 332, no. 24, pp. 6254–6264, 2013.

[67] N. Popplewell and S. E. Semercigil, "Performance of the bean bag impact damper for a sinusoidal external force," Journal of Sound and Vibration, vol. 133, no. 2, pp. 193–223, 1989.

[68] Z. Xu, M. Y. Wang, and T. Chen, "Particle damping for passive vibration suppression : numerical modelling and experimental investigation," Journal of Sound and Vibration, vol. 279, no. 3, pp. 1097–1120, 2005.

[69] C. C. Cheng and J. Y. Wang, "Free vibration analysis of a resilient impact damper," International Journal of Mechanical Sciences, vol. 45, no. 4, pp. 589–604, 2003.

[70] K. Li and A. P. Darby, "An experimental investigation into the use of a buffered impact damper," Journal of Sound and Vibration, vol. 291, no. 3, pp. 844–860, 2006.

[71] Z. Lu, X. Lu, W. Lu, and S. F. Masri, "Experimental studies of the effects of buffered particle dampers attached to a multi-degree-of-freedom system under dynamic loads," Journal of Sound and Vibration, vol. 331, no. 9, pp. 2007–2022, 2012.

[72] A. F. Vakakis, "Inducing passive nonlinear energy sinks in vibrating systems," Journal of Vibration and Acoustics, vol. 123, no. 3, pp. 324–332, 2001.

[73] O. V. Gendelman, "Targeted energy transfer in systems with non-polynomial non linearity," Journal of Sound and Vibration, vol. 315, pp. 732–745, 2008.

[74] ——, "Transition of energy to a nonlinear localized mode in a highly asymmetric system of two oscillators," Nonlinear dynamics, vol. 25, no. 1, pp. 237–253, 2001.

[75] O. Gendelman, L. I. Manevitch, A. F. Vakakis, and R. MCloskey, "Energy pumping in nonlinear mechanical oscillators : Part idynamics of the underlying hamiltonian systems," Journal of Applied Mechanics, vol. 68, no. 1, p. 34, 2001.

[76] A. F. Vakakis and O. Gendelman, "Energy pumping in nonlinear mechanical oscillators : Part IIresonance capture," Journal of Applied Mechanics, vol. 68, no. 1, p. 42, 2001.

[77] A. F. Vakakis, L. I. Manevitch, O. Gendelman, and L. Bergman, "Dynamics of linear discrete systems connected to local, essentially non-linear attachments," Journal of Sound and Vibration, vol. 264, no. 3, pp. 559–577, 2003.

[78] A. F. Vakakis, "Shock isolation through the use of nonlinear energy sinks," Journal of Vibration and Control, vol. 9, no. 1-2, pp. 79–93, 2003.

[79] O. V. Gendelman, "Bifurcations of nonlinear normal modes of linear oscillator with strongly nonlinear damped attachment," Nonlinear Dynamics, vol. 37, no. 2, pp. 115–128, 2004.

[80] Y. V. Mikhlin and S. N. Reshetnikova, "Dynamical interaction of an elastic system and essentially nonlinear absorber," Journal of Sound and Vibration, no. 1, pp. 91–120, 2005.

[81] E. Gourdon and C. H. Lamarque, "Nonlinear energy sink with uncertain parameters," Journal of Computational and Nonlinear Dynamics, vol. 1, no. 3, pp. 187–195, 2006.

[82] A. Y. Kozmin, Y. V. Mikhlin, and C. Pierre, "Localization of energy in nonlinear systems with two degrees of freedom," International Applied Mechanics, vol. 43, no. 5, pp. 568–576, 2007.

[83] F. Schmidt and C. H. Lamarque, "Energy pumping for mechanical systems involving non-smooth saint-venant terms," International Journal of Non-Linear Mechanics, vol. 45, no. 9, pp. 866–875, 2010.

[84] Y. S. Lee, G. Kerschen, A. F. Vakakis, P. Panagopoulos, L. Bergman, and D. M. McFarland, "Complicated dynamics of a linear oscillator with a light, essentially nonlinear attachment," Physica D : Nonlinear Phenomena, vol. 204, no. 1, pp. 41–69, 2005.

[85] G. Kerschen, O. Gendelman, A. F. Vakakis, L. A. Bergman, and D. M. McFarland, "Impulsive periodic and quasi-periodic orbits of coupled oscillators with essential stiff-

ness nonlinearity," Communications in Nonlinear Science and Numerical Simulation, vol. 13, no. 5, pp. 959–978, 2008.

[86] L. I. Manevitch, A. I. Musienko, and C.-H. Lamarque, "New analytical approach to energy pumping problem in strongly nonhomogeneous 2dof systems," Meccanica, vol. 42, no. 1, pp. 77–83, 2007.

[87] L. I. Manevitch, E. Gourdon, and C. H. Lamarque, "Towards the design of an optimal energetic sink in a strongly inhomogeneous two-degree-of-freedom system," Journal of Applied Mechanics, vol. 74, no. 6, pp. 1078–1086, 2007.

[88] T. Sapsis, D. D. Quinn, O. Gendelman, A. F. Vakakis, L. A. Bergman, and G. Kerschen, "Applying l. manevitchs complexification averaging method to analyze conditions for optimal targeted energy transfer in coupled oscillators with essential stiffness nonlinearity," NPPS-2008, Moscow, Russia, 2008.

[89] D. D. Quinn, O. Gendelman, G. Kerschen, T. P. Sapsis, L. A. Bergman, and A. F. Vakakis, "Efficiency of targeted energy transfers in coupled nonlinear oscillators associated with 1:1 resonance captures : Part i," Journal of Sound and Vibration, vol. 311, no. 3, pp. 1228–1248, 2008.

[90] M. A. Al-Shudeifat, "Analytical formulas for the energy, velocity and displacement decays of purely nonlinear damped oscillators," Journal of Vibration and Control, vol. 21, no. 6, pp. 1210–1219, 2013.

[91] T. P. Sapsis, D. Dane Quinn, A. F. Vakakis, and L. A. Bergman, "Effective stiffening and damping enhancement of structures with strongly nonlinear local attachments," Journal of Vibration and Acoustics, vol. 134, no. 1, 2012.

[92] X. Fang, J. Wen, J. Yin, and D. Yu, "Highly efficient continuous bistable nonlinear energy sink composed of a cantilever beam with partial constrained layer damping," Nonlinear Dynamics, vol. 87, no. 4, pp. 2677–2695, 2017.

[93] G. Habib and F. Romeo, "The tuned bistable nonlinear energy sink," Nonlinear Dynamics, vol. 89, no. 1, pp. 179–196, 2017.

[94] D. Qiu, T. Li, S. Seguy, and M. Paredes, "Efficient targeted energy transfer of bistable nonlinear energy sink : application to optimal design," Nonlinear Dynamics, vol. 92, no. 2, pp. 443–461, 2018.

[95] S. Tsakirtzis, G. Kerschen, P. N. Panagopoulos, and A. F. Vakakis, "Multi-frequency nonlinear energy transfer from linear oscillators to mdof essentially nonlinear attachments," Journal of Sound and Vibration, vol. 285, no. 1, pp. 483–490, 2005.

[96] A. I. Musienko, C. H. Lamarque, and L. I. Manevitch, "Design of mechanical energy pumping devices," Journal of Vibration and Control, vol. 12, no. 4, pp. 355–371, 2006.

[97] E. Gourdon and C. H. Lamarque, "Energy pumping for a larger span of energy," Journal of Sound and Vibration, vol. 285, no. 3, pp. 711–720, 2005.

[98] G. Pennisi, C. Stephan, E. Gourc, and G. Michon, "Experimental investigation and analytical description of a vibro-impact NES coupled to a single-degree-of-freedom linear oscillator harmonically forced," Nonlinear Dynamics, vol. 88, pp. 1769–1784, 2017.

[99] T. Li, C. Lamarque, S. Seguy, and A. Berlioz, "Chaotic characteristic of a linear oscillator coupled with vibro-impact nonlinear energy sink," Nonlinear Dynamics, vol. 91, pp. 2319–2330, 2018.

[100] T. Li, E. Gourc, S. Seguy, and A. Berlioz, "Dynamics of two vibro-impact nonlinear energy sinks in parallel under periodic and transient excitations," International Journal of Non-Linear Mechanics, vol. 90, pp. 100–110, 2017.

[101] I. Karayannis, A. F. Vakakis, and F. Georgiades, "Vibro-impact attachments as shock absorbers," Proceedings of the Institution of Mechanical Engineers, Part C : Journal of Mechanical Engineering Science, vol. 222, no. 10, pp. 1899–1908, 2008.

[102] F. Nucera, A. F. Vakakis, D. M. McFarland, L. A. Bergman, and G. Kerschen, "Targeted energy transfers in vibro-impact oscillators for seismic mitigation," Nonlinear Dynamics, vol. 50, no. 3, pp. 651–677, 2007.

[103] Y. S. Lee, F. Nucera, A. F. Vakakis, D. M. McFarland, and L. A. Bergman, "Periodic orbits, damped transitions and targeted energy transfers in oscillators with vibro-impact attachments," Physica D : Nonlinear Phenomena, vol. 238, no. 18, pp. 1868–1896, 2009.

[104] F. Nucera, D. McFarland, L. Bergman, and A. Vakakis, "Application of broadband nonlinear targeted energy transfers for seismic mitigation of a shear frame : Computational results," Journal of Sound and Vibration, vol. 329, pp. 2973–2994, 2010.

[105] M. A. AL-Shudeifat, N. Wierschem, D. D. Quinn, A. F. Vakakis, L. A. Bergman, and B. F. Spencer, "Numerical and experimental investigation of a highly effective single-sided vibro-impact non-linear energy sink for shock mitigation," International Journal of Non-Linear Mechanics, vol. 52, pp. 96–109, 2013.

[106] M. A. AL-Shudeifat, A. F. Vakakis, and L. A. Bergman, "Shock mitigation by means of low- to high-frequency nonlinear targeted energy transfers in a large-scale structure," Journal of Computational and Nonlinear Dynamics, no. 2, 2016.

[107] T. Li, S. Seguy, and A. Berlioz, "Dynamics of cubic and vibro-impact nonlinear energy sink : Analytical, numerical, and experimental analysis," Journal of Vibration and Acoustics, vol. 138, pp. 031 010–1, 2016.

[108] ——, "On the dynamics around targeted energy transfer for vibro-impact nonlinear energy sink," NonLinear Dynamics, vol. 87, pp. 1453–1466, 2017.

[109] ——, "Optimization mechanism of targeted energy transfer with vibro-impact energy sink under periodic and transient excitation," NonLinear Dynamics, vol. 87, pp. 2415–2433, 2017.

[110] J. Wang, N. Wierschem, B. F. Spencer, and X. Lu, "Numerical and experimental study of the performance of a single-sided vibro-impact track nonlinear energy sink," Earthquake Engineering & Structural Dynamics, vol. 45, pp. 635–652, 2016.

[111] M. A. AL-Shudeifat, "Asymmetric magnet-based nonlinear energy sink," Journal of Computational and Nonlinear Dynamics, vol. 10, no. 1, 2015.

[112] S. Lo Feudo, C. Touzé, J. Boisson, and G. Cumunel, "Nonlinear magnetic vibration absorber for passive control of a multistorey structure," Journal of Sound and Vibration, vol. 438, pp. 33–53, 2019.

[113] J. Wang, N. Wierschem, B. F. Spencer Jr, and X. Lu, "Experimental study of track nonlinear energy sinks for dynamic response reduction," Engineering Structures, vol. 94, pp. 9–15, 2015.

[114] X. Lu, Z. Liu, and Z. Lu, "Optimization design and experimental verification of track nonlinear energy sink for vibration control under seismic excitation," Structural Control and Health Monitoring, vol. 24, no. 12, p. e2033, 2017.

[115] J. Wang, H. Li, B. Wang, Z. Liu, and C. Zhang, "Development of a two-phased nonlinear mass damper for displacement mitigation in base-isolated structures," Soil Dynamics and Earthquake Engineering, vol. 123, pp. 435–448, 2019.

[116] J. Wang, N. Wierschem, B. F. Spencer Jr, and X. Lu, "Numerical and experimental study of the performance of a single-sided vibro-impact track nonlinear energy sink," Earthquake Engineering & Structural Dynamics, vol. 45, no. 4, pp. 635–652, 2016.

[117] J. Wang, B. Wang, N. E. Wierschem, and B. F. Spencer Jr, "Dynamic analysis of track nonlinear energy sinks subjected to simple and stochastice excitations," Earthquake Engineering & Structural Dynamics, vol. 49, no. 9, pp. 863–883, 2020.

[118] O. V. Gendelman, G. Sigalov, L. I. Manevitch, M. Mane, A. F. Vakakis, and L. A. Bergman, "Dynamics of an eccentric rotational nonlinear energy sink," Journal of Applied Mechanics, vol. 79, pp. 011 012–1–9, 2012.

[119] G. Sigalov, O. V. Gendelman, M. A. AL-Shudeifat, L. I. Manevitch, A. F. Vakakis, and L. A. Bergman, "Resonance captures and targeted energy transfers in an inertially-coupled rotational nonlinear energy sink," Nonlinear Dynamics, vol. 69, pp. 1693–1704, 2012.

[120] Y. S. Lee, A. F. Vakakis, L. A. Bergman, D. M. McFarland, and G. Kerschen, "Suppression aeroelastic instability using broadband passive targeted energy transfers, part 1 : Theory," AIAA journal, vol. 45, no. 3, pp. 693–711, 2007.

[121] Y. S. Lee, G. Kerschen, D. M. McFarland, W. J. Hill, C. Nichkawde, T. W. Strganac, L. A. Bergman, and A. F. Vakakis, "Suppressing aeroelastic instability using broadband passive targeted energy transfers, part 2 : experiments," AIAA journal, vol. 45, no. 10, pp. 2391–2400, 2007.

[122] Y. Bichiou, M. R. Hajj, and A. H. Nayfeh, "Effectiveness of a nonlinear energy sink in the control of an aeroelastic system," Nonlinear Dynamics, vol. 86, no. 4, pp. 2161–2177, 2016.

[123] B. Pidaparthi and S. Missoum, "Stochastic optimization of nonlinear energy sinks for the mitigation of limit cycle oscillations," AIAA journal, vol. 57, no. 5, pp. 2134–2144, 2019.

[124] Y. S. Lee, A. F. Vakakis, L. A. Bergman, D. M. McFarland, and G. Kerschen, "Enhancing the robustness of aeroelastic instability suppression using multi-degree-of-freedom nonlinear energy sinks," AIAA journal, vol. 46, no. 6, pp. 1371–1394, 2008.

[125] S. A. Hubbard, D. M. McFarland, L. A. Bergman, and A. F. Vakakis, "Targeted energy transfer between a model flexible wing and nonlinear energy sink," Journal of aircraft, vol. 47, no. 6, pp. 1918–1931, 2010.

[126] K. Yang, Y.-W. Zhang, H. Ding, T.-Z. Yang, Y. Li, and L.-Q. Chen, "Nonlinear energy sink for whole-spacecraft vibration reduction," Journal of Vibration and Acoustics, vol. 139, no. 2, 2017.

[127] W. Zhang, J. Fang, Y. He, and J. Zhang, "Resonance capture and targeted energy transfer for suppressing aeroelastic instability of 2-d wing," The European Physical Journal Special Topics, vol. 228, no. 9, pp. 1873–1889, 2019.

[128] H. Guo, S. Cao, T. Yang, and Y. Chen, "Aeroelastic suppression of an airfoil with control surface using nonlinear energy sink," Nonlinear Dynamics, vol. 94, no. 2, pp. 857–872, 2018.

[129] S. A. Hubbard, D. M. McFarland, L. A. Bergman, A. F. Vakakis, and G. Andersen, "Targeted energy transfer between a swept wing and winglet-housed nonlinear energy sink," AIAA journal, vol. 52, no. 12, pp. 2633–2651, 2014.

[130] S. A. Hubbard, R. L. Fontenot, D. M. McFarland, P. G. Cizmas, L. A. Bergman, T. W. Strganac, and A. F. Vakakis, "Transonic aeroelastic instability suppression for a swept wing by targeted energy transfer," Journal of Aircraft, vol. 51, no. 5, pp. 1467–1482, 2014.

[131] D. R. Pacheco, F. D. Marques, and A. J. Ferreira, "Panel flutter suppression with nonlinear energy sinks : Numerical modeling and analysis," International Journal of Non-Linear Mechanics, vol. 106, pp. 108–114, 2018.

[132] Z. Yan, S. A. Ragab, and M. R. Hajj, "Passive control of transonic flutter with a nonlinear energy sink," Nonlinear Dynamics, vol. 91, no. 1, pp. 577–590, 2018.

[133] T.-Z. Yang, X.-D. Yang, Y. Li, and B. Fang, "Passive and adaptive vibration suppression of pipes conveying fluid with variable velocity," Journal of Vibration and Control, vol. 20, no. 9, pp. 1293–1300, 2014.

[134] A. E. Mamaghani, S. Khadem, and S. Bab, "Vibration control of a pipe conveying fluid under external periodic excitation using a nonlinear energy sink," Nonlinear Dynamics, vol. 86, no. 3, pp. 1761–1795, 2016.

[135] X.-Y. Zhao, Y.-W. Zhang, H. Ding, and L.-Q. Chen, "Vibration suppression of a nonlinear fluid-conveying pipe under harmonic foundation displacement excitation via nonlinear energy sink," International Journal of Applied Mechanics, vol. 10, no. 09, p. 1850096, 2018.

[136] K. Zhou, F. Xiong, N. Jiang, H. Dai, H. Yan, L. Wang, and Q. Ni, "Nonlinear vibration control of a cantilevered fluid-conveying pipe using the idea of nonlinear energy sink," Nonlinear Dynamics, vol. 95, no. 2, pp. 1435–1456, 2019.

[137] T. Yang, T. Liu, Y. Tang, S. Hou, and X. Lv, "Enhanced targeted energy transfer for adaptive vibration suppression of pipes conveying fluid," Nonlinear Dynamics, vol. 97, no. 3, pp. 1937–1944, 2019.

[138] C. Dongyang, L. K. Abbas, W. Guoping, R. Xiaoting, and P. Marzocca, "Numerical study of flow-induced vibrations of cylinders under the action of nonlinear energy sinks (ness)," Nonlinear Dynamics, vol. 94, no. 2, pp. 925–957, 2018.

[139] D. Chen, C. Gu, K. Fang, J. Yang, D. Guo, and P. Marzocca, "Vortex-induced vibration of a cylinder with nonlinear energy sink (nes) at low reynolds number," Nonlinear Dynamics, pp. 1–18, 2021.

[140] A. B. Blanchard, O. V. Gendelman, L. A. Bergman, and A. F. Vakakis, "Capture into slow-invariant-manifold in the fluidstructure dynamics of a sprung cylinder with a nonlinear rotator," Journal of Fluids and Structures, vol. 63, pp. 155–173, 2016.

[141] A. Blanchard, L. A. Bergman, and A. F. Vakakis, "Targeted energy transfer in laminar vortex-induced vibration of a sprung cylinder with a nonlinear dissipative rotator," Physica D : Nonlinear Phenomena, vol. 350, pp. 26–44, 2017.

[142] R. K. R. Tumkur, A. J. Pearlstein, A. Masud, O. V. Gendelman, A. B. Blanchard, L. A. Bergman, and A. F. Vakakis, "Effect of an internal nonlinear rotational dissipative

element on vortex shedding and vortex-induced vibration of a sprung circular cylinder," Journal of Fluid Mechanics, vol. 828, pp. 196–235, 2017.

[143] A. B. Blanchard and A. J. Pearlstein, "On-off switching of vortex shedding and vortex-induced vibration in crossflow past a circular cylinder by locking or releasing a rotational nonlinear energy sink," Physical Review Fluids, vol. 5, no. 2, p. 023902, 2020.

[144] D. Chen, C. Gu, R. Zhang, J. Liu, D. Guo, and P. Marzocca, "Vortex-induce vibrations of two degrees of freedom sprung cylinder with a rotational nonlinear energy sink (r-nes) : a numerical investigation," Journal of Computational and Nonlinear Dynamics, 2021.

[145] G. R. Franzini, "An elastic rotative nonlinear vibration absorber (ernva) as a passive suppressor for vortex-induced vibrations," Nonlinear Dynamics, vol. 103, no. 1, pp. 255–277, 2021.

[146] D. J. Rodrigues, A. R. Champneys, M. I. Friswell, and R. E. Wilson, "Experimental investigation of a single-plane automatic balancing mechanism for a rigid rotor," Journal of Sound and Vibration, vol. 330, no. 3, pp. 385–403, 2011.

[147] M. Makram, S. S. Kossa, M. K. Khalil, A. F. Nemnem, and G. Samer, "Experimental investigation of ABB effect on unbalanced rotor vibration," Journal of Coupled Systems and Multiscale Dynamics, vol. 7, pp. 225–231, 2017.

[148] T. Inoue, Y. Ishida, and H. Niimi, "Vibration analysis of a self-excited vibration in a rotor system caused by a ball balancer," Journal of Vibration and Acoustics, vol. 134, no. 2, 2012.

[149] T. C. Chan, C. K. Sung, and P. C. P. Chao, "Non-linear suspension of an automatic ball balancer," International Journal of Non-Linear Mechanics, vol. 46, no. 2, pp. 415–424, 2011.

[150] M. Rezaee and R. Fathi, "A new design for automatic ball balancer to improve its performance," Mechanism and Machine Theory, vol. 94, pp. 165–176, 2015.

[151] J. W. Hijmissen and W. T. van Horssen, "On aspects of damping for a vertical beam with a tuned mass damper at the top," Nonlinear Dynamics, vol. 50, pp. 169–190, 2007.

[152] A. F. Vakakis, O. V. Gendelman, L. A. Bergman, D. M. McFarland, G. Kerschen, and Y. S. Lee, Nonlinear targeted energy transfer in mechanical and structural systems. Springer Science & Business Media, 2008, vol. 156.

[153] H. Guo, B. Liu, Y. Yu, S. Cao, and Y. Chen, "Galloping suppression of a suspended cable with wind loading by a nonlinear energy sink," Archive of Applied Mechanics, vol. 87, pp. 1007–1018, 2017.

[154] M. A. AL-Shudeifat, N. Wierschem, D. D. Quinn, A. F. Vakakis, L. A. Bergman, and B. F. Spencer, "Numerical and experimental investigation of a highly effective single-sided vibro-impact non-linear energy sink for shock mitigation," International Journal of Non-Linear Mechanics, vol. 52, pp. 96–109, 2013.

[155] C.-J. Lu and C.-H. Hung, "Stability analysis of a three-ball automatic balancer," Journal of Vibration and Acoustics, vol. 130, no. 5, 2008.

[156] H.-W. Chen, Q.-J. Zhang, and X.-Q. Wu, "Stability and dynamic analyses of a horizontal axis washing machine with a ball balancer," Mechanism and Machine Theory, vol. 87, pp. 131–149, 2015.

[157] L. Amar, E. Laurendeau, G. Michon, and S. Prothin, "Passive control of flutter applied on a 3DOF airfoil," in ICTAM 2016-Montréal, Canada, 2016.

[158] M. M. Selwanis, G. R. Franzini, C. Béguin, and F. P. Gosselin, "Wind tunnel demonstration of galloping mitigation with a purely nonlinear energy sink," Journal of Fluids and Structures, vol. 100, p. 103169, 2021.

[159] M. A. Wawzonek, "Aeroelastic behavior of square section prisms in uniform flow," Ph.D. dissertation, University of British Columbia, 1979.

[160] L. Meirovitch, Fundamentals of vibrations. Waveland Press, 2010.

[161] I. Kovacic, R. Rand, and S. Mohamed Sah, "Mathieu's equation and its generalizations : overview of stability charts and their features," Applied Mechanics Reviews, vol. 70, no. 2, 2018.

[162] H. Ding and L.-Q. Chen, "Designs, analysis, and applications of nonlinear energy sinks," Nonlinear Dynamics, vol. 100, pp. 3061–3107, 2020.

[163] D. Pereira, Wind Rose. The MathWorks Inc. (https://www.mathworks.com/matlabcentral/fileexchange/47248-wind-rose), Retrieved October 2021.

[164] M. Selwanis, G. R. Franzini, C. Béguin, and F. P. Gosselin, "How a ball free to orbit in a circular track mitigates the galloping of a square prism," Research Square [Preprint]., Posted : October 18, 2021. https://doi.org/10.21203/rs.3.rs-973095/v1.

APPENDIX A MEASUREMENT UNCERTAINTIES CALCULATION

We use a protractor read by naked eye to fix the square prism angle of attack expecting a small deviation from the required angle. To eliminate any error that may arise from this deviation, we use the KolmogorovSmirnov (K-S) test. This statistical method mainly quantifies how the distribution functions of two data samples are similar. After reflecting C_y values measured at negative angles about the origin, we compare it to C_y values measured at positive angles (figure A.1a). The KolmogorovSmirnov test indicates the dissimilarity between the two C_y curves by converting the two samples of normal force coefficient data to another form, C_y_sum (table A.1), where:

$$C_{y\_}sum_i = \sum_{j=1}^{i} C_{y_j}, \tag{A.1}$$

$$D = \mid \sum_{j=1}^{n} (C_{y_1\_}sum_j - C_{y_2\_}sum_j) \mid . \tag{A.2}$$

The absolute value of summation of the differences, D, indicates how the two data samples follow the same distribution and increases when the data samples are highly dissimilar. For the C_y curve, a shift in α changes the value of C_y at each angle of attack according to the slope of the curve at this point.

$$\delta C_y = \delta\alpha \cdot slope \tag{A.3}$$

Based on the KolmogorovSmirnov test, a MATLAB code is written to get the optimum shift in α (not exceeding the angle measurement resolution of $\pm 1^o$) that achieves the best symmetry between the measured data of C_y at the positive and negative values, see Figure A.1. Figure A.1b shows the C_y values measured for negative and positive angles of attack with a 0.65^o shift. Using a smoothing parameter p= 0.999995, a spline fits the measured data after eliminating the systematic error (Figure A.1c). This fitting works as input for the NES-prism mathematical model to introduce accurate values for the galloping force coefficient of the square prism at different angles of attack.

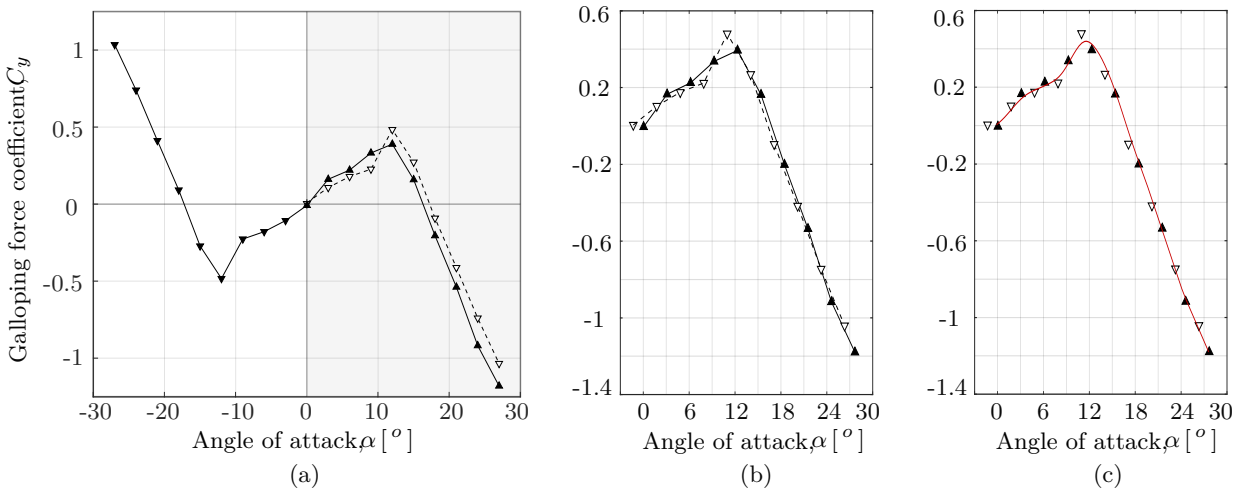

Figure A.1 The normal force coefficient C_y ; —▲— measured at positive angles of attack $+\alpha$, —▼— measured at $-\alpha$, -▽- the reflection of the C_y curve of negative angles about the origin. (a) direct measurement, (b) measurements shifted by 0.65^o to eliminate the systematic error in the angles' reading, (c) C_y fitting (—).

Table A.1 K-S test for the two data samples of the measured C_y at positive and negative angles of attack.

i	Angle	C_{y1}	C_{y2}	C_{y1}_sum	C_{y2}_sum	Difference
1	0^o	0.0084	-0.0084	0.0084	-0.0084	0.0168
2	3^o	0.1071	0.1612	0.1155	0.1528	-0.0373
3	6^o	0.1789	0.2206	0.2944	0.3734	-0.079
4	9^o	0.2268	0.3320	0.5212	0.7054	-0.1842
5	12^o	0.4834	0.3891	1.0046	1.0945	-0.0899
6	15^o	0.2722	0.1588	1.2768	1.2533	0.0235
7	18^o	-0.0913	-0.2050	1.1855	1.0483	0.1372
8	21^o	-0.4123	-0.5385	0.7732	0.5098	0.2634
9	24^o	-0.7401	-0.9188	0.0331	-0.4090	0.4421
10	27^o	-1.0348	-1.1807	-1.0017	-1.5897	0.588
					D=$\sum$ Difference=	1.08